MODELING PARTICLE SUSPENSIONS USING LATTICE BOLTZMANN METHOD

A Dissertation
Presented to
The Academic Faculty

By

Wenbin Mao

In Partial Fulfillment
of the Requirements for the Degree
Doctor of Philosophy in the
George W. Woodruff School of Mechanical Engineering

Georgia Institute of Technology

December 2013

MODELING PARTICLE SUSPENSIONS USING LATTICE BOLTZMANN METHOD

Approved by:

Dr. Alexander Alexeev, Advisor
School of Mechanical Engineering
Georgia Institute of Technology

Dr. Edmond T. Chow
School of Computer Science and Engineering
Georgia Institute of Technology

Dr. Todd A. Sulchek
School of Mechanical Engineering
Georgia Institute of Technology

Dr. Dino Di Carlo
Department of Bioengineering
University of California, Los Angeles

Dr. Peter J. Hesketh
School of Mechanical Engineering
Georgia Institute of Technology

Date Approved: August, 2013

ACKNOWLEDGEMENTS

First of all I would like to express my most sincere gratitude to my advisor, Dr. Alexander Alexeev, for his guidance, encouragement and support over the past four years through my whole study and research at Georgia Tech. His insight, curiosity, and dedication provided me with broad and exciting learning and research experience. I have learnt the very important lesson of being a good researcher by his perspectives on research.

I am also deeply grateful to my dissertation reading committee, Drs. Todd Sulchek, Dino Di Carlo, Peter Hesketh, and Edmond Chow for reviewing my dissertation and providing me with their valuable reviews and comments.

I would like to thank my lab mates, colleagues, and friends for their support, discussions, and encouragement during my stay at Georgia Tech.

I wish to express my appreciate to American Physical Society, National Science Foundation, United States – Israel Binational Science Foundation, and Georgia Institute of Technology for their generous financial supports to help me present my Ph.D. research at scientific conferences and workshops.

Finally, I would like to say thanks to my parents and family members for their unconditional supports. I specially thank my girlfriend, for her consistent love and encouragement in both easy and difficult times. I dedicate this work to them.

TABLE OF CONTENTS

LIST OF TABLES

Page

LIST OF FIGURES

SUMMARY

Particle suspensions are common both in nature and in various technological applications. The complex nature of hydrodynamic interactions between particles and the solvent makes such analysis difficult that often requires numerical modeling to understand the behavior of particle suspensions. In this dissertation, we employ a hybrid computational model that integrates a lattice spring model for solid mechanics and a lattice Boltzmann model for fluid dynamics. We use this model to study several practical problems in which the dynamics of spherical and spheroidal particles and deformable capsules in dilute suspensions plays an important role. The results of our studies yield new information regarding the dynamics of solid particle in pressure-driven channel flows and disclose the nonlinear effects associated with fluid inertia leading to particle cross-stream migration. This information not only give us a fundamental insight into the dynamics of dilute suspensions, but also yield engineering guidelines for designing high throughput microfluidic devices for sorting and separation of synthetic particles and biological cells.

We first demonstrate that spherical particles can be size-separated in ridged microchannels. Specifically, particles with different sizes follow distinct trajectories as a result of the nonlinear inertial effects and secondary flows created by diagonal ridges in the channel. Then, separation of biological cells by their differential stiffness is studied and compared with experimental results. Cells with different stiffness squeeze through narrow gaps between solid diagonal ridges and channel wall, and migrate across the microchannel with different rates depending on their stiffness. This deformability-based

microfluidic platform may be valuable for separating diseased cells from healthy cells, as a variety of cell pathologies manifest through the change in mechanical cell stiffness. Finally, the dynamics of spheroid particles in simple shear and Poiseuille flows are studied. Stable rotational motion, cross-stream migration, and equilibrium trajectories of non-spherical particles in flow are investigated. Effects of particle and fluid inertia on dynamics of particles are disclosed. The dependence of equilibrium trajectory on particle shape reveals a potential application for shape based particle separation.

CHAPTER 1

INTRODUCTION

1.1 Background

Suspensions are two phase materials usually consisting of solid and fluid phases. For example, in colloidal systems, particles are dispersed in a liquid solvent. Particle suspensions are important both in nature and in industry. Suspensions are utilized in the manufacturing processes, food processing, paint and paper manufacturing, and pharmaceutics. Particle-laden flows are also found in fluidized beds, packed beds, and other technological processes [1]. Thus, it is important to be able to predict the properties of particle suspensions. The complex nature of hydrodynamic interactions between particles and a solvent makes such analysis difficult that often requires numerical modeling to fully understand the behavior of particle suspensions.

In the simplest case, particle suspension is composed of rigid spherical particles dispersed in a Newtonian fluid. When suspension is set in motion and flows, the particle-fluid system is characterized by an additional dissipative mechanism and an increased bulk viscosity. The viscosity of suspensions had been an active research area since Einstein's pioneering work about a hundred years ago. It was shown that in the dilute limit a suspension is a Newtonian fluid, but with an effective viscosity that is $(1+2.5\phi)$ times greater than the fluid viscosity, where ϕ is the solid fraction [2]. When the solid fraction increases, particle interactions due to hydrodynamics, Brownian motion, and inter-particle forces make system dynamics very complex. As a result, these interactions

lead to a macroscopic behavior that is significantly different from that of a Newtonian fluid.

In order to describe suspensions, the hydrodynamic interactions should be considered. First, the dynamics of a Newtonian fluid is governed by the Navier-Stokes equation,

$$\frac{\partial \mathbf{u}}{\partial t} + \mathbf{u} \cdot \nabla \mathbf{u} = -\nabla p + \frac{1}{\mathrm{Re}} \nabla^2 \mathbf{u} . \qquad (1)$$

Here, $\mathbf{u}$ and p are the fluid velocity and pressure, respectively. The Reynolds number, Re, characterizes the strength of inertial force over viscous force. On the particle scale, it is defined as $\mathrm{Re}_p = 2\rho U a/\mu$, where a, ρ and μ are the particle radius, fluid density, and fluid viscosity, respectively. When flow is dominated by viscosity and particles are small, one can assume that $\mathrm{Re} = 0$, i.e. the fluid inertia can be neglected. This is referred to a Stokes or creeping flow and allows one to significantly simplify the equations governing fluid motion. Due to the linearity of the Stokes equations, various analytical techniques such as Green's function and multipole expansions are available for the solution of Stokes flow problems [3, 4].

Researchers have extensively studied suspensions in a Stokes flow [5-7]. The quasi-steady nature of Stokes flow implies that particle positions and driving forces are sufficient to define the dynamics of a particle. It means there is no history dependence. Furthermore, linearity of the Stokes flow allows superposition of independent solutions. This has been exploited, for example, to study the combined effect of shear and Brownian motion on the suspension [8, 9].

Thus, Stokes flow suspensions are well-examined and well-understood. However, the effect of inertia on the motion of suspended particles has not yet been studied

thoroughly. Inertia is important when, for example, particles are large or a suspension is far from equilibrium [10]. In these situations, the behavior of the solid and fluid phases is coupled and the assumption of a zero Reynolds number is invalid, requiring the solution of the complete Navier-Stokes equations to correctly describe the flow of suspended particles.

Inertia may cause many important phenomena even in the dilute suspension limit. Experiments show that in a pressure-driven pipe flow with small inertia, the particles migrate to an equilibrium position located at a distance of about 0.6 of the pipe radius from the pipe axis [11, 12]. The migration takes place due to fluid inertia that causes a lift force acting perpendicular to the stream-wise direction. At higher Reynolds numbers where the effect of fluid inertia is more prominent, it is found that the equilibrium position of particles shifts closer to the wall [13, 14].

Inertia can affect the flow pattern of suspensions in a simple shear flow. It is found recently that the streamlines close to the surface of the particles are not closed but actually spiraling [15]. It implies that in heat and mass transfer problems inertia provides a convective mechanism for particle transport through outward spiraling streamlines.

The inclusion of convective terms on the left hand side of the Navier-Stokes equation adds nonlinearity to the problem. This rules out exact analytical solutions even for a single particle and one has to rely on perturbation or fully numerical methods. Furthermore, simulations provide a more detailed and accurate description than experimentation. In particular, confounding variables that can be difficult to eliminate or quantify experimentally (such as particle roughness and interparticle forces) can be easily controlled in simulations [1].

Recently, the lattice Boltzmann method (LBM) has gained much attention as a tool for modeling fluid flows involving particulate suspensions [16-18]. LBM is a mesoscopic method for solving the Navier-Stokes equations. Introducing particles and imposing the correct boundary conditions at the solid-fluid interface allow the many-body, time-dependent hydrodynamic interactions among particles and fluid to be properly simulate. Unlike Stokesian dynamics [19], LBM is capable of simulating flow at finite Reynolds numbers with the effect of inertia. Compared with traditional computational fluid dynamics methods like finite element method (FEM) or finite volume method (FVM), LBM is relatively simple due to its spatial locality and easier for parallelization [20, 21].

1.2 Objectives

Our proposed studies are aimed to address the following scientific questions: (1) to understand the characteristic of inertial migration of spherical particles in pressure-driven flow and to employ the inertial effects for designing a microfluidic device capable of continuous separation of microparticles; (2) to probe the motion of compliant cells in microchannels with periodical constrictions and to examine how the dynamical interplay between elastic deformation and fluid flow can be harnessed to separate cells with different mechanical stiffness; (3) to study the dynamics of spheroid particles in simple shear and Poiseuille flows and to investigate how non-spherical particles can be separated based on their shapes. To reach our goals, we develop and validated a hybrid numerical method for fluid-structure interactions that is based on the lattice Boltzmann method for incompressible viscous fluids. This three-dimensional, fully-coupled model will not only be able to capture the motion and deformation of solid particles in a flow with a non-zero

Reynolds number, but also can accurately simulate viscous flows and relevant hydrodynamic interactions between suspended particles and complex microchannel geometry.

CHAPTER 2

METHODOLOGY

2.1 Lattice Boltzmann Method

Historically, the lattice Boltzmann method (LBM) is a descendent of the lattice gas automata (LGA) where the discrete positions and the velocities of single particles are tracked on a lattice while satisfying the conservation equations locally. In a lattice gas, after each time step, the state at a given site can be determined by the state of the site itself and the neighboring sites, before the current time step [22]. The disadvantages of the lattice gas include the lack of Galilean invariance and statistical noise.

The LBM can be directly derived from the Boltzmann equation, evolved from the idea of fixing the drawbacks of the LGA approach. Instead of Boolean variables associated with a given lattice direction in LGA, the LBM uses continuous distribution functions. In this way, the statistical noise in the LBM can be eliminated. Accompanying this replacement, the discrete collision rule is also replaced by a continuous function known as the collision operator. This gives much more flexibility to LBM, and leads to Galilean invariance without scaling of time and allows the tuning of viscosity [20].

We use the LBM approach developed by Ladd and his group [23] to model the hydrodynamics of fluid flow. The state of the system discretized in space and time is characterized by the velocity distribution function $f_i(\mathbf{r},t)$, which describes the number density of the LB particles moving with discrete velocity $\mathbf{c}_i$ at a lattice node $\mathbf{r}$ at time *t*.

The hydrodynamic fields, i.e., mass density ρ , momentum density $\mathbf{j} = \rho\mathbf{u}$, and momentum flux $\mathbf{\Pi} = p\mathbf{I} + \rho\mathbf{uu}$, are moments of velocity distribution function,

$$\rho = \sum_i f_i \,,\ \mathbf{j} = \sum_i f_i \mathbf{c}_i \,,\ \mathbf{\Pi} = \sum_i f_i \mathbf{c}_i \mathbf{c}_i \,. \tag{2}$$

The lattice Boltzmann equation (LBE) for the time evolution of $f_i(\mathbf{r},t)$ is written as

$$f_i(\mathbf{r} + \mathbf{c}_i \Delta t, t + \Delta t) = f_i(\mathbf{r},t) + \sum_j S_{ij} f_j^{neq} \,, \tag{3}$$

where Δt is the time step and the linearized collision operator S_{ij} describes the change in f_i due to collision, $f_i^{neq} = f_i - f_i^{eq}$ is the non-equilibrium distribution function, and the lattice vectors are labeled by *i*. This simple evolution equation is second-order accurate in space and time [20]. The numerical diffusion that usually accompanies a low-order method is eliminated by the relationship between the eigenvalues of the linearized collision operator and the fluid viscosity. For small Mach numbers ($M = u/c_s << 1$), the general form of equilibrium distribution that is chosen to recover the Navier-Stokes equations can be written as,

$$f_i^{eq} = a^{c_i} \left[\rho + \frac{\mathbf{j} \cdot \mathbf{c}_i}{c_s^2} + \frac{\rho \mathbf{uu} : (\mathbf{c}_i \mathbf{c}_i - c_s^2 \mathbf{I})}{2 c_s^4} \right], \tag{4}$$

where $c_s = \Delta x / \sqrt{3} \Delta t$ is the sound speed, Δx is the spacing between neighboring lattice nodes, Δt is the time step, and $\mathbf{I}$ is the identity tensor. Typically, Δx and Δt are both chosen to be unity in LBM for simplicity. If the inertial term, which is expressed through the quadratic term in the velocity of fluid, $\mathbf{uu}$, can be neglected, then the corresponding

equilibrium distribution is reduced to a linear form, which leads to the Stokes equation in the continuum limit [24], $f_i^{eq} = a^{c_i}\left[\rho + \frac{\mathbf{j}\cdot\mathbf{c}_i}{c_s^2}\right]$.

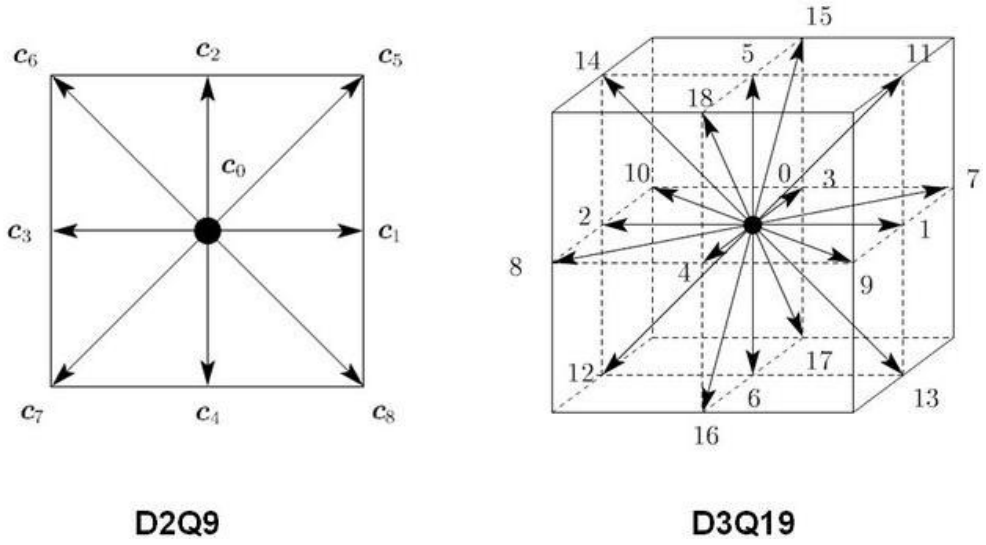

Figure 1 Some common lattice structures.

We use a 19 velocity three-dimensional D3Q19 model which has one stationary particle and 18 velocities corresponding to the [100] and [110] directions of a simple cubic lattice (Fig. 1). The distribution associated with each velocity has a weight a^{c_i} that describes the fraction of particles with velocity $\mathbf{c}_i$ in a system at rest. These weights depend only on the speed $\mathbf{c}_i$ and for D3Q19 model they are

$$a^0 = \frac{1}{3},\ a^1 = \frac{1}{18},\ a^{\sqrt{2}} = \frac{1}{36},$$

$$\mathbf{c}_i = \begin{cases} (0,0,0), & i = 0 \\ (\pm 1,0,0),(0,\pm 1,0),(0,0,\pm 1), & i = 1,2,\ldots,6 \\ (\pm 1,\pm 1,0),(\pm 1,0,\pm 1),(0,\pm 1,\pm 1), & i = 7,8,\ldots,18 \end{cases} . \qquad (5)$$

For D2Q9 model, these weights are 4/9, 1/9, and 1/36 respectively.

The fundamental limitation of this class of lattice Boltzmann models is that the Mach number must be small, since the compressibility error is on the order of $O(M^2)$ [25]. In our simulations, we always keep $M < 0.15$. If it is not specified otherwise, we use a 3-parameter collision operator [23], allowing for separate relaxation of the 5 shear modes, one bulk mode, and 9 kinetic modes. In general, the eigenvalues of kinetic modes are set to -1, which simplifies the simulation and ensures a rapid relaxation of the non-hydrodynamic modes. The collision operator can be further simplified by taking a single eigenvalue for both viscous and kinetic modes. This would recover to the most popular form of the collision operator, so-called single relaxation time Bhatnagar-Gross-Krook (BGK) model,

$$f_i(\mathbf{r}+\mathbf{c}_i\Delta t, t+\Delta t) = f_i(\mathbf{r},t) - \frac{1}{\tau}(f_i - f_i^{eq}), \tag{6}$$

where $\tau = -\frac{1}{\lambda}$ is the relaxation time. However, the absence of a clear time scale separation between the kinetic and viscous modes can sometimes cause errors at solid-fluid interface [23].

In the Ladd's model, the post-collision distribution $f_i^* = f_i + \sum_j S_{ij} f_j^{neq}$ is written as

$$f_i^* = a^{c_i}\left[\rho + \frac{\mathbf{j}\cdot\mathbf{c}_i}{c_s^2} + \frac{(\rho\mathbf{u}\mathbf{u} + \boldsymbol{\Pi}^{neq,*}) : (\mathbf{c}_i\mathbf{c}_i - c_s^2\mathbf{I})}{2c_s^4}\right]. \tag{7}$$

In the collision process, mass and momentum remain conserved, but the non-equilibrium momentum flux changes according to

$$\boldsymbol{\Pi}^{neq,*} = (1+\lambda)\overline{\boldsymbol{\Pi}}^{neq} + \frac{1}{3}(1+\lambda_v)(\boldsymbol{\Pi}^{neq} : \mathbf{I})\mathbf{I}, \tag{8}$$

where $\mathbf{\Pi}^{neq} = \mathbf{\Pi} - \mathbf{\Pi}^{eq}$ and $\overline{\mathbf{\Pi}}^{neq}$ indicates the traceless part of $\mathbf{\Pi}^{neq}$. The parameters λ and λ_v are related to the fluid shear and bulk viscosities, respectively,

$$\mu = -\rho c_s^2 \Delta t \left(\frac{1}{\lambda} + \frac{1}{2} \right), \ \mu_v = -\frac{2\rho c_s^2}{3} \Delta t \left(\frac{1}{\lambda_v} + \frac{1}{2} \right). \tag{9}$$

The factor of 1/2 corrects for numerical diffusion, so that viscous momentum diffuses at the expected speed for the given viscosity.

In the presence of an externally imposed force density $\mathbf{g}$, for example a pressure gradient or a gravitational field, the time evolution equation of the lattice Boltzmann model includes an additional term $g_i(\mathbf{r},t)$,

$$f_i(\mathbf{r} + \mathbf{c}_i \Delta t, t + \Delta t) = f_i^*(\mathbf{r},t) + g_i(\mathbf{r},t). \tag{10}$$

This forcing term can be expanded in a power series in the particle velocity [26],

$$g_i = \left(1 + \frac{\lambda}{2} \right) a^{c_i} \left[\frac{\mathbf{g} \cdot \mathbf{c}_i}{c_s^2} + \frac{(\mathbf{gu} + \mathbf{ug}) : (\mathbf{c}_i \mathbf{c}_i - c_s^2 \mathbf{I})}{2 c_s^4} \right] \Delta t \,. \tag{11}$$

More accurate solutions of the velocity field are obtained, when they include a portion of the momentum added to each node and use value $\mathbf{u}'$ to replace $\mathbf{u}$ in the calculation of g_i and f_i^* [27],

$$\mathbf{j}' = \rho \mathbf{u}' = \sum_i f_i \mathbf{c}_i + \mathbf{g} \Delta t / 2 \,. \tag{12}$$

An applied pressure gradient may also be represented by a constant force density. Indeed, adding a constant force in one direction is equivalent to changing the pressure difference in this direction, and this is done in our simulations to model flows driven by a pressure gradient.

The macroscopic behavior arising from the lattice Boltzmann equation can be found from a multi-scale analysis or Chapman-Enskog expansion [17], using an expansion parameter ε or Knudsen number, defined as the ratio of molecular mean free path length to a characteristic macroscopic length. The hydrodynamic limit corresponds to $\varepsilon << 1$. It can be shown that the lattice Boltzmann equation reproduces the Navier-Stokes equations with an accuracy that is of the order of ε^2 and u^2 [20]. Thus at sufficiently low Mach numbers, the method is of the second-order accuracy in space.

2.1.1 Multiple-relaxation-time Model

The multiple-relaxation-time (MRT) or generalized approach dates back to d'Humieres' pioneering work [28, 29]. The MRT lattice Boltzmann equation overcomes some obvious defects of the LBGK model, in addition to being more stable, it allows one to tune the eigenvalues of the collision matrix, expanding the application to a much wider range of fluid and thermal transport systems. The MRT model has been successively used for multiphase flows [30], free surfaces [31], thermal flows [32], and viscoelastic flows [33].

In the MRT model, the time evolution of the distribution function is expressed in moment space instead of the real space. To project into moment space, we need diagonalize the collision operator S_{ij} using a transformation matrix $\mathbf{M} = \sum_i |i\rangle\langle e_i|$, and the inversion of transformation matrix can be obtained using orthogonality relation, $\mathbf{M}^{-1} = \sum_i |we_i\rangle\langle i| / \langle we_i | e_i \rangle$. Here, $|i\rangle = [0, 0, \ldots, 1, 0, \ldots 0]^T$, where ith element is 1, others are 0. From here on, the Dirac notations of bracket $|\ \rangle$ and $\langle\ |$ are used to denote the column and row vectors, respectively. Eigenvectors of the collision operator are

$|e_i\rangle = [e_{i0}, e_{i1}, \ldots, e_{ib}]^T$ and corresponding weighted eigenvectors of the collision operator are $|we_i\rangle$, where b is the number of velocity vectors and $w_i = \sum_k a^{c_k} e_{i,k}^2$ is the ith weight. These eigenvectors can be constructed from irreducible polynomials of the lattice vectors $\mathbf{c}_i$, and can be found in [29]. The advantage of this choice of eigenvectors is that the equilibrium distribution has no projection onto the kinetic modes [34]. By use of weighted eigenvectors, the implementation of thermal fluctuations is simplified. Applying the transformation to the evolution equation of LBM (Eq. (3)) yields

$$f_i(\mathbf{r} + \mathbf{c}_i \Delta t, t + \Delta t) - f_i(\mathbf{r}, t) = \mathbf{M}^{-1} \hat{\mathbf{S}} \left[m_i(\mathbf{r}, t) - m_i^{eq}(\mathbf{r}, t) \right], \tag{13}$$

where $\hat{\mathbf{S}} = \mathbf{M}\mathbf{S}\mathbf{M}^{-1} = diag(s_0, s_1, \ldots, s_b)$ is a diagonal matrix whose elements are eigenvalues of the collision operator, and $|m\rangle = \mathbf{M}|f\rangle$ are the modes or moments of distribution function. We can restore the distribution functions from the modes by $|f\rangle = \mathbf{M}^{-1}|m\rangle$.

In the D3Q19 model, the corresponding 19 moments $|m\rangle$ are arranged in the following order

$$|m\rangle = [\rho, e, \varepsilon, j_x, q_x, j_y, q_y, j_z, q_z, 3p_{xx}, 3\pi_{xx}, p_{ww}, \pi_{ww}, p_{xy}, p_{yz}, p_{xz}, m_x, m_y, m_z]^T. \tag{14}$$

Here, fluid density ρ and momentums j_x, j_y, j_z are conserved, whereas kinetic energy e, kinetic energy square ε, energy flux q_x, q_y, q_z, symmetric traceless of the viscous stress tensor ($3p_{xx}$, p_{ww}, p_{xy}, p_{yz}, p_{xz}), and other five modes are not conserved. The diagonal collision matrix is

$$\hat{\mathbf{S}} = diag(0, s_1, s_2, 0, s_4, 0, s_4, 0, s_4, s_9, s_{10}, s_9, s_{10}, s_{13}, s_{13}, s_{13}, s_{16}, s_{16}, s_{16}), \tag{15}$$

where zeros correspond to conserved moments. The matrix $\mathbf{M}$ is given by

1	1	1	1	1	1	1	1	1	1	1	1	1	1	1	1	1	1	1
-1	0	0	0	0	0	0	1	1	1	1	1	1	1	1	1	1	1	1
1	-2	-2	-2	-2	-2	-2	1	1	1	1	1	1	1	1	1	1	1	1
0	1	-1	0	0	0	0	1	-1	1	-1	1	-1	1	-1	0	0	0	0
0	-2	2	0	0	0	0	1	-1	1	-1	1	-1	1	-1	0	0	0	0
0	0	0	1	-1	0	0	1	-1	-1	1	0	0	0	0	1	-1	1	-1
0	0	0	-2	2	0	0	1	-1	-1	1	0	0	0	0	1	-1	1	-1
0	0	0	0	0	1	-1	0	0	0	0	1	-1	-1	1	1	-1	-1	1
0	0	0	0	0	-2	2	0	0	0	0	1	-1	-1	1	1	-1	-1	1
0	2	2	-1	-1	-1	-1	1	1	1	1	1	1	1	1	-2	-2	-2	-2
0	-2	-2	1	1	1	1	1	1	1	1	1	1	1	1	-2	-2	-2	-2
0	0	0	1	1	-1	-1	1	1	1	1	-1	-1	-1	-1	0	0	0	0
0	0	0	-1	-1	1	1	1	1	1	1	-1	-1	-1	-1	0	0	0	0
0	0	0	0	0	0	0	1	1	-1	-1	0	0	0	0	0	0	0	0
0	0	0	0	0	0	0	0	0	0	0	0	0	0	0	1	1	-1	-1
0	0	0	0	0	0	0	0	0	0	0	1	1	-1	-1	0	0	0	0
0	0	0	0	0	0	0	1	-1	1	-1	-1	1	-1	1	0	0	0	0
0	0	0	0	0	0	0	-1	1	1	-1	0	0	0	0	1	-1	1	-1
0	0	0	0	0	0	0	0	0	0	0	1	-1	-1	1	-1	1	1	-1

The equilibrium values of the non-conserved moments are as follows, $e^{(eq)} = \mathbf{j}\cdot\mathbf{j}/\rho_0$, $\varepsilon^{(eq)} = 0$, $q_x^{(eq)} = q_y^{(eq)} = q_z^{(eq)} = 0$, $p_{xx}^{(eq)} = (2j_x^2 - j_y^2 - j_z^2)/3\rho_0$, $p_{ww}^{(eq)} = (j_y^2 - j_z^2)/\rho_0$, $\pi_{xx}^{(eq)} = \pi_{ww}^{(eq)} = m_x^{(eq)} = m_y^{(eq)} = m_z^{(eq)} = 0$, $p_{xy}^{(eq)} = (j_x - j_y)/\rho_0$, $p_{xz}^{(eq)} = (j_x - j_z)/\rho_0$, $p_{yz}^{(eq)} = (j_y - j_z)/\rho_0$. The constant ρ_0 is the mean density in the system and is usually set to be unity.

To ensure isotropy, most LB models include more variables than appear in the hydrodynamic equations. For D3Q19 model, only 10 independent variables are necessary to recover the three dimensional Navier-Stokes equations. These 10 variables are the density, the three components of velocity, and the six components of a symmetric stress tensor. The other extra variables are associated with non-hydrodynamic variables that have no effect on the hydrodynamic behavior, but affect the stability and accuracy of the method and the boundary conditions. The suggested eigenvalues of this model can be

found through a linear analysis [35]. The effect of these values on the boundary conditions has been previously discussed [24, 36]. The kinematic viscosity ν and the bulk viscosity ν_v of the MRT model are

$$\nu = \frac{1}{3}\left(\frac{1}{s_9} - \frac{1}{2}\right) = \frac{1}{3}\left(\frac{1}{s_{13}} - \frac{1}{2}\right),\ \nu_v = \frac{2}{9}\left(\frac{1}{s_1} - \frac{1}{2}\right). \tag{16}$$

2.2 Lattice Spring Model

The solid material in our simulations is modeled by a lattice spring model (LSM) or mass-spring model, which consists of a network of springs that connect regularly spaced mass points. LSM has been widely used in computer graphics to model deformable objects, such as cloth or fabric simulation, face animation. It has been used to model the behavior of soft tissues in surgery training systems [37] and to model membranes of capsules and biological cells [38, 39]. Compared to a finite element method (FEM), LSM has the advantage that it is more robust at large deformations, relatively simple to implement, and it typically requires less computational effort. LSM has been shown to be algebraically equivalent to simple finite-element methods in which the lattice springs are analogous to element boundaries and linear interpolations function are utilized [40, 41]. However, relatively little attention has been devoted to the accuracy of this model. In order to reproduce the correct mechanical properties of solid material, many parameters, such as mesh configuration, spring stiffness and mass of nodes, need to set up carefully [42].

In LSM, the solid body is modeled as a set of point masses (nodes) connected by weightless elastic springs obeying some variant of the Hooke's law. The spring network may either derive from a two-dimensional polygonal mesh representation of a surface, or

from a three-dimensional mesh modeling the internal structure of an object. Additional springs between nodes can be added, or the force law of the springs modified, to achieve required mechanical properties. Applying Newton's second law to the point masses including the forces applied by the springs and any external forces (due to gravity, hydrodynamic forces, etc.) gives a system of differential equations for the motion of the nodes.

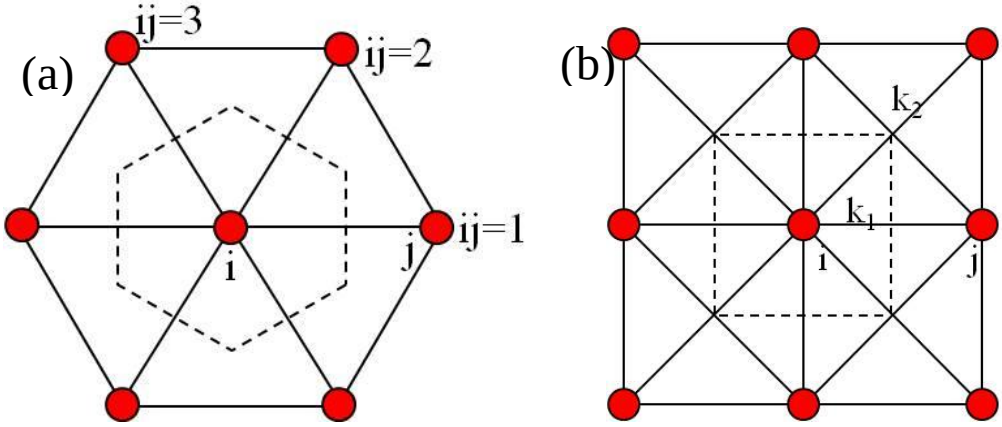

Figure 2 (a) Two-dimensional triangular lattice, with node *i* at the center, surrounded by six regularly spaced neighbors. The hexagon with dash line represents a unit cell associated with node *i*. (b) Two-dimensional square lattice with diagonal springs. The square with dash line represents a unit cell associated with node *i*. The spring constant k_1 associated with nearest-neighbor connections, and k_2 associated with diagonal second-neighbor connections.

Isotropic linear elastic materials are characterized by two parameters, i.e., Young's modulus E and Poisson's ratio ν .Therefore, it is necessary to establish a link between the parameters of LSM and the material properties. It has been proven that both triangular and square lattices can be made to behave like an isotropic elastic continuum [43]. We will briefly describe the derivation process and the relationship between spring constants and elasticity parameters.

For two-dimensional (2D) triangular lattice, a node is connected by springs to six nearest neighbors with spring constant k, as depicted in Figure 2a. The elastic energy of the node i should obey the requirements of translational and rotational invariance. Translational invariance implies that the energy can only depend on the differences between node positions, i.e., $\mathbf{r}_{ij} = \mathbf{r}_j - \mathbf{r}_i$. Rotational invariance implies that the energy can only depend on the scalar products of such vectors, i.e., $\mathbf{r}_{ij} \cdot \mathbf{r}_{ij}$. The elastic energy stored in node i is $U_i = \frac{1}{2}\sum_{ij=1}^{3} k(|\mathbf{r}_{ij}| - |\mathbf{r}_{ij}^0|)^2$, where ij is a nearest neighbor pair, $\mathbf{r}_{ij}^0$ is the equilibrium position vector between the nodes and its length $r_{ij}^0 = a_0$ is equal to the lattice spacing. The summation from 1 to 3 is due to the fact that the springs are shared by two neighbor nodes and the structure is symmetric. The elastic forces acting on the nodes can be obtained from the derivative of the elastic energy. The force acting on node i due to the deformation of the spring between nodes i and j is $F_{ij} = -\frac{\partial U_i}{\partial \mathbf{r}_{ij}} = -k\left(\frac{|\mathbf{r}_{ij}| - |\mathbf{r}_{ij}^0|}{|\mathbf{r}_{ij}|}\right)\mathbf{r}_{ij}$.

The elastic energy density of the lattice is the sum of energy stored in each node divided by the total area $A = N\sqrt{3}a_0^2/2$. The energy density is given by $\phi = \frac{1}{A}\sum_{i=1}^{N} U_i = \frac{k}{\sqrt{3}a_0^2}\sum_{ij=1}^{3}(|\mathbf{r}_{ij}| - |\mathbf{r}_{ij}^0|)^2$, where N is the total number of nodes. The dash hexagon in the Figure 2a represents a cell centered surround node i. It is assumed that the displacements imposed on the lattice remain small. In this case, the displacement difference can be rewritten as $\frac{|\mathbf{r}_{ij}| - |\mathbf{r}_{ij}^0|}{r_{ij}^0} = \hat{\mathbf{r}}_{ij} \cdot \boldsymbol{\varepsilon} \cdot \hat{\mathbf{r}}_{ij}^T$, where $\boldsymbol{\varepsilon}$ is the Cauchy's strain tensor, and $\hat{\mathbf{r}}_{ij}$ is the unit direction vector of pair ij. For example, for pair $ij = 1$, the unit direction

vector $\hat{\mathbf{r}}_{ij} = [1, 0]$, so $|\mathbf{r}_{ij}| - |\mathbf{r}_{ij}^0| = a_0 \varepsilon_{11}$. Similarly, for pair $ij = 2$ and pair $ij = 3$, $|\mathbf{r}_{ij}| - |\mathbf{r}_{ij}^0| = a_0 \left(\frac{\varepsilon_{11}}{4} + \frac{3\varepsilon_{22}}{4} + \frac{\sqrt{3}}{4}(\varepsilon_{12} + \varepsilon_{21}) \right)$ and $|\mathbf{r}_{ij}| - |\mathbf{r}_{ij}^0| = a_0 \left(\frac{\varepsilon_{11}}{4} + \frac{3\varepsilon_{22}}{4} - \frac{\sqrt{3}}{4}(\varepsilon_{12} + \varepsilon_{21}) \right)$, respectively. The elastic energy density can finally be written as a function of the strains, $\phi = \frac{k}{\sqrt{3}} \left[\frac{9}{8} \left(\varepsilon_{11}^2 + \varepsilon_{22}^2 \right) + \frac{3}{4} \varepsilon_{11} \varepsilon_{22} + \frac{3}{4} \left(\varepsilon_{12}^2 + \varepsilon_{21}^2 \right) \right]$. This form can be readily compared with the elastic energy density of a two-dimensional isotropic elastic continuum [44], i.e.,

$$\phi = \frac{1}{2} \lambda \left(\varepsilon_{11} + \varepsilon_{22} \right)^2 + \mu \left(\varepsilon_{11}^2 + \varepsilon_{12}^2 + \varepsilon_{21}^2 + \varepsilon_{22}^2 \right). \tag{17}$$

From the comparison, we obtain $\lambda = \mu = \sqrt{3}k/4$. The elastic constants can, therefore, be expressed in terms of Lamé constants λ and μ. In terms of the spring constant, Young's modulus for 2D material is $E_s = 4\mu \frac{\lambda + \mu}{\lambda + 2\mu} = \frac{2}{\sqrt{3}} k$, Poisson's ratio is $\nu_s = \frac{\lambda}{\lambda + 2\mu} = \frac{1}{3}$, area compression modulus is $K_s = \lambda + \mu = \sqrt{3}k/2$, and surface shear modulus is $G_s = \mu = \frac{E_s}{2(1+\nu_s)} = \frac{\sqrt{3}}{4} k$.

For this simple network, the Poisson's ratio is a constant value of 1/3. However, the Poisson's ratio can be modified by introducing a bond-bending interaction which controls the rotation of each of the six angles made by node *i* and two its neighbors [43]. The mass of each node is the same due to the network isotropy, $M = \rho_s \sqrt{3} a_0^2 / 2$, where ρ_s is the density of the solid material.

In a square lattice, springs connect four first and four second neighbors, as depicted in Figure 2b. Similar to the triangular lattice, the elastic energy density can be

written as $\phi = (k_1/2 + k_2/2)(\varepsilon_{11}^2 + \varepsilon_{22}^2) + k_2\varepsilon_{11}\varepsilon_{22} + k_2(\varepsilon_{12}^2 + \varepsilon_{21}^2)$. Comparison with Eq. 17 yields the following coefficients $\lambda = k_2$ and $\mu = k_1/2 = k_2$. Hence, in terms of the spring constants $k_2 = k_1/2 \equiv k$, the elastic parameters can be expressed as $E_s = 8k/3$ and $\nu_s = 1/3$. The mass of each node is given by $M = \rho_s a_0^2$.

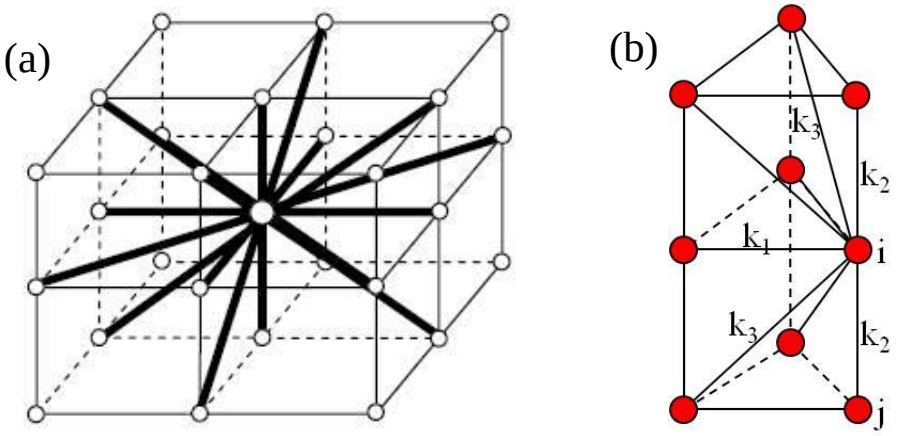

Figure 3 (a) 3D cubic lattice, with node *i* at the center, surrounded by 18 neighbors. (b) 3D triangular prism lattice, with node *i* at the center, connecting 20 neighbors (only one sixth of network element is shown here). The spring constant k_1 associated with nearest-neighbor connections at the same layer, k_2 associated with nearest-neighbor connections at the upper and lower layers, and k_3 associated with the diagonal second-neighbor connections at different layers.

For a three-dimensional (3D) model, an elastic solid can be represented by a network of springs, which connects 18 nearest and next nearest neighbors on a simple cubic lattice (Fig. 3a). It ensures three-dimensional network isotropy. Using the same method as described above, we obtain the elastic energy density as a function of the strains,

$$\phi = \frac{3k}{2a_0}(\varepsilon_{11}^2 + \varepsilon_{22}^2 + \varepsilon_{33}^2) + \frac{k}{a_0}(\varepsilon_{11}\varepsilon_{22} + \varepsilon_{11}\varepsilon_{33} + \varepsilon_{22}\varepsilon_{33}) + \frac{2k}{a_0}(\varepsilon_{12}^2 + \varepsilon_{13}^2 + \varepsilon_{23}^2). \qquad (18)$$

Comparing with 3D isotropic continuum equation [44],

$$\phi = (\mu + \lambda/2)\left(\varepsilon_{11}^2 + \varepsilon_{22}^2 + \varepsilon_{33}^2\right) + \lambda(\varepsilon_{11}\varepsilon_{22} + \varepsilon_{11}\varepsilon_{33} + \varepsilon_{22}\varepsilon_{33}) + 2\mu\left(\varepsilon_{12}^2 + \varepsilon_{13}^2 + \varepsilon_{23}^2\right), \qquad (19)$$

we find the following relationship $\mu = \lambda = k/a_0$. Thus, the elastic parameters are $E = \frac{\mu(3\lambda + 2\mu)}{\mu + \lambda} = \frac{5k}{2a_0}$, $\nu = \frac{\lambda}{2(\lambda + \mu)} = \frac{1}{4}$, and the bulk modulus is $K = \lambda + 2\mu/3 = 5k/3a_0$. The Poisson's ratio can be modified by adding bond-bending springs to control the angles between adjacent nodes [45].

To extend a 2D triangular lattice to 3D, a triangular prism network is constructed from two layers of triangular lattice elements. The layers are separated by a distance equal to the length of triangle edges and are connected by springs between the nearest (with spring constant k_2) and next-nearest neighbor nodes (with spring constant k_3) (Fig. 3b). Using the linear elasticity theory, spring constants are set as follows, $k_1 = 2k$, $k_2 = k$, and $k_3 = 2k/3$, yielding Lamé constants $\mu = \lambda = 2k/\sqrt{3}a_0$. Thus, Young's modulus is $E = 5k/\sqrt{3}a_0$, Poisson's ratio is $\nu = 1/4$, and the mass of each spring nodes is $M = \rho_s \sqrt{3}a_0^3/2$.

LSM can be used to obtain both dynamic and static steady-state solutions. In the latter case, the equations of motion should be damped to reach the equilibrium state that satisfies the applied boundary conditions. A damping force can be set proportional to the node velocity $\mathbf{F}_i^d = -\alpha \mathbf{v}_i$, where α is the damping constant. This damping force vanishes at steady state.

2.2.1 Model for Thin Membranes

LSM can be applied to model thin membranes. When the thickness of the membrane is small compared to the membrane extent, the membrane can be modeled as

an elastic sheet with bending rigidity. There are two approaches to introduce bending rigidity in a membrane. For a 2D triangular lattice, one way is to add bending springs among all triplets jij', where $j' = j+3$ (i.e., j' denotes the neighbor opposite to neighbor j) [46]. This approach also refers to bond-bending model (BB) [47]. The bending energy stored in node i is $U_{bending,i} = \sum_{jij'=1}^{3} k_b(\cos\theta_{jij'} - \cos\theta_0) = \sum_{jij'=1}^{3} k_b\left(\frac{\mathbf{r}_{ij}\cdot\mathbf{r}_{ij'}}{|\mathbf{r}_{ij}||\mathbf{r}_{ij'}|}+1\right)$, where k_b is the bending spring constant, and $\theta_0 = \pi$ is the spontaneous or initial angle between bonds ji and ij'.

For small deflections, following a procedure similar to that used for linearized stretching springs, we obtain the bending energy density $\phi_{bending} = \frac{9k_b}{16}\left(w_{xx}^2 + w_{yy}^2 + \frac{2}{3}w_{xx}w_{yy} + \frac{4}{3}w_{xy}^2\right)$, where w is the displacement perpendicular to the membrane surface. Comparing with the continuum equation for small-deflection plate bending [48] given by, $\phi_{bending} = \frac{D}{2}\left[(w_{xx}+w_{yy})^2 - 2(1-\nu)(w_{xx}w_{yy} - w_{xy}^2)\right]$, we find that bending rigidity or modulus is $D = 3\sqrt{3}k_b/4$ when $\nu = 1/3$, where $D = \frac{E_S h^3}{12(1-\nu^2)}$ can be defined as a thin plate of thickness h. The forces acting on nodes j, j', and i due to the bending of triplets jij' are $\mathbf{F}_j = -\frac{k_b}{|\mathbf{r}_{ij}||\mathbf{r}_{ij'}|}\left(\mathbf{r}_{ij'} - \frac{(\mathbf{r}_{ij}\cdot\mathbf{r}_{ij'})}{r_{ij}^2}\mathbf{r}_{ij}\right)$, $\mathbf{F}_{j'} = -\frac{k_b}{|\mathbf{r}_{ij}||\mathbf{r}_{ij'}|}\left(\mathbf{r}_{ij} - \frac{(\mathbf{r}_{ij}\cdot\mathbf{r}_{ij'})}{r_{ij'}^2}\mathbf{r}_{ij'}\right)$, and $\mathbf{F}_i = -(\mathbf{F}_j + \mathbf{F}_{j'})$, respectively. For a 2D square lattice, similarly, we derive the relation of bending rigidity and bending spring constant

as $k_{b1} = 2D/3$, $k_{b2} = D/3$, where k_{b1} is associated with the nearest-neighbor connections, and k_{b2} indicates the diagonal connections.

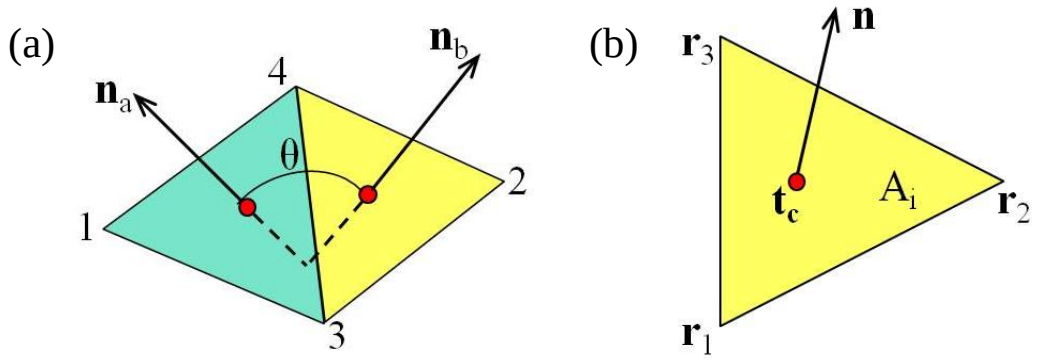

Figure 4 (a) A bending element with dihedral angle θ. (b) Sketch of a triangular element of springs.

Another way to include bending contribution is to consider the change of dihedral angle of adjacent pairs of triangles (abbreviated as DA for this model) [49]. The bending contribution to the Helmholtz free energy of the system is $U_{bending} = \sum_i k_b[1-\cos(\theta_i - \theta_0)]$, where θ_i is the instantaneous angle between two adjacent triangles with the common edge i, and θ_0 is the spontaneous angle. The relationship between the bending spring constant and the macroscopic bending rigidity can be derived for the case of a spherical shell, which gives $D = \sqrt{3}k_b/2$ [50]. Similarly, for a square lattice, we obtain $k_b = \sqrt{2}D/3$. Figure 4a shows two equilateral triangles with the angle θ between two triangle normals $\mathbf{n}_a$ and $\mathbf{n}_b$. The force acting on the nodes can be derived from the bending energy, $\mathbf{F}_1 = \alpha \frac{|\mathbf{r}_{34}|}{n_a^2}\mathbf{n}_a$, $\mathbf{F}_2 = \alpha \frac{|\mathbf{r}_{34}|}{n_b^2}\mathbf{n}_b$,

$\mathbf{F}_3 = \alpha\left[\frac{(\mathbf{r}_{41}\cdot\mathbf{r}_{34})\mathbf{n}_a}{|\mathbf{r}_{34}|n_a^2} + \frac{(\mathbf{r}_{42}\cdot\mathbf{r}_{34})\mathbf{n}_b}{|\mathbf{r}_{34}|n_b^2}\right]$, and $\mathbf{F}_4 = -\alpha\left[\frac{(\mathbf{r}_{31}\cdot\mathbf{r}_{34})\mathbf{n}_a}{|\mathbf{r}_{34}|n_a^2} + \frac{(\mathbf{r}_{32}\cdot\mathbf{r}_{34})\mathbf{n}_b}{|\mathbf{r}_{34}|n_b^2}\right]$, where $\mathbf{n}_a = \mathbf{r}_{31}\times\mathbf{r}_{41}$ and $\mathbf{n}_b = \mathbf{r}_{42}\times\mathbf{r}_{32}$ are the area weighted normals, and $\alpha = -k_b(\sin\theta\cos\theta_0 - \cos\theta\sin\theta_0)$. Here, $\cos\theta = \frac{\mathbf{n}_a\cdot\mathbf{n}_b}{|\mathbf{n}_a||\mathbf{n}_b|}$, and $\sin\theta = \pm\sqrt{1-\cos^2\theta}$ taken with the positive sign if $(\mathbf{n}_a - \mathbf{n}_b)\cdot(\mathbf{t}_a - \mathbf{t}_b) \geq 0$ and with the negative sign otherwise; $\mathbf{t}_a$ and $\mathbf{t}_b$ are the center of mass vectors of triangles *a* and *b*, respectively.

2.2.2 Modeling Solid Body Dynamics

To capture the dynamics of solid object, we integrate Newton's equation of motion, $\mathbf{F}_i = M_i\,\partial^2\mathbf{r}_i/\partial t^2$, using the velocity Verlet algorithm [51]. Here, $\mathbf{F}_i$ is the total force acting on the node *i* including the spring force, the hydrodynamic force, and any external forces. The velocity Verlet scheme is a second-order in time and fourth order in space finite difference approximation to the equations of motion. This allows us to obtain the accurate velocity at the interface nodes to couple the solid and fluid systems. The Verlet algorithm updates the position, velocity and acceleration of the nodes in the following manner,

$$\mathbf{a}_i(t) = \mathbf{F}_i(\mathbf{r}_i, t)/M_i$$

$$\mathbf{v}_i(t+\Delta t/2) = \mathbf{v}_i(t) + \frac{1}{2}\mathbf{a}_i(t)\Delta t$$

$$\mathbf{r}_i(t+\Delta t/2) = \mathbf{r}_i(t) + \mathbf{v}_i(t+\Delta t/2)\Delta t$$

$$\mathbf{a}_i(t+\Delta t) = \mathbf{F}_i(\mathbf{r}_i, t+\Delta t/2)/M_i$$

$$\mathbf{v}_i(t+\Delta t) = \mathbf{v}_i(t+\Delta t/2) + \frac{1}{2}\mathbf{a}_i(t+\Delta t)\Delta t\,, \qquad (20)$$

where $\mathbf{v}_i$ and $\mathbf{a}_i$ are the velocity and acceleration of the node *i*, respectively.

For a rigid object, we need to sum up the forces on each node to obtain the total force and torque acting on the body. The kinematics of rigid body motion yields a formula for the acceleration of node *i* on the body in terms of the position $\mathbf{r}_i$ as $\mathbf{F}_i = M_i(\mathbf{F}/\sum M_i + \boldsymbol{\omega}\times\boldsymbol{\omega}\times(\mathbf{r}_i - \mathbf{R}) + \boldsymbol{\alpha}\times(\mathbf{r}_i - \mathbf{R}))$. Here, $\mathbf{F}$ is the total force on the body, $\mathbf{F}_i$ is the newly redistributed force on each node, $\mathbf{R}$ is the position of the center of mass, $\boldsymbol{\omega}$ and $\boldsymbol{\alpha}$ are the angular velocity and angular acceleration of the rigid body, respectively. The angular acceleration is calculated from Euler's equation, $\frac{d}{dt}(\mathbf{I}\cdot\boldsymbol{\omega}) = \mathbf{M}$, in an inertial frame of reference, where $\mathbf{I}$ is the moment of inertia tensor calculated in the inertia frame and $\mathbf{M}$ is the total torque. For a rigid body, the relative displacements of the nodes must be zero. Therefore, to ensure this constraint, there include a 'penalty' force of the form $\mathbf{F}_i^p = -\sum_j k_{ij}(r_{ij} - r_{ij}^0)\hat{\mathbf{r}}_{ij}$. This force is added to the nodes at each LSM iteration. Here, j is the index of nodes connected to node i, k_{ij} is the spring constant between the nodes, r_{ij} and r_{ij}^0 are the current and initial displacement between the nodes respectively, and $\hat{\mathbf{r}}_{ij}$ is the unit direction vector of pair ij.

Considered numerical stability, the time step should be chosen that it is less than the time needed for elastic wave propagation through lattice element. This leads to the condition $\Delta t < \Delta x/V_p$, where $V_p = \sqrt{(K + 4G/3)/\rho_s}$ is the P-wave velocity [52] and Δx is the lattice spacing. Furthermore, for deformable solid, we need to maintain $\Delta x > 1$ (in LB units), which prevents large fluctuations in the force of the fluid on the lattice spring nodes due to the discretization [53]. For a rigid solid, we do not have this restriction,

since the total hydrodynamic force is redistributed to all the nodes on the surface and the solid follow the motion of a rigid body. If the solid is stiff, the P-wave velocity V_p may require Δt smaller than 1. In this case, we perform several LSM iterations for each LBM cycle, thus reducing Δt sufficiently to stabilize the simulations.

2.3 Solid-fluid Coupling

To simulate the hydrodynamic interactions between fluid and solid, the model must incorporate an appropriate boundary condition at the solid-fluid interface. The simulation proceeds as following: first, the LSM system (solid) is updated by calculating the forces that are acting on the LSM nodes due to the springs, the surrounding fluid and external field. Next, new positions, velocities, and accelerations of the LSM nodes are calculated using the Verlet algorithm. During the update of LBM system, we first find LBM links intersecting the solid-fluid interface. We then obtain the velocities at the intersection points from neighboring LSM nodes (see Fig. 5a). Next, the appropriate boundary rule is applied to these boundary nodes, which ensures no-slip and no-penetration conditions at the interface.

The most popular boundary rule in LBM is the linked bounce back (LBB) rule [23], where the momentum of a fluid distribution function reverses when fluid collides with a solid surface. The location of boundary node is the half-way between fluid nodes, so it will portray a curved boundary as a series of steps. It has been shown that this boundary rule is of the first order accurate for solid surfaces oriented at arbitrary angles [23].

Recently, alternative methods to retain second order accuracy have been proposed [24], which include linear (LI) and quadratic (QI) interpolation rules, multi-reflection rule

(MR), and equilibrium interpolation link bounce-back (EI) rule. However, all these rules have some drawbacks, either the location of the no-slip boundary walls depends on fluid viscosity (LI and QI) or they requires information from multiple fluid nodes (QI and MR). In our simulations, we use two boundary rules: LI and EI rules.

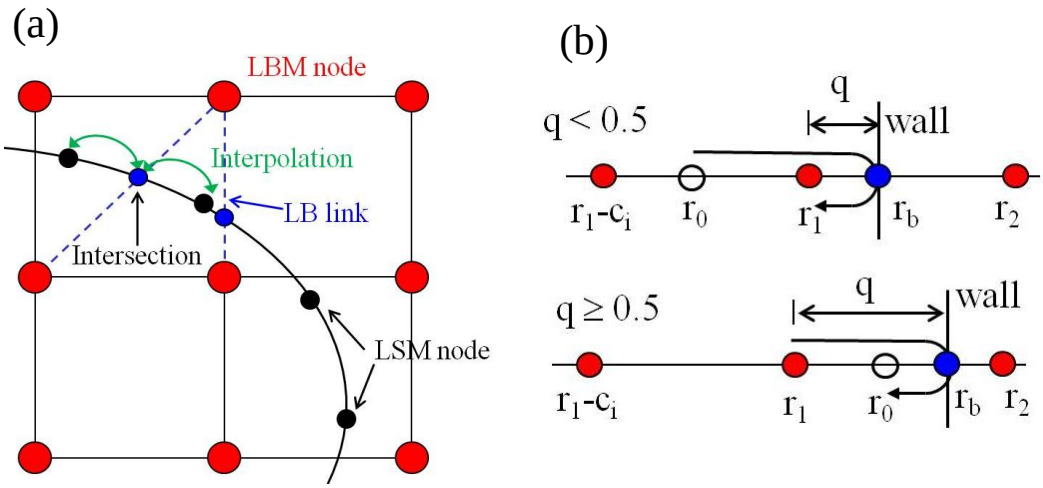

Figure 5 (a) Location of boundary nodes for a curved surface. (b) Schematic diagrams of the linear interpolation rule; q is the distance of the fluid node $\mathbf{r}_1$ from the boundary node $\mathbf{r}_b$, normalized by the lattice spacing.

The solid surface is not always located midway between two LBM nodes. Second-order accuracy therefore requires the use of an interpolation. In LI rule, we follow the scheme that is developed by Bouzidi *et al*. [54] as illustrated in Figure 5b. For $q<1/2$, we obtain $f_i^*(\mathbf{r}_0,t)$, which is the postcollision distribution at the position $\mathbf{r}_0$, by linear interpolation between $f_i^*(\mathbf{r}_1-\mathbf{c}_i,t)$ and $f_i^*(\mathbf{r}_1,t)$. After propagation step and being reflected at the boundary node, the interpolated distribution will end up at node $\mathbf{r}_1$ with a velocity in the opposite direction i'. Hence,

$$f_{i'}(\mathbf{r}_1,t+\Delta t)=2qf_i^*(\mathbf{r}_1,t)+(1-2q)\,f_i^*(\mathbf{r}_1-\mathbf{c}_i,t),\ q<1/2\,. \qquad (21)$$

For $q \geq 1/2$, we first propagate the fluid particle at node $\mathbf{r}_1$, such that it ends up at the position $\mathbf{r}_0$, i.e., $f_{i'}(\mathbf{r}_0, t+\Delta t) = f_i^*(\mathbf{r}_1, t)$. We then obtain $f_{i'}(\mathbf{r}_1, t+\Delta t)$ by linear interpolation between $f_{i'}(\mathbf{r}_0, t+\Delta t)$ and $f_{i'}(\mathbf{r}_1 - \mathbf{c}_i, t+\Delta t)$, i.e.

$$f_{i'}(\mathbf{r}_1, t+\Delta t) = \frac{1}{2q} f_i^*(\mathbf{r}_1, t) + \frac{2q-1}{2q} f_{i'}^*(\mathbf{r}_1, t), q \geq 1/2. \quad (22)$$

Although the linear interpolation scheme leads to second-order accuracy at the boundary, the location of the interface depends on fluid viscosity in a way that cannot be easily estimated as it is for the bounce-back rule. For EI rule developed by Chun and Ladd [24], a separation of equilibrium and nonequilibrium parts provides a viscosity-independent boundary rule. This is because the viscosity dependence of hydrodynamic boundary only comes from the nonequilibrium distribution. The decomposition must be done before the propagation step, so the equilibrium part is interpolated first and the nonequilibrium part is bounced back. For the case $q < 1/2$, we use the neighboring node at $\mathbf{r}_1 - \mathbf{c}_i$ for the interpolation. Similarly to the standard linear interpolation, we obtain

$$f_{i'}^{eq}(\mathbf{r}_1, t+\Delta t) = 2q f_i^{eq}(\mathbf{r}_1, t) + (1-2q) f_i^{eq}(\mathbf{r}_1 - \mathbf{c}_i, t), q < 1/2. \quad (23)$$

On the other hand, for $q \geq 1/2$, we use the expected equilibrium distribution at the boundary node $\mathbf{r}_b$ to interpolate,

$$f_{i'}^{eq}(\mathbf{r}_1, t+\Delta t) = \frac{1-q}{q} f_i^{eq}(\mathbf{r}_1, t) + \frac{2q-1}{q} f_i^{eq}(\mathbf{r}_b, t), q \geq 1/2, \quad (24)$$

where $f_i^{eq}(\mathbf{r}_b, t)$ is the equilibrium distribution corresponding to the local velocity of the interface $\mathbf{u}_b$. If the interface is stationary, $f_i^{eq}(\mathbf{r}_b, t) = a^{c_i}\rho_0$. The final distribution at the

fluid node $f_{i'}(\mathbf{r}_1, t+\Delta t)$ should includes the nonequilibrium distribution regardless of q, which is obtained from the bounce-back rule $f_{i'}^{neq}(\mathbf{r}_1, t+\Delta t) = f_i^{neq}(\mathbf{r}_1, t)$.

For a moving interface, we have to account for the velocity $\mathbf{u}_b$ of the solid material at the interface. This leads to an additional term $-\frac{2a^{c_i}\rho \mathbf{c}_i \cdot \mathbf{u}_b}{c_s^2}$ in the above equations that is proportional to the velocity $\mathbf{u}_b$, where ρ is the local density. When a particle collides with an impenetrable wall, it reverses its momentum normal to the wall and gains an additional momentum due to the wall velocity. Thus for LI rule, the distributions are

$$f_{i'}(\mathbf{r}_1, t+\Delta t) = 2q f_i^*(\mathbf{r}_1, t) + (1-2q) f_i^*(\mathbf{r}_1 - \mathbf{c}_i, t) - \frac{2a^{c_i}\rho \mathbf{c}_i \cdot \mathbf{u}_b}{c_s^2}, q < 1/2$$

$$f_{i'}(\mathbf{r}_1, t+\Delta t) = \frac{1}{2q} f_i^*(\mathbf{r}_1, t) + \frac{2q-1}{2q} f_{i'}^*(\mathbf{r}_1, t) - \frac{2a^{c_i}\rho \mathbf{c}_i \cdot \mathbf{u}_b}{c_s^2}, q \geq 1/2. \quad (25)$$

The intersection point may not overlap with the lattice spring node. In this case, the velocity $\mathbf{u}_b$ can be obtained using a linear interpolation between the neighboring lattice spring nodes of the triangulated surface.

As a result of the bounce-back process, fluid exerts a force on the solid-fluid interface. This force is taken to be equal to the rate of exchange in momentum that takes place as the fluid particle is reflected at the solid-fluid interface,

$$\mathbf{F}_b(\mathbf{r}_b, t+\frac{1}{2}\Delta t) = \frac{\Delta x^3}{\Delta t}\left[f_i^*(\mathbf{r}_1, t) + f_{i'}^*(\mathbf{r}_1, t+\Delta t)\right]\mathbf{c}_i. \quad (26)$$

It was recently found that this formula gives an error in the quadratic terms in the distribution function that breaks Galilean invariance [55]. This error cancels out when simulating fluid-filled thin shells, in which a corresponding internal fluid particle

interacts with the solid surface. However, when one models a solid body without an internal fluid, a corrected bounce-back operation term needs to be used, $\overline{\mathbf{F}}_b = \mathbf{F}_b - 2\rho a^{c_i}\left[1+\frac{1}{2c_s^4}(\mathbf{c}_i\cdot\mathbf{u}_b)^2-\frac{1}{2c_s^2}u_b^2\right]\mathbf{c}_i$. The hydrodynamic force $\overline{\mathbf{F}}_b$ is then distributed among the neighboring lattice spring nodes, such that the normal and tangential forces on the interface are conserved [53].

CHAPTER 3

MODEL VALIDATION

In this section, the accuracy of our hybrid fluid-structure interaction model presented in the previous chapter is examined and the model is validated by simulating fluid flow around solid particles. This serves as a basis for the subsequent researches on the flow of particle suspensions.

3.1 Flow Past Sphere in Unbounded Flow

We study the convergence of our model by placing a solid sphere at the center of a cubic domain with size $L = 5a$, where a is the radius of the sphere. In our simulation, fluid is driven by a pressure gradient with a constant particle Reynolds number $\mathrm{Re}_p = Ua/\nu = 0.05$. Periodic boundary conditions are used in all directions. The analytic solution [56] for drag force acting on a periodic array of spheres forming a cubic lattice in creeping flow is given by $F = K 6\pi\mu a U$, where the correction coefficient $K^{-1} = 1 - 1.7601c^{1/3} + c - 1.5593c^2 + O(c^{8/3})$, c is the volume fraction of a sphere in the cubic domain, and U is the mean velocity at periodic boundary. This analytical solution is valid for $c << 1$.

The lattice spacing of both LSM and LBM are refined sequentially, and the relative error of the force is computed by comparing the simulation results with the analytical solution. The relative node spacing is defined as lattice spacing divided by domain size L. The results are shown in Figure 6a, indicating that our simulations converge to the analytical solution. The slope of 1.86 obtained in the simulations is close

to the theoretical accuracy of LBM, which is of the second order accuracy, and also indicates the boundary condition at fluid-solid interface is of the second order accuracy.

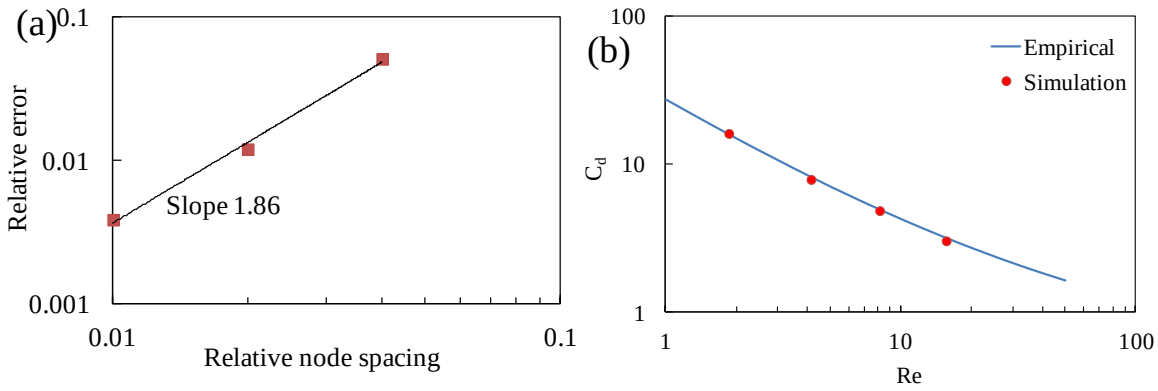

Figure 6 (a) Convergence of relative errors of drag force on a fixed sphere in unbounded Stokes flow. (b) Drag coefficient of a periodic array of settling spheres at different Re.

This simulation tests the boundary condition when the solid sphere is stationary. In order to examine the situation when the interface moves across the lattice, we impose a constant velocity on the solid sphere. Similarly, we compare our simulation with the analytical solution (here, U is relative velocity between fluid and solid), and find the relative error is within 1.2% for $a=10$ (LB unit). No force or velocity fluctuations are observed in the simulation, indicating a sub-grid scale resolution for our coupled model.

In order to probe the utility of our method for simulating moving boundaries in an inertial flow, we allow a periodic array of spheres to settle at larger Reynolds numbers. In the simulation, a sphere was placed in a cubic box of $80a\times32a\times32a$ with periodic conditions on all sides. An empirical equation for the drag coefficient is given by White [57], $C_d \approx \frac{24}{\mathrm{Re}}+\frac{6}{1+\sqrt{\mathrm{Re}}}+0.4$, where $F=0.5C_d\rho U^2\pi a^2$, U is the relative velocity between sphere and fluid, and Re is calculated based on particle diameter. This empirical

formula fits a large amount of data available within 10% error. Our results are shown in Figure 6b, which agree well with the empirical expression.

3.2 Effect of Time Relaxation Parameter on Fluid-solid Coupling

To probe the accuracy and stability of different LBM boundary rules, we examine the steady Stokes flow through a cubic array of spheres. The cubic domain size $L = 5a$ is used in our simulations, where $a = 10$ is the radius of the sphere. We evaluate the viscosity dependence of the computed drag force by using different fluid-solid coupling schemes. MRT-LI, MRT-EI, Ladd-LI, Ladd-EI, BGK-LI are respectively used to denote the MRT scheme with linear interpolation, MRT with equilibrium interpolation, Ladd's scheme with linear interpolation, Ladd's scheme with equilibrium interpolation, and BGK scheme with linear interpolation boundary conditions (see Chapter 2). For MRT model, the eigenvalues of collision operator are chosen as $s_4 = s_{16} = -2 - \lambda$, $s_1 = s_2 = s_9 = s_{10} = s_{13} = \lambda$, where λ is the relaxation time related to viscosity; this corresponds to $w = 0.5$ as in [24].

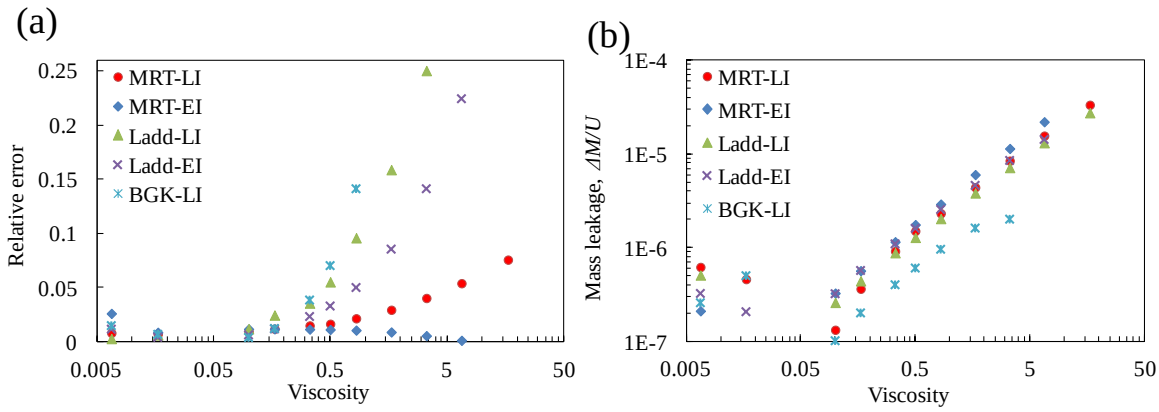

Figure 7 (a) Relative error in drag force for a simple cubic array of spheres as a function of fluid viscosity. (b) Viscosity dependence of the mass leakage for different schemes.

In LBM, the fluid viscosity can only be changed by varying relaxation time. Figure 7a shows the relative error of the drag force as a function of fluid viscosity. The results indicate that the data obtained using MRT scheme are much less dependent on viscosity than those obtained by Ladd scheme and BGK scheme. The MRT-EI scheme is almost independent of viscosity. MRT-LI and Ladd-EI schemes have acceptable error when the viscosity is less than 0.5. BGK-LI scheme has the worst results and is only accurate when $\mu \le 0.2$. All these schemes have minimum errors when $\mu = 0.1$. We conclude that MRT-EI scheme should be used to model highly viscous fluids. For low viscosity, Ladd scheme is recommended since its run time is about 30% faster than MRT scheme.

A major drawback of the interpolation schemes is that the total fluid mass is not always exactly conserved. For special cases, such as a channel flow with the walls symmetrically placed on the grids, there is no mass leakage since the gain and loss of mass from the interpolations are exactly cancelled each other [24]. However, solid surfaces are typically not located in symmetric positions, so that fluid mass tends to keep increasing or decreasing over time depending on the position of the fluid-solid boundaries. The mass leakage per time step, $\Delta M = \sum_j \left(\rho(\mathbf{r}_j, t) - \rho_0\right) \Big/ \Delta t \sum \rho_0$ is roughly constant for a given configuration and proportional to the average velocity of fluid. The results in Figure 7b show that $\Delta M/U$ is negligible when $\mu \le 0.5$ for all schemes, but increases linearly with viscosity. It should be noted that even though the mass gain or loss increases with time, we did not observe any variation of velocity field due to mass leakage, which is similar to the results reported in [24].

3.3 Frequency-dependent Rotational Friction Coefficient

To model the dynamics of a solid particle, different approaches can be used with regard to including the fluid located in the particle interior into the model. As first suggested by Ladd [16], a particle can be treated as a solid shell of mass m_0 and moment of inertia I_0, filled with a fluid. It has been shown that this model is not accurate to model the dynamics of solid particle under certain situations [18].

Ladd [16] investigated the influence of the internal fluid on the rotational dynamics of a single spherical particle. For high-frequency rotation ($\Omega >> \nu/a^2$, where Ω is the frequency, ν is the viscosity, and a is the particle radius), the internal fluid makes no contribution and the particle displays the same behavior as a rigid particle with the moment of inertia I_0. For low-frequency rotation ($\Omega << \nu/a^2$), the internal fluid contributes essentially as a rigid body and the particle acts as a rigid particle with the combined mass and moment of inertia of the shell plus the internal fluid.

It is worth noting that the internal fluid can be assigned a higher viscosity to ensure the relaxation to the long time limit. However, at short times, the inertial lag of the fluid is noticeable and does affect the dynamics. For this reason, several schemes have developed to eliminate the effect of internal fluid [10, 18]. We follow the method developed in [18] that treat the internal fluid nodes as virtual nodes. The virtual nodes are updated as normal nodes at the collision step in LBM, but they do not impose torque and force on the solid particle interface. In contrast, a solid shell containing internal fluid is implemented by summing up hydrodynamic forces exerted by both internal and external fluids at the boundary nodes. Therefore with small change, this method is able to simulate both solid particles and fluid-filled capsules.

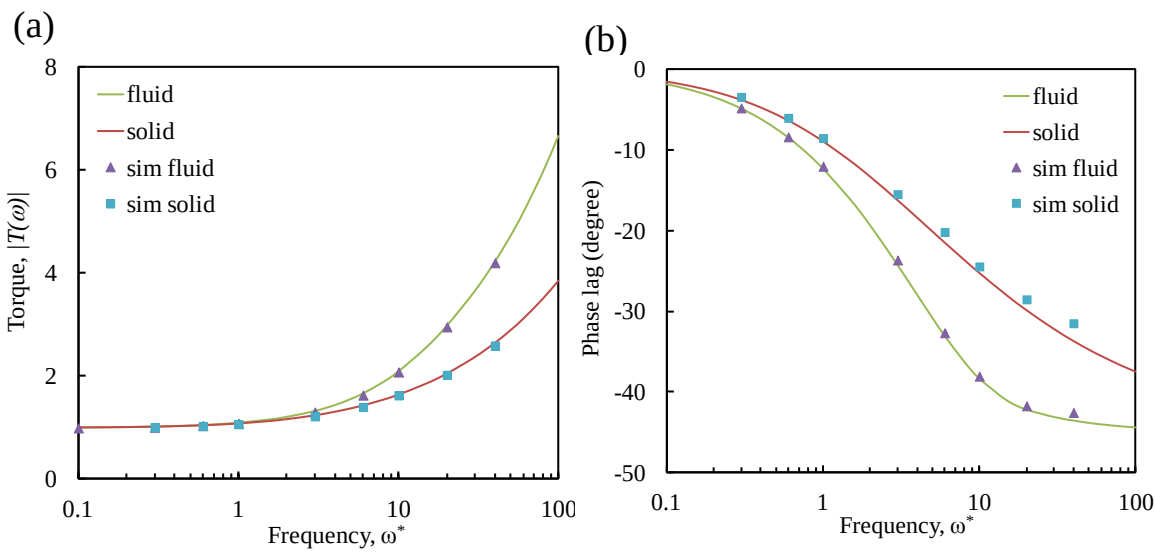

Figure 8 (a) Frequency-dependent torque on a rotating sphere with and without internal fluid. The torque on the sphere is normalized by $\xi_0\Omega_0$. (b) Phase lag between oscillations and torque on a rotating sphere with and without internal fluid.

To validate this method, we consider an unsteady motion of an isolated sphere in the limit of zero Reynolds number. We begin by investigating the motion of a sphere undergoing small-amplitude rotational oscillations $\Omega(t)=\Omega_0\cos(\omega t)$. In this case, the internal fluid exerts a frequency-dependent torque $T(\omega)$ on the particle. The motion of particle can be analyzed theoretically [58] to separately obtain the internal and external contributions $T_{ext}=-\xi_0\Omega_0\left(1-\dfrac{i\omega^*}{3(1+\sqrt{-i\omega^*})}\right)$ and $T_{\text{int}}=\xi_0\Omega_0\left(1-\dfrac{i\omega^*}{3(1-\sqrt{i\omega^*}\cot\sqrt{i\omega^*})}\right)$ in terms of the reduced frequency $\omega^*=\omega a^2/\nu$ and the zero-frequency drag coefficient $\xi_0=8\pi\mu a^3$.

In our simulations, we impose a sinusoidal rotational motion on the particle and calculate the magnitude and phase lag of the viscous torque due to the fluid. The shell mass and the moment of inertia are set to values of a solid sphere with the same density

as the fluid. Our results are shown in Figure 8. We find that the phase lag slightly underestimates the theory at sufficiently high frequencies when the period of oscillation ($2\pi/\omega^*$) is less than 10 LBM time steps. The accuracy can be increased by increasing the size of the sphere or by decreasing the viscosity of the fluid. At low frequency, the effect of the internal fluid on the magnitude of the torque is minor. However, the contribution to the phase lag is noticeable. Our method can accurately model the low-frequency effects of the internal fluid in close agreement with the theory prediction.

3.4 Drag and Lift Forces on Sphere in Shear Flow

It is well-known that particles carried by a viscous fluid along a wall are subjected to a lift force normal to the flow direction. For a vanishing small Reynolds number, at the leading order O(0) the lift force on a sphere is zero due to the linearity of the Stokes equations. At the next order O(1), fluid inertia results in a lift force normal to the wall [59]. The calculation of lift force is a highly sensitive test of the model accuracy and we use this test to examine the properties of our model.

Recently, Samir [59] used a regular perturbation expansion method to study the lift force on a sphere at a low Reynolds number. For a sphere fixed in a linear shear flow, he provides an accurate fitting formula valid for $\mathrm{Re} << 1$ and distance $1.01 \le l/a \le 100$,

$$\ln L_S = \frac{2.0172\lambda^5 + 3.4562\lambda^4 + 3.9608\lambda^3 + 2.6728\lambda^2 - 0.15728\lambda + 0.01386}{\lambda^4 + 0.96328\lambda^3 + 1.264\lambda^2 - 0.07648\lambda + 0.006228} \quad , \quad \text{where}$$

$\lambda = \ln(l/a)$, l is the distance from particle center to the wall, a is particle radius, $L_S = F_L / \rho a^4 \dot{\gamma}^2$ is the lift coefficient, and $\dot{\gamma}$ is the shear rate.

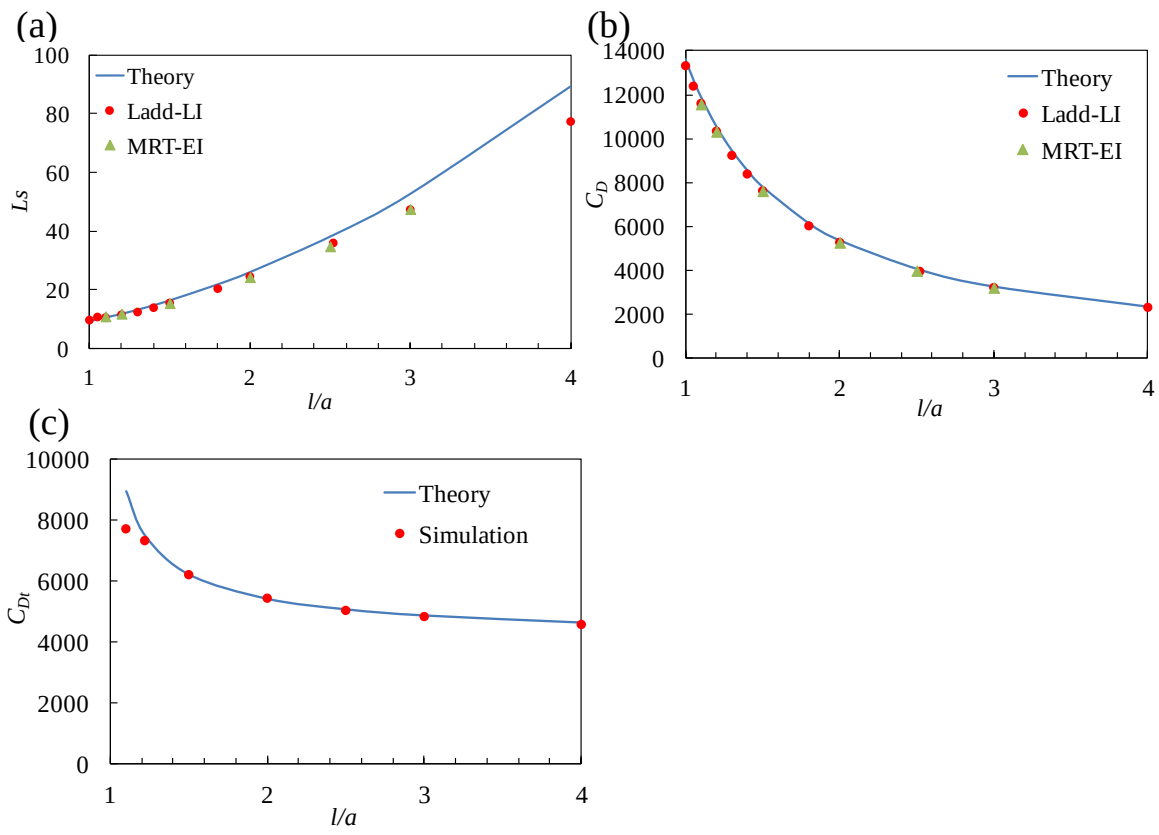

Figure 9 (a) Lift force on a fixed sphere in linear shear flow and comparison with the theory. (b) Drag force on a fixed sphere in linear shear flow. (c) Drag force on a moving sphere parallel to the wall in a quiescent fluid.

In the simulations, the grid resolution is set $a=5$, and the domain size is $40a\times 40a\times 40a$. Besides the standard Ladd-LI scheme, MRT-EI scheme with viscosity $\mu=5/3$ is also examined in these tests. Figure 9a compares our simulations with the theory for the lift force on a fixed sphere in a shear flow. Our results are close to the theory for $l/a<2$. In the limiting case when the particle is in contact with the wall, Krishnan and Leighton [60] obtained an analytical value $L_S=9.257$. In this limit, our computational result is 9.7, which is within a 5% error. When the particle is far away from the wall, our results begin to deviate from the theory. It is because the theory is derived for semi-infinite domain with a single wall. In contrast, the effect of the top wall

cannot be neglected in our simulations. So our simulation underestimates the lift force when $l/a > 2$.

We also compare the drag force with the correlation provided by Zeng [61], and our simulations show good agreement for both computational schemes (Fig. 9b). An accurate fit for the low Reynolds number drag force on a stationary particle in a shear flow is given by [61], $C_{Ds} = \frac{24}{\mathrm{Re}}\left(1 + 0.138\exp(-2\delta) + \frac{9}{16(1+2\delta)}\right)$, where $\delta = 0.5(l/a - 1)$, $\mathrm{Re} = 2al\dot{\gamma}/\nu$, and $C_{Ds} = 2F/\rho\pi a^2 l^2 \dot{\gamma}^2$.

Additionally, we test our method by simulating the case when a sphere moves parallel to a wall in a quiescent fluid. For a translating sphere, the correlation for the lift force is given by [59], $L_T = \frac{1.77(l/a)^4 + 14.48(l/a)^3 + 45.52(l/a)^2 - 42.67(l/a) + 9.243}{(l/a)^4 + 8.14(l/a)^3 + 23.59(l/a)^2 - 16.54(l/a)}$, where $L_T = F_L/\rho a^2 U_p^2$ and U_p is the translating velocity of particle. The corresponding drag coefficient is [61], $C_{Dt} = \frac{24}{\mathrm{Re}_t}\left(1.028 - \frac{0.07}{1+4\delta^2} - \frac{8}{15}\ln\left(\frac{270\delta}{135+256\delta}\right)\right)$, where $\mathrm{Re}_t = 2aU_p/\nu$. It should be noted that when the sphere is allowed to move parallel to the wall, the lift force would be substantially reduced compared to a stationary sphere.

In our simulations, we find the lift force on the sphere fluctuates in a periodic way. These fluctuations are related to the relative position of the sphere with respect to the LBM grid nodes. Similar behavior has been previously reported [62]. We note, however, that oscillations of the drag force are negligible small. By averaging the lift force over time required to move over the distance equal to single grid spacing, we find the lift force that agrees with the theory within 4% error. For the drag force, good

agreement is found when the particle is at least one grid unit away from the wall (Fig. 9c). For smaller distances between particle and wall, the lubrication force should be included into the model. There are several ways to incorporate lubrication forces into LBM [63, 64]. However, we do not consider the lubrication force in our model since we focus on the flow regimes where the distance between a solid particle and a wall is greater than one lattice unit.

3.5 Lattice Spring Model Validation

When the thickness of a membrane is small compared to the capsule diameter, the membrane can be modeled as an elastic sheet with surface shear elastic modulus G_S, area dilation modulus K_S, surface Young's modulus E_S, and Poisson's ratio ν_S. Only two of those moduli are independent, whereas other can be found using the relations of elasticity $K_S = G_S(1+\nu_S)/(1-\nu_S)$ and $E_S = 2G_S(1+\nu_S)$. When the membrane is isotropic, the principal directions of deformation and stress are co-linear. A simple way to express the membrane constitutive law is to relate the principle tensions (forces per unit area) T to the principal extension ratio in the membrane plane $\lambda = L/L_0$, where L is the final length and L_0 is the initial length of the material. For a uniaxial stretch, for example, in the x_1 direction $T_1 \neq 0$, in the limit of small deformation, $T_1 = E_S(\lambda_1^2 - 1)/2 = E_S\varepsilon_1$, where ε_1 is the Green strain. The area dilation modulus can be obtained from isotropic stretching ($T_1 = T_2 = T$). Its value in the limit of small deformations is given by $T = K_S(\lambda_1\lambda_2 - 1) = K_S\Delta S/S_0$, where $\Delta S/S_0$ is the relative area change [42].

A number of constitutive laws have been proposed to model thin hyperelastic membranes. Depending on the constitutive law, different materials can be modeled

including relatively large deformations. For example, models with a strain softening feature can be used for gelled membranes that exhibit rubber-like elasticity or models with strain hardening can be employed to study membranes made of a polymerized network with strong covalent links. For each law discussed below, we provide only an expression for T_1 as a function of the deformation, whereas a corresponding expression for T_2 can be obtained by interchanging the indices 1 and 2.

In the limit of small deformations, all constitutive laws reduce to the Hooke's law, $T_1^H = \frac{G_S}{1-\nu_S}\left[\lambda_1^2 - 1 + \nu_S(\lambda_2^2 - 1)\right]$. An area incompressible membrane is characterized by $\nu_S = 1$. For large deformations, a widely used law is the neo-Hookean law (NH) that describes the behavior of an infinitely thin sheet of a three-dimensional isotropic material that is volume incompressible, $T_1^{NH} = \frac{G_S}{\lambda_1\lambda_2}\left[\lambda_1^2 - \frac{1}{(\lambda_1\lambda_2)^2}\right]$. For small deformations, the corresponding Poisson's ratio is 1/2. Another law (SK) has been derived for 2D materials has independent surface shear and area dilation moduli [65], $T_1^{SK} = G_S\left[\lambda_1(\lambda_1^2 - 1)/\lambda_2 + C\lambda_1\lambda_2(\lambda_1^2\lambda_2^2 - 1)\right]$. In the limit of small deformations, the corresponding parameters are $\nu_S = C/(C+1)$, and $K_S = G_S(1+2C)$.

For large deformations, the condition $T_2 = 0$ provides an expression of λ_2 as a function of λ_1 that gives an expression for the tension T_1 for different constitutive laws. In this way, the analytical solution can be obtained. Under large uniaxial stretch, the variation of T_1 with ε_1 is nonlinear for NH and SK laws.

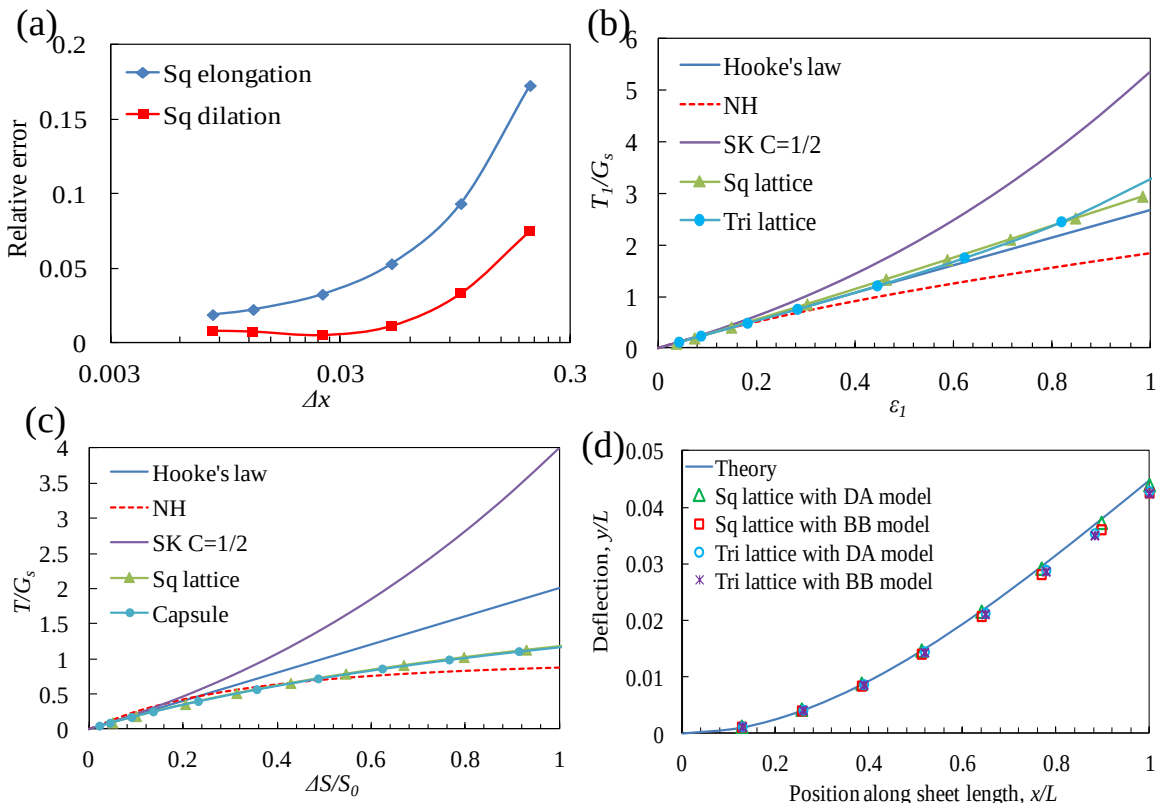

Figure 10 (a) Relative error of elastic moduli as a function of mesh spacing under uniaxial extension and isotropic extension. (b) Tension-strain relationship under uniaxial elongation from continuum theories and spring models. (c) Tension-strain relationship under isotropic dilation from continuum theories and spring models. (d) Deflection of a free end loaded 2D sheet from the theory and spring models.

We calculate the mechanical properties of the LSM and compare them with the continuum models. We first examine the effect of mesh size Δx by investigating the deformation of a 2D spring network with square shape under uniaxial and isotropic extension. Figure 10a shows the values of $|E - E_S|/E_S$ and $|K - K_S|/K_S$ as functions of mesh size for a square lattice (Sq). Here, E and K are numerical results calculated from the strain-stress relationship under small deformations, while E_S and K_S are analytical values for LSM calculated from the expressions given in Chapter 2.2. The tension T is calculated based on the width of sheet after deformation. It is evident that the size of the

mesh influences the accuracy of the model. When the mesh is coarse, the spring network seems to overestimate the moduli since the hypothesis of a homogenous deformation of the individual lattice springs becomes inaccurate. As the mesh is refined, the values converge toward the analytical values for isotropic material. The deviation from the analytical value is less than 2% when grid size $\Delta x < 0.025$ for a unit length network sheet. The Poisson's ratio is found to be in good agreement with the analytical values.

Next, we compare the tension-strain relationships of a spring network with continuum models under large deformations. In all cases, we use a fine mesh to suppress the effect of mesh size. The tension-strain relationships are shown in Fig. 10b for several membrane models under uniaxial elongation. We note that SK law is strain hardening, while NH law is strain softening. When the strain is not very large ($\varepsilon < 0.6$), both square lattice and triangular lattice exhibit a linear tension-strain relationship, close to the Hooke's law with $\nu_S = 1/3$. For very large deformation, spring network shows slight strain hardening behavior. The isotropic tension-area dilation relations are shown in Fig. 10c. For a 2D sheet of square lattice, it shows a strain softening behavior close to NH law, which is similar to the result reported in [42].

We also study the behavior of a spherical capsule under uniform inflation. The sphere shell is composed of triangular lattices. Due to the discretization it is impossible to generate a fully isotropic mesh on a spherical surface. The most regular mesh that can be generated for a sphere is by subdivision of a regular icosahedron [66]. The subdivision scheme starts at creating a new node at the middle of each edge. Those new nodes are then projected onto the sphere surface and connected to form additional faces. This procedure can be repeated several times to create a finer gird.

In this study, the surface is discretized with 1280 triangles. In order to model inflation of a spherical capsule, we impose external forces uniformly distributed on the surface nodes with the direction normal to the surface. Following [42], we define the tension $T = R\sum_i \mathbf{F}_i \mathbf{n}_i \big/ 2S$, where R is the radius of the capsule after deformation, $\mathbf{n}_i$ is the outward normal unit vector to the surface at node *i*, and S is the total surface area. The tension-strain curve can be perfectly overlapped with the results of a 2D isotropic deformation with square lattice (Fig. 10c). Therefore, we can conclude that, for isotropic extension, previous findings on the mechanical properties of flat 2D spring networks can be applied to curved membranes.

After examining the behavior of LSM for the in-plane deformation, we probe the mechanical response of LSM under bending load. Specifically, a transverse loading test is performed using a clumped 2D spring sheet. For a long and relatively thin sheet, the effect of a force applied to the free end is sheet bending with negligible in-plane deformation. The results shown in Figure 10d are compared to the theoretical solution $y = \frac{Fx^2}{6EI}(3L - x)$, where F is the loading force at the free end, y is the deflection, L is the length of sheet, and $I = h^3 W / 12$ is the moment of inertia for a rectangular plate of thickness h and width W. Two types of spring network with two different bending models (bond-bending and dihedral angle) are compared with the theory. All models agree well with the theory within 5% error. We also find dihedral angle (DA) model has a more uniform deflection along the width of the sheet compared to bond-bending (BB) model.

3.6 Deformable Spherical Capsule in Shear Flow

The deformation of a single capsule freely suspended in linear shear flow has been studied extensively over the years. The results of the simulations allow us to relate the capsule deformation to the flow strength and to predict the stress level in the membrane [67].

We assume the external fluid and the fluid inside the capsule are Newtonian and share the same properties, including fluid density and viscosity. In the limit of a Stokes flow, the only dimensional parameter that characterizes the system is the capillary number $Ca = \dot{\gamma}\mu a / G_S$, which defines the ratio between viscous and elastic forces. Here, $\dot{\gamma}$ is the shear rate of the undisturbed external fluid, and a and G_S are the radius and the surface shear modulus of the capsule, respectively. Due to the presence of an external shear flow, the initially spherical capsule obtains an elongated shape with the long axis inclined with respect to the flow direction, while the membrane steadily rotates around the center of mass of the capsule. This tank-treading behavior has been observed by many researchers [68, 69]. The deformation of the capsule is typically quantified using the Taylor parameter D_{12} in the shear plane, $D_{12} = \frac{L - B}{L + B}$, where L and B denote the maximum and minimum profile diameters in the measurement plane, respectively.

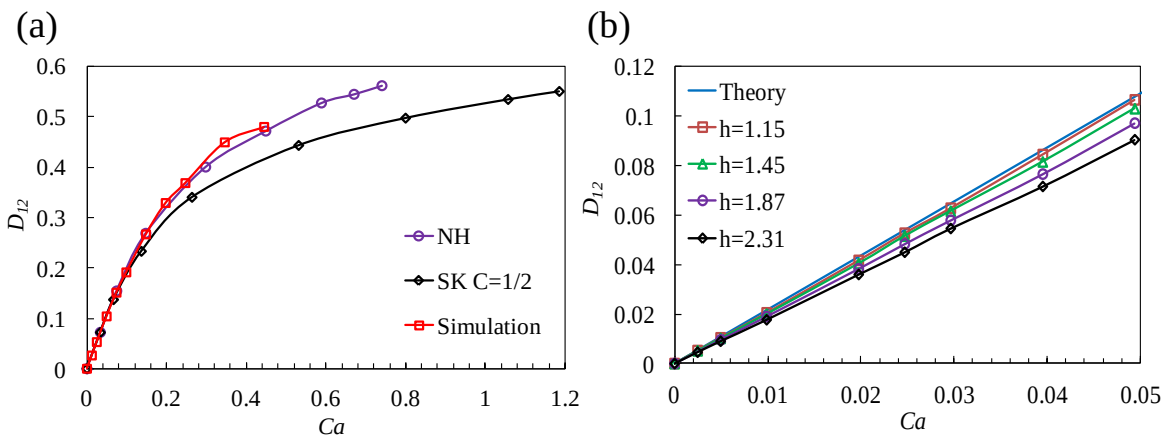

Figure 11 (a) Taylor deformation as a function of capillary number for capsules with NH, SK, and lattice spring model. (b) Taylor deformation in the shear plane as a function of capillary number for different bending rigidities. Theoretical data is from [69].

In a Stokes flow, the analytical expression for small deformations in the shear plane [69] is $D_{12} = \frac{5}{4}\left(\frac{2+\nu_S}{1+\nu_S}\right)Ca$, where ν_S is the Poisson's ratio of the membrane. This expression is valid for $Ca < 0.1$ and materials with zero bending rigidity. The asymptotic model predicts that compressive tension occurs in the vicinity of the equatorial plane. This means that the capsule is mechanically unstable and the membrane may buckle. Numerically, bending rigidity should be introduced into the membrane to prevent buckling. Furthermore, in practice, most physical membranes have a finite thickness and thus a resistance to bending.

In order to validate our numerical model, we compare our model with the theory for different values of bending rigidities with relatively small deformations. We use a large computational domain $15a \times 10a \times 10a$, where the capsule radius $a = 10$, which reduces the effect of the boundaries on the capsule deformation.

Figure 11(a) shows the Taylor parameter versus capillary number for a LSM capsule. The deformation of the capsule changes linearly with capillary number under small deformations. When the capsule is subject to a strong flow (large Ca), the deformation is similar to a neo-Hookean membrane capsule. The surface bending rigidity is defined as $D = \frac{E_S h^3}{12\left(1-\nu_S^2\right)}$, where E_S is the Young's modulus and h is the effect thickness of the membrane. Figure 11(b) shows the Taylor parameter as a function of Ca for capsules with different bending rigidities under small deformation. For a small bending rigidity, numerical results are close to the analytic solutions. Specifically, the relative errors are within 3%, 5%, 11%, and 17% for membranes with thickness 1.15, 1.45, 1.87, and 2.31 (LB unit), respectively. Higher bending rigidity makes the capsule stiffer, which agrees with the previously published results [68].

3.7 Summary

In this chapter, we validated our computational model for fluid-structure interactions that integrates the lattice Boltzmann and lattice spring models. The accuracy of the combined model is examined by comparing the simulation results with analytical and numerical solutions from the literature. The applicability of the model for simulation of fluid flows with particles is demonstrated.

CHAPTER 4

CONTINUOUS SORTING OF MICROPATICLES BY SIZE IN RIDGED MICROCHANNELS

4.1 Introduction

Separation of microscopic particles and capsules by size is a critical step in many medical assays and biochemical studies. Active methods for microparticle separation utilize forces from external sources such as dielectric, magnetic, acoustic forces or employ optical manipulation to discriminate particles and cells with different sizes [70-74]. These active methods typically provide excellent separation accuracy, but often offer limited throughput and require complex sample preparation and sophisticated external control.

Another approach is to use hydrodynamic effects in microfluidic channels, in which case individual particles are propelled by a flowing fluid and are separated due to interactions with channel microscale topography [75-80]. These interactions force particles with different properties follow different trajectories inside microchannel, thereby inducing their segregation. The passive hydrodynamic methods typically offer high-throughput and continuous separation critical for massive screening of biomedical samples. Furthermore, these methods can be often operated in an autonomous manner without any external control [70, 77, 81].

Among different methods for passive particle separation, microfluidic methods harnessing inertial hydrodynamic effects benefit from a simple device layout combined with the ability to operate at high flow rates, making this approach an attractive alternative for designing high-throughput microfluidic sorters [81]. This hydrodynamic

method is based on non-linear inertial effects in microfluidic channels that provoke cross-stream migration of solid particles. This inertial particle drift is associated with interplay of two hydrodynamic forces, namely a wall-induced lift force that repels particles away from the wall, and a force due to a non-uniform shear in channel flow that causes particles to migrate away from the channel centerline. A balance between these forces sets the particle equilibrium position in the flow, which depends not only on channel geometry [82] [83], but also particle size [81]. This size-dependence of cross-stream migration can be, therefore, employed for size-based particle separation. Specifically, small particles can be typically found at a distance about $0.2H$ from the wall in a channel with height H [11], whereas larger particles follow trajectories that are closer to the channel centerline. A practical disadvantage of this method is that the spatial separation between trajectories of different particles is relatively small and is comparable to particle size, thus making it difficult to identify and isolate particles with different sizes without extra processing steps.

In this chapter, we use simulations to design a ridged microfluidic channel that effectively sorts and separates neutrally-buoyant microparticles by size. The high-resolution particle separation is achieved using a combination of inertial migration effects and secondary flows induced by channel topography. More specifically, the top and bottom channel walls are decorated with symmetrically aligned diagonal ridges (Fig. 12a). The gap between opposite ridges is greater that the diameter of particles, thereby allowing their free passage between ridges and reducing the potential channel clogging. In our microfluidic system, inertial migration separates particles in the vertical z direction. This vertical separation is then amplified by secondary flows created by

periodical ridges that transport particles with different sizes to opposite channel sidewalls in the y directions. Thus, the combination of these two effects drastically enhances the separation efficiency and resolution. As we show below, this separation method is practically insensitive to the magnitude of fluid velocity and can be successfully employed with relatively high flow rates, which makes this approach especially attractive for high-throughput sorting and separation applications.

4.2 Computational Setup

In our three-dimensional simulations, we consider a pressure-driven flow in a periodic microfluidic channel of height H and width $W = 3.2H$ (Fig. 12a). The top and bottom channel walls are lined with symmetrical solid ridges. The rectangular ridges have the width $b = 0.4H$ and height $c = 0.2H$ and form a uniform gap between two oppositely laying ridges that is equal to $h = 0.6H$. Furthermore, the ridges are inclined at an angle $\alpha = 45^\circ$ relative to the channel longitudinal axis. In our current implementation, the channel is periodic in the x direction with a period equal to $L = 5H$; thus, the separation between centers of consecutive pairs of solid ridges is L. A constant pressure gradient is imposed in the negative x direction via a uniform body force to create a Poiseuille flow in the channel. We introduce neutrally-buoyant spherical particles with diameters a in the range between $a_{\min} = 0.1H$ and $a_{\max} = 0.5H$, and track their trajectories as the particles move through the ridged microchannel. We set the channel height equal to $H = 50$ LBM units. Hereafter, all dimensional values are given in the LBM units is not specified.

We impose non-penetration, no-slip conditions on the channel walls in the y and z directions and a periodic boundary condition in the x direction. Specifically, when a

particle leaves the channel at $x = L$, we introduce a new particle at $x = 0$ with the same y, z positions and the same exerting forces, thus we model the movement of particle through a periodic array of ridges in a microfluidic channel.

We characterize the microchannel flow in terms of the Reynolds number $\mathrm{Re} = U_m H/\nu$ that indicates the relative importance of inertial and viscous effects. Here, $U_m = \nabla_x P H^2/8\mu$ is the maximum flow velocity of the fluid with $\nabla_x P$ being the pressure gradient along the channel of a uniform height H. In the simulations described below, we vary Re between 0.5 and 20.

4.3 Results and Discussion

We start our simulations by placing particles with different diameters at $y = 0.5W$, and track the particle motion inside the ridged microchannel. We first fix the lateral y position of particles and let the particles to reach their equilibrium trajectories in the $z - x$ plane, and then release the particles so they can move in the y direction. This allows us to eliminate the effect of initial transient on the particle lateral migration.

Figures 1b and 1c shows the spatial trajectories of centers of mass of different particles after they are released at the same initial position $y = 0.5W$. Due to the periodical ridges, the trajectories oscillate as particles are propelled in the channel. More importantly, the trajectories of particles with different diameters are distinctly different. In the $x - y$ plane, smaller particles migrate in the positive y direction, whereas larger particles migrate in the negative y direction (Fig. 12b). Thus, different-sized particles almost uniformly spread out in the $x - y$ plane, thereby separating by size.

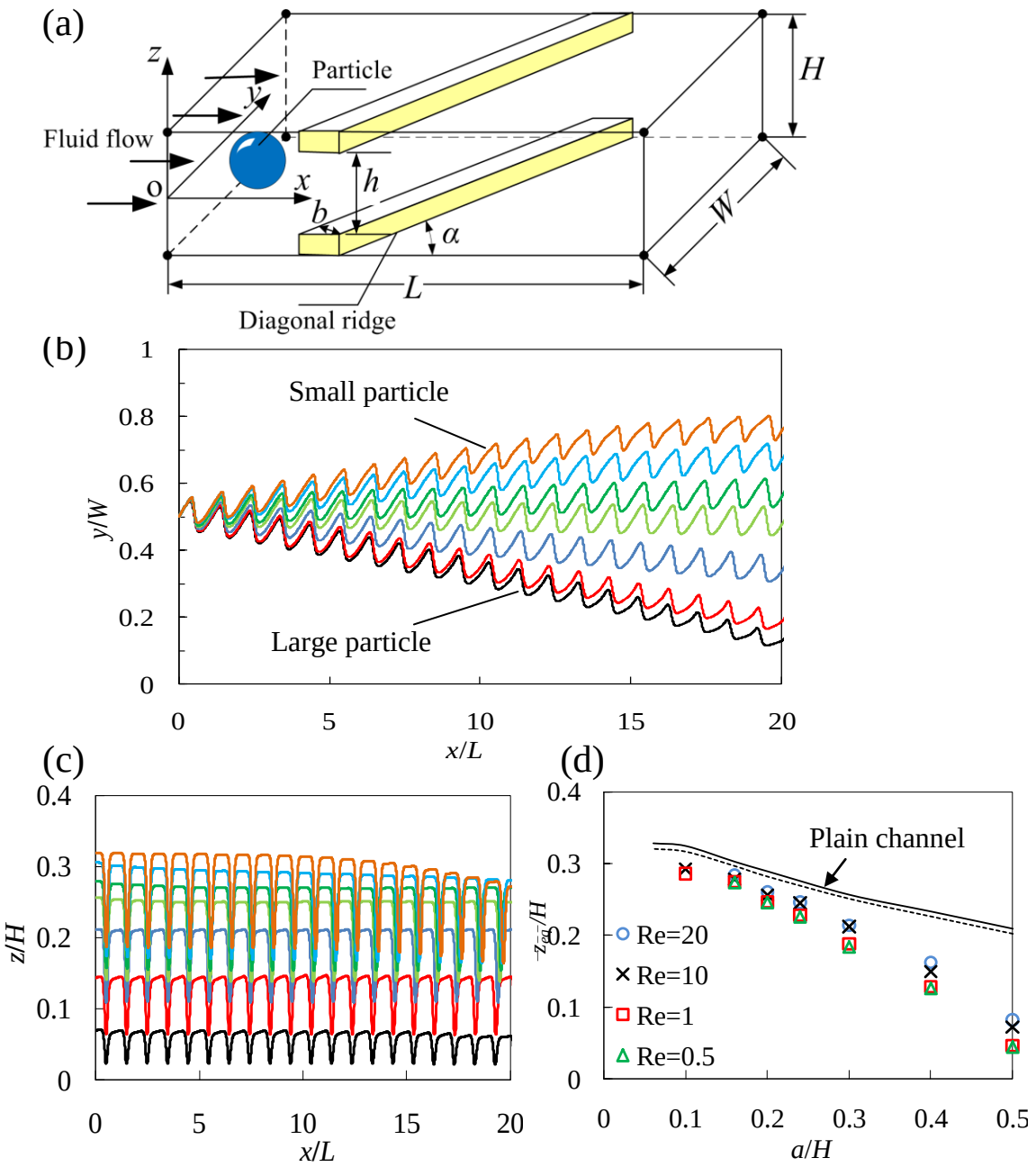

Figure 12 Panel (a) shows schematic of a microfluidic channel with diagonal ridges protruding from the top and bottom walls. Trajectories of particles with different sizes in (b) $x-y$ plane and (c) $y-z$ plane. In panels (b) and (c), $\mathrm{Re}=10$ and the lines from the top down respectively correspond to particles with sizes: $a/H=0.1$, 0.16, 0.24, 0.3, 0.4, and 0.5. Panel (d) presents equilibrium positions of different sized particles in pressure driven channel flows with different Re. The symbols indicate equilibrium positions in ridged channels, whereas the dotted and solid lines show the particle equilibrium positions in channels with smooth walls with $\mathrm{Re}=1$ and $\mathrm{Re}=10$, respectively.

This separation process is rather fast. After about 20 channel periods the smallest and the largest particles migrate to the opposite channel sidewalls, making it easy to differentiate and isolate these particles. We note that the separation can be further enhanced by including additional ridges and increasing the channel width. Thus, a microchannel with diagonal ridges constitutes an effective means for rapid sorting and separation of solid particles by size.

We first study the transient process during which particles drift from the initial vertical position to a new equilibrium trajectory in the $z-x$ plane. Figure 13 shows the focusing of particles with the same diameters ($a=20$), but different initial positions. We find that the particles have three possible equilibrium trajectories. One is at the channel center due to the symmetry, but this equilibrium trajectory is unstable and any small perturbations end up in particles migrating to other equilibrium trajectories.

The two other equilibrium trajectories are symmetric with respect to the channel height. When the initial position of a particle is close to the wall, it can rapidly reach the equilibrium trajectory after only one period of the ridges (the blue line in Fig. 13). This indicates that wall repulsive force pushes particles to the channel center. On the other hand when the initial position of particle is close to the centerline, it may take several periods for the particles drift to an equilibrium trajectory. In this case the drift is due to a shear-induced lift force.

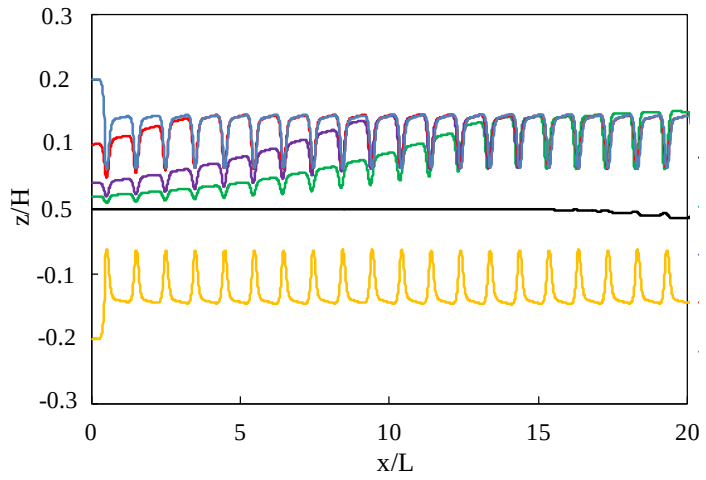

Figure 13 Focusing of particles with different initial positions in the x-z plane.

The magnitude of the lift force in a parabolic flow between two infinite planes is given by $F_L = f_L(\mathrm{Re}, z/H)\rho U_m^2 a^4 / H^2$ [14]. Here, f_L is a nondimensional lift coefficient that depends on the position of the particle in the flow and the channel Reynolds number. At equilibrium, where all forces on the particle are balanced, $f_L = 0$. The expression for the inertial migration velocity, U_L, can be developed assuming that the lift force is balanced by the Stokes drag, i.e. $F_L = 3\pi\mu a U_L$, yielding $U_L = f_L \rho U_m^2 a^3 / 3\pi\mu H^2$.

To estimate of the migration time, we assume the average value of $f_L = 0.025 H/a$ for the particle migration from the center to the equilibrium position [81]. In this case, the number of microchannel structure periods required to migrate to the equilibrium trajectory is $p = \dfrac{\Delta z / U_L}{L/U_m} = \dfrac{3\pi\mu H^2 \Delta z}{f_L \rho U_m a^3 L}$, where Δz is the migration distance. Table 1 compares the migration periods from our simulations and the estimates for particles with different sizes. Although our estimates are rather rough, the theoretical

results are relatively close to the simulations. We find that the migration velocity is small compared to the mainstream velocity ($U_m \approx 0.017$ LB unit). However, if the particles are not far away from the equilibrium position, migration periods typically are less than 20 due to the confined channel height.

Table 1 Comparison of migration periods from simulation and calculation at $\mathrm{Re} = 5$.

Particle diameter (d, LB unit**)**	**Migration distance (** $\Delta z / d$ **)**	**Migration velocity (** U_L / U_m **)**	**Migration periods (simulation)**	**Migration periods (calculation)**
20	0.115	3.05e-3	4	3.6
20	0.265	3.05e-3	10	8.3
20	0.315	3.05e-3	14	9.9
15	0.367	1.72e-3	11	15.3
15	0.567	1.72e-3	21	23.7
10	0.35	0.76e-3	19	22.0
10	0.85	0.76e-3	39	53.4

Different-sized particles also exhibit distinct trajectories in the $x-z$ plane (Fig. 12c). In this case, however, the separation between trajectories of different particles is relatively small and remains roughly the same as particles are propelled along the microchannel. The only exception is for particles that are close to the side wall, their equilibrium trajectories change as they approach the side wall.

The separation of particles with different sizes in the $x-z$ plane is related to the particle inertial drift in a pressure-driven channel flow which alters particle z position [77, 84]. In Figure 10d, we show the particle positions at equilibrium, z_{eq}, as a function of particle diameter. To calculate these equilibrium positions, we average the z component of particle trajectories. We find that larger particles have z_{eq} closer to the channel centerline at $z = 0$, whereas smaller particles drift closer towards the channel walls. Similar results are found for smooth channels without ridges (shown in Fig. 12d by

the solid and dotted lines). This size dependent equilibrium positions was experimentally observed by Di Carlo *et al*. [81]. In plain channels, however, the separation between the smallest and largest particles is less than a half of the separation in ridged channels. We also find, for the channel with normal ridges, the equilibrium positions are almost the same as slanted ridges. Thus, periodical ridges enhance the size-dependence of particle drift in the $x-z$ plane by displacing larger particles closer to the channel centerline.

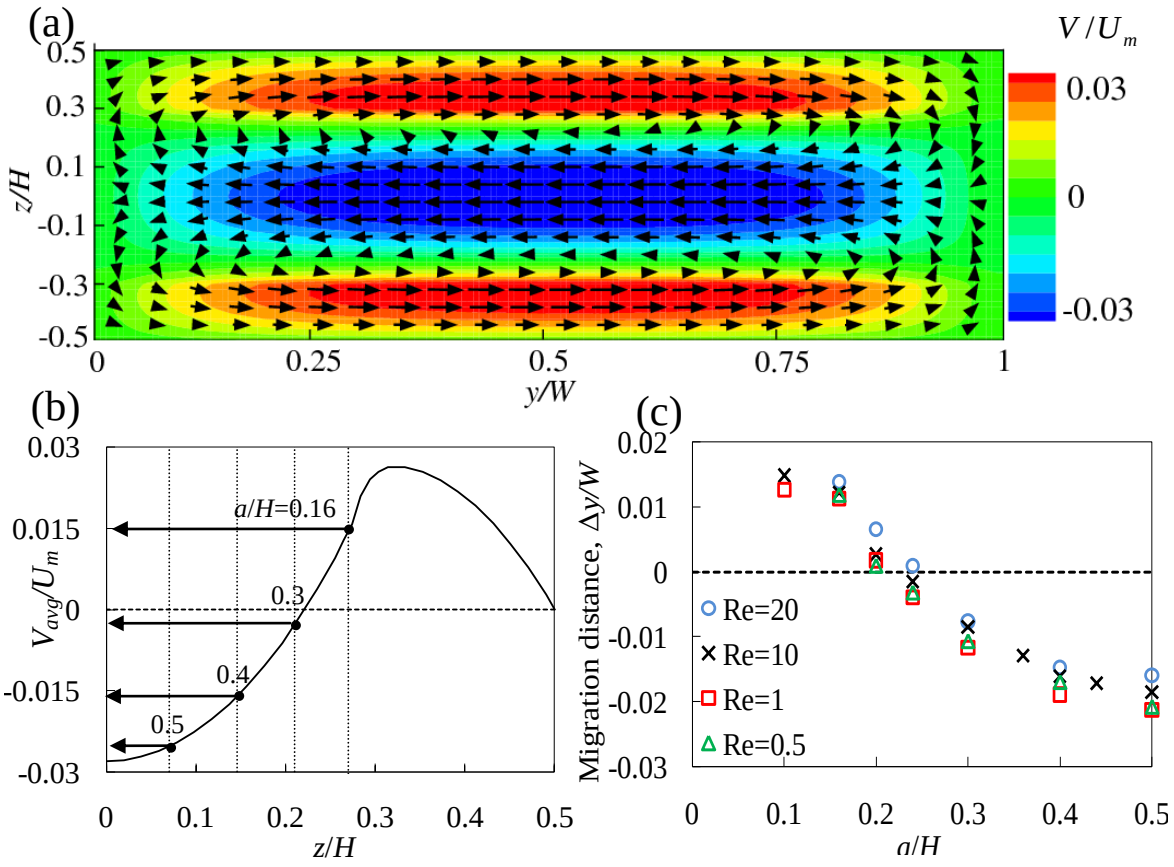

Figure 14 Panel (a) shows cross-stream velocity distribution in a channel with ridged walls. The velocity is averaged over one period of the wall structure. The arrows show the direction of fluid velocity, whereas the color represents the normalized magnitude of lateral fluid velocity. Note that the diagonal ridges create circulatory flows that transport fluid to the left in the channel midplane and to the right close to the top and bottom walls. Panel (b) shows averaged lateral flow velocity as a function of vertical position inside channel. Here, the vertical dotted lines show equilibrium position of particles with different sizes and the arrows indicating corresponding particle cross-stream drift velocities. Panel (c) shows the migration distance per channel period as a function of

particle size for different Reynolds numbers. Note that while the flow rate is changed 40 times between $\mathrm{Re} = 0.5$ and $\mathrm{Re} = 20$, the migration rate per ridge changes by only a few percent.

The diagonal ridges not only enhance the particle size separation in the $x-z$ plane (Fig. 12c), but also induce particle spreading in the $x-y$ plane (Fig. 12b). To explain the $x-y$ separation, we calculate the average velocity field in the $y-z$ plane in microchannel. Figure 14a shows that diagonal ridges create two vortices, in which the fluid at the channel center ($z=0$) is transported in the negative y direction, whereas the fluid located near channel walls ($z=\pm H/2$) moves in the positive y direction. This effect is harnessed to create the y separation among particles with different z positions.

Figure 14b shows the average fluid velocity V_{avg} in the y direction and the equilibrium positions of different sized particles z_{eq}. For larger particles, the velocity is negative and, thus, these particles migrate towards the wall at $y=0$. On the other hand, for smaller particles, the velocity is positive and these particles move towards the wall at $y=W$. Between z_{eq} of the smallest and largest particles, the fluid velocity V_{avr} monotonically changes, thereby enabling almost uniform spreading of different sized particles. We note that the magnitude of lateral migration velocity is at least 10 times faster than the vertical migration velocity (Table 1), which indicates the secondary flow in lateral direction significantly enhances the particle separation.

We summarize our simulations in Fig. 14c, where we plot the y displacement of particles over one channel period, Δy, as a function of particle diameter a. This plot can be used to determine size of particles based on their trajectories, whereas the final separation resolution is defined by the channel width.

To further investigate the influence of flow velocity on particle separation, we calculated the displacement in flows with different Re and found that Δy is almost independent of flow rate (Fig. 14c). Indeed, particle equilibrium position z_{eq} practically does not change with Re (see Fig. 12d), whereas the circulation flow velocity is linearly proportional to the mean fluid velocity. Thus, the separation method is insensitive to channel flow rate for a wide range of Re, which is important for the robust operation of high-throughput devices. Based on our simulations for $\mathrm{Re} = 20$, we estimate that a ridged microchannel of 1 mm length can separate up to 10^5 particles per minute and the separation rate can further enhanced using channel parallelization.

4.4 Summary

In summary, we use computer modeling to design a ridged microchannel that hydrodynamically separate solid spherical particles by size. This new continuous separation method is insensitive to the variations in fluid flow rate, features high throughput, enhanced resolution, and simple channel layout, enabling simple integration in lab-on-a-chip devices for autonomous particle sorting. Furthermore, we expect this method can be adapted with minimal changes for stiffness-based separation of biological cells and compliant particles, in which case the equilibrium trajectories in the channel flow are defined by particle mechanical stiffness.

CHAPTER 5

STIFFNESS DEPENDENT SEPARATION OF CELLS IN A MICROFLUIDIC DEVICE

5.1 Introduction

Rapidly sorting and separating biological cells can enable a large number of applications in bio-related science and technology. For example, diseased cells have been identified through morphological differences with healthy cells and fluorescent molecular markers are routinely used to separate specific subpopulations of cells [85, 86]. However, the morphological overlap between the diseased and healthy cells often poses a significant problem to accurate identification of cell populations. New molecular and biophysical markers which can be detected and used to rapidly sort cells are critical to robust separation of specific cell subpopulations.

A variety of different mechanisms utilizing microfabricated structures have been used to separate biological cells, including magnetic fields [72, 87, 88], electric fields [89-92], optical forces [93, 94], and acoustic fields [71, 95, 96]. However, these active separation methods generally require an applied external field which adds to the complexity and increases the cost. Alternatively, labeling of cells through specific binding of fluorescent antibodies [97] is expensive and hampers the downstream analysis of separated cells. Additionally, the separation executed by these techniques occurs only after individual readout of the labeling differentiation. This process may be slow, leading to limited throughput.

Consequently, a label-free method that can separate cells continuously by biophysical properties would greatly complement existing separation technologies. A

number of disease states result in drastic changes in cell mechanics in comparison with healthy counterparts. For example, several studies have shown a reduction in cell stiffness in human cancer cells [98, 99]. Mechanical stiffness has been utilized to identify abnormal cell populations in detecting cancers [100-103] and infectious diseases [98, 102]. Recently, mechanical stiffness of cells was used to classify and enrich cell populations [104-106].

One of the limitation of the current methods of high throughput biophysical detection and separation is a coupling between cell size and stiffness [106, 107] or optical refractive index and stiffness [99]. This coupling affects the effectiveness of stiffness-based separation due to the heterogeneity within cell populations. In this chapter, we demonstrate a new strategy to passively, continuously, and non-destructively separate cells into subpopulations by exploiting the variation in mechanical stiffness between individual cells using a fluid flow in a structured microfluidic channel.

5.2 Computational Setup

We use three-dimensional computational simulations to design microfluidic channels for continuous flow separation of deformable cells. The microfluidic channel is decorated with an array of diagonal ridges protruding from the top wall (Fig. 15a). The dimensions of our simulation box are: length L = 5.2D, width W = 12.5D, height H = 1.33D, where D is the diameter of the cell. The solid ridge has width 1.33D and is inclined to an angle $\alpha = 45^{\circ}$ relative to the channel axis. The gap between the ridge and channel bottom wall h is equal to 0.57D.

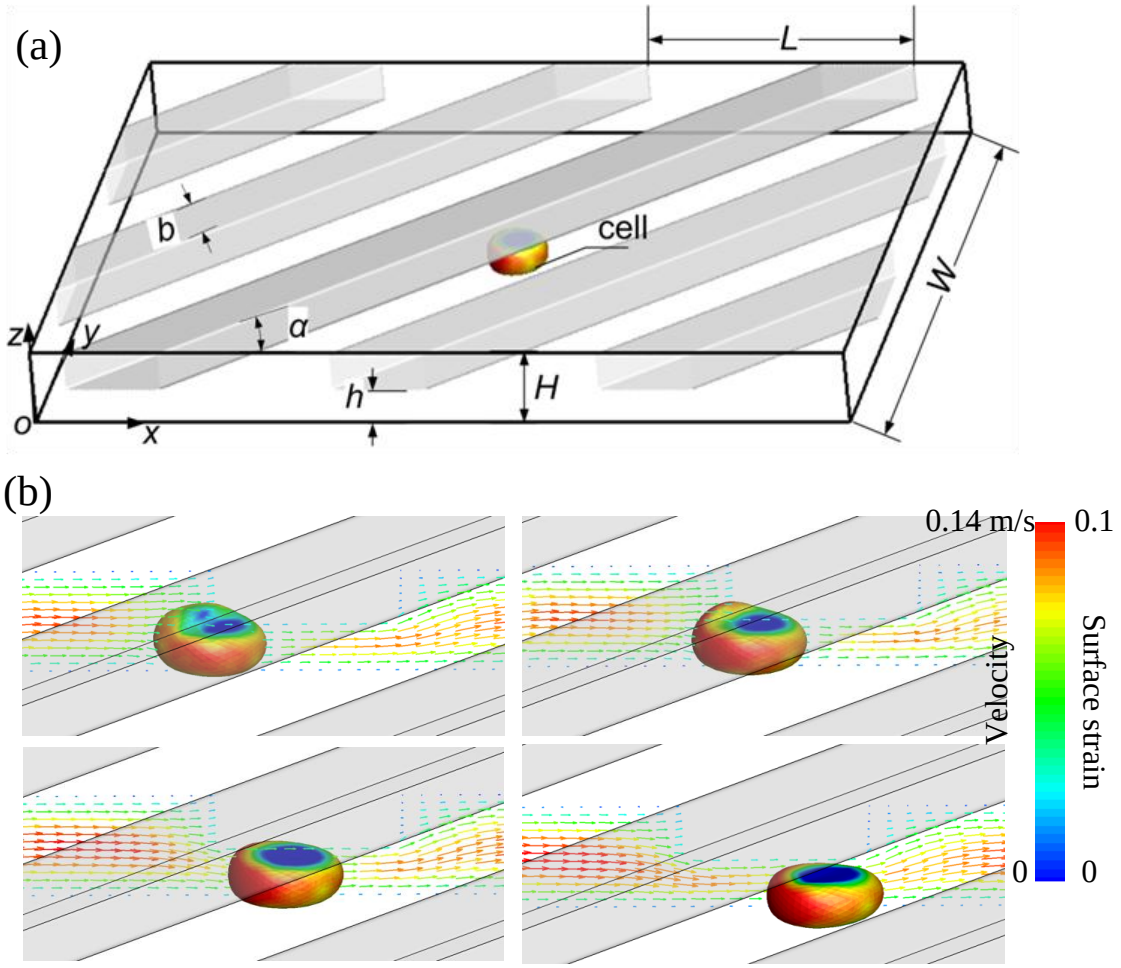

Figure 15 (a) Schematic of the microfluidic device. The ridge is inclined at angle $\alpha = 45^{\circ}$ and the ridge width $b = 20\ \mu m$. The spacing L of ridge period is $78.3\ \mu m$. The gap h between the ridges and the substrate is $8.5\ \mu m$. (b) Snapshots present the dynamics of a cell when passing through the ridges. Arrows show the velocity field in $x-z$ plane. The color bar shows surface strain of the cell.

A pressure gradient in the x direction is imposed via a uniform body force. We apply non-penetration, no-slip conditions for the walls in the y and z directions and a periodic boundary condition in the x direction. Thus, we effectively model the motion of cells in a channel with a periodic array of diagonal ridges. We characterize the flow in terms of the Reynolds number $\mathrm{Re} = \rho U_0 H / \mu$ that represents the relative importance of inertial and viscous effects. Here, ρ is fluid density, μ is fluid viscosity, and

$U_0 = \nabla_x PH^2/12\mu$ is the average fluid velocity in a straight channel of height H due to the pressure gradient $\nabla_x P$. The Reynolds number is set to be equal to 1.33. We characterize the relative importance of viscous forces versus the elastic response of cell by defining a dimensionless cell capillary number $Ca = \mu U_0/ED$, where E is cell Young's modulus.

5.3 Cell Model

We choose lymphoblastic cell line K562 (CCL-243) as the prototype. These non-adherent cells appear to be spherical with an average diameter of approximately 15 μm. The cell is modeled as a spherical fluid-filled elastic shell. The shell is formed from a layer of 642 equally spaced LSM nodes connected by stretching and bending springs. The spring constants are tuned such that cell deformation matches the atomic force microscope (AFM) experiments conducted by our collaborators. The cytoplasm is characterized by a high viscosity [108]. To mimic this viscoelastic property, we set the viscosity of the fluid encapsulated in cell $\mu_{in} = 10^3 \mu$.

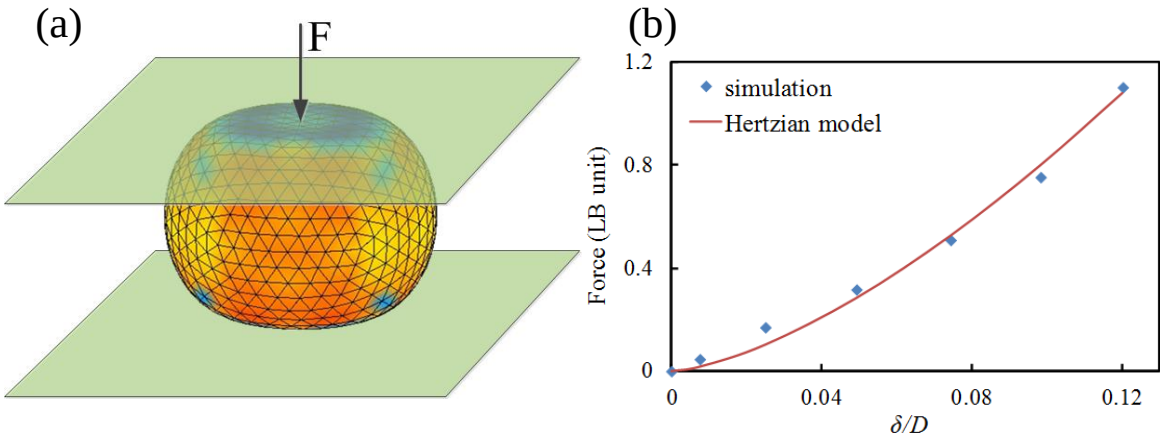

Figure 16 (a) Schematic view of the cell compression between two plates. (b) Force versus dimensionless indentation curve derived from a cell, fitted with the Hertzian model.

To establish the mechanical properties of the model cells we conduct indentation simulations mimicking AFM experiments. In the indentation simulation, cells are compressed between two parallel plates (Fig. 16a). The force-indentation curve is obtained in the simulation and then Hertzian model is used to fit the curve to calculate the apparent Young's modulus. The Hertzian model has been shown to be valid for small deformations of biological cells (up to 10% of the cell diameter) [109].

When the spherical cell is subjected to an applied normal force F between two rigid flat walls, the Hertzian model gives the following relation for compressed cell $F = \frac{4\sqrt{R}}{3}\frac{E}{1-\nu^2}\delta^{3/2}$. Here, δ is the indentation, i.e. a half of the compressive displacement at the pole of the deformed cell, ν is the Poisson's ratio (for soft biological samples, it is assumed to be 0.5), E is apparent Young's modulus, and R is the radius of the cell. Figure 16b shows the force-indentation dependence obtained in our simulations and the fitted curve corresponding to the Hertzian model. The simulation results are close to the Hertzian model, which indicates that our cell model yields a static mechanical response similar to that of biological cells.

5.4 Results and Discussion

We start our simulations by placing cells at the middle of the microchannel ($y = 0.5W$) and letting them to reach their equilibrium trajectories in the vertical direction. Then, we release the cells so they can move freely in the lateral direction. This allows us to eliminate the effect of initial transients on the cell lateral migration. Snapshots in Figure 15b show how the cells dynamically deformed by the solid ridges. The initially spherical cell is compressed when it passes through the first ridge and

remains, due to slow relaxation, in this compressed state when moves in the rigid channel.

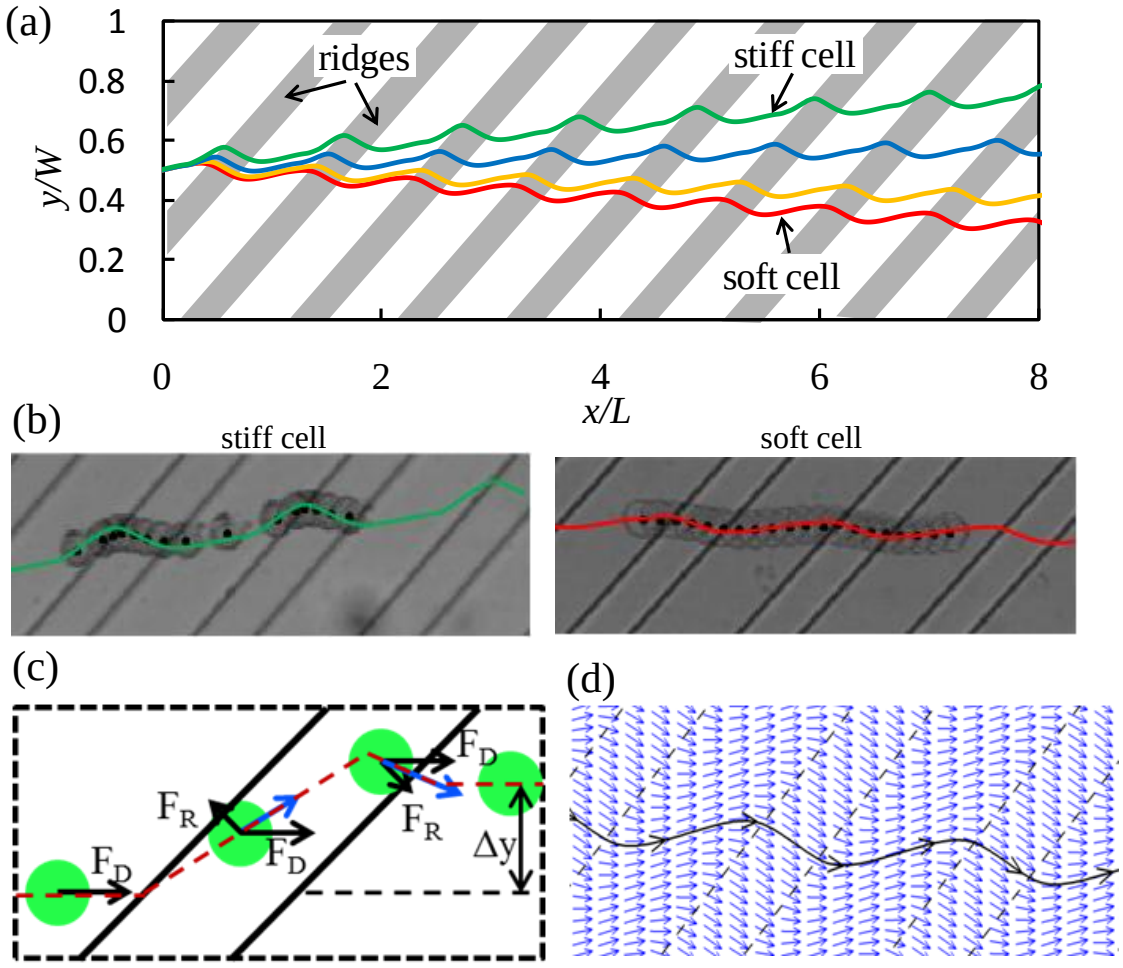

Figure 17 (a) Simulation results show trajectories of cells of different stiffness in the channel. The lines from the top down respectively correspond to cells with capillary numbers: *Ca* = 2.1e-3, 2.6e-3, 3.9e-3, and 5e-3. Gray straps indicate the ridges. (b) Overlaid of still frames from experiment and simulation shows cell trajectories. The black dots represent the center of cells. The solid line presents the corresponding simulation result. (c) Schematic of the cell's trajectory across a diagonal ridge. (d) Top view of velocity field and streamline in the channel.

Figure 17a shows the simulated spatial trajectories of cells with different stiffness. The simulation shows that dissimilar cells exhibit diverging trajectories. We find that stiffer cells move in the positive y direction, whereas softer cells migrate in the negative y

direction, thereby separating by stiffness. The experimental trajectories with cells with corresponding stiffnesses are shown in Fig. 17b with the results from the simulations overlaid.

The experimental and simulated trajectories are in good agreement indicating the simulation accurately captures the trajectory oscillations due to the periodical ridges and the distinct paths due to different stiffnesses. The lateral migration rate is almost uniform across the channel, which provides constant lateral displacement per ridge and steady separation. When cells move in the narrow gap between a ridge and the top wall, they display a disc-like shape (see Fig. 15b). We find that due to a large internal viscosity cells do not fully recover to their undeformed shapes when propelled in the wider sections of channel between consecutive ridges, but remain squashed.

Cells propelled by fluid flow experience mechanical forces when they confront periodic ridges in microchannel (indicated by F_R in Fig. 17c). These forces arise due to cell deformation and, therefore, are proportional to the cell mechanical stiffness. Thus, cells with different stiffness experience different mechanical forces when they pass through periodical constrictions. Thermodynamically, this mechanical force is associated with the change of system free energy due to cell elastic deformation and, therefore, is directed normal to the ridge. At the same time, drag force from the fluid propels the cell forward (indicated by F_D in Fig. 17c). Thus, the total force has a component that drives cells along the ridge before it goes through. Cells with larger stiffness result in a larger force, leading to greater transversal displacement in the positive y direction (Fig. 17b). On the other hand, when cells are soft, the mechanical force is weak and cells move with fluid streamlines. Diagonal ridges alter fluid flow direction (Fig. 17d) [110, 111] and,

consequently, softer cells are more propelled by the flow, in the negative y direction (Fig. 17a).

We find that the lateral migration per ridge is determined by the intrinsic cell stiffness and the channel flow rate, both of which can be described in terms of the dimensionless capillary number. Figure 18a shows cell lateral migration per ridge as a function of capillary number. We find that the threshold capillary number Ca_c (where the lateral migration is zero) remains unchanged with different flow rates. This indicates that the magnitude of threshold particle stiffness can be tuned by changing the flow rate. This enables our device suitable to separate different types of cells with different mechanical properties by simply changing the flow rate without changing any geometric dimensions of the channel. The relatively soft cells with $Ca > Ca_c$ migrate negatively in transverse direction, whereas stiffer cells with $Ca < Ca_c$ migrate positively in transverse direction. As a result, soft and stiff cells accumulate on the opposite sides of the microchannel.

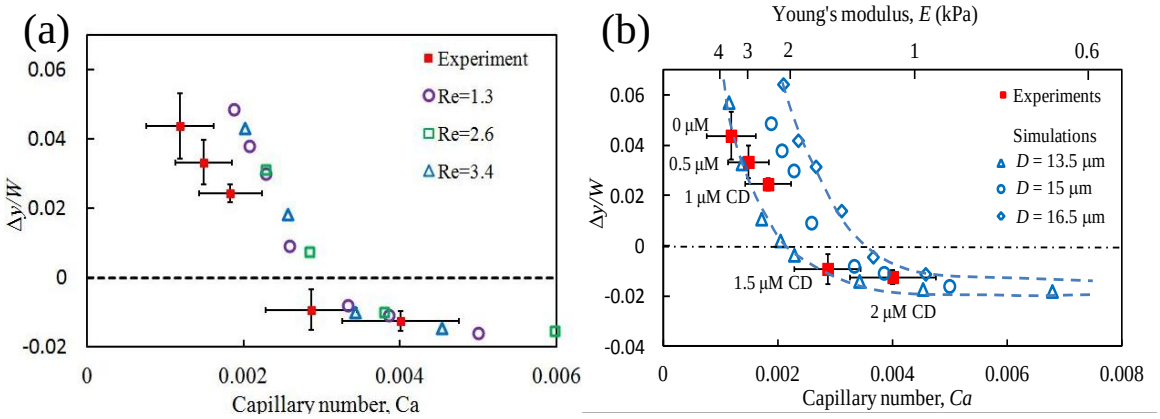

Figure 18 (a) Normalized transverse displacement per ridge as a function of capillary number with different Re numbers. (b) Normalized transverse displacement per ridge as a function of capillary number (bottom x axis) and Young's modulus (top x axis). The red solid squares with error bars represent the experimental results. The hollow symbols show the simulation results for different cell diameters. The blue dashed lines are guides for the eye.

Experimental results show that cell size is not a significant factor in cell separation for the conditions tested. We hypothesize that the lack of sensitivity to cell size in the separation is due to the cell's viscoelasticity. The mechanical compression imposed by the ridges is periodic, with a time between ridges (approximately $0.75\,ms$) much shorter than the time for relaxation of the cells. Viscoelasticity of leukocytes and K562 cell line was previously studied by micropipette aspiration [112, 113] and the characteristic time scale for cell relaxation was found about 0.1 seconds. Therefore, the individual cells will likely not have sufficient time to fully relax to equilibrium diameter before they are compressed by the next ridge. This behavior is also is found in our numerical simulations.

Since the mechanical force on the cells due to narrow constrictions is mostly defined by the size of deformed cell normal to the constriction, initial cell size does not significantly affect the transverse separation. This weak sensitivity of separation to cell size allows eliminating pre-processing size separation which may be required by other methods for high-throughput hydrodynamic separation by stiffness [106]. Our simulations show that cell size has a relatively small effect on lateral migration (Fig. 18b) and the range is mainly within the experimental error. Additionally, cell deformation and dynamics can be affected by viscoelastic responses of biological cells, which have not been included in our computational mode. These effects can be especially important when cells undergo large periodic deformations. Viscoelastic behavior of cell under large deformations should be considered in the further research.

5.5 Summary

We demonstrate a new approach to continuously separate cells by their differential stiffness. This deformability-based microfluidic separation platform may be valuable for separating and identifying diseased cells from healthy cells, as a variety of cell pathologies manifest through a change in mechanical stiffness in cells. Furthermore, this platform can be applied in high-throughput cell stiffness measurements.

CHAPTER 6

FLUID AND PARTICLE INERTIA EFFECTS ON THE MOTION OF SPHEROID PARTICLES IN SHEAR FLOW

6.1 Introduction

Hydrodynamic interaction of a non-spherical particle leads to a dynamic orientation of the particle in the flow. In 1922, Jeffery [114] demonstrated that an isolated inertialess ellipsoid in an unbounded zero-Reynolds-number linear shear flow follows one of a family of closed orbits (usually called Jeffery orbits) around the vorticity axis. There is an infinite number of such orbits, and the specific orbit that particle follows depends on the initial particle orientation. The orbit period of an spheroid with an aspect ratio $a_r = a/b$ (defined as the semi-axis length a divided by the semi-axis length b) is given by $T_J = 2\pi(a_r + a_r^{-1})/\gamma$, where γ is the shear rate.

A schematic diagram of a spheroid rotating in a simple shear flow is depicted in Figure 19. The orientation of the spheroid can be defined by a unit vector $\mathbf{p}$. In order to compare particle trajectory with a Jeffery's orbit, we also define θ as the angle between $\mathbf{p}$ and the vorticity (z) axis, and φ as the angle between the projection of $\mathbf{p}$ on the shear ($x-y$) plane and the x axis. Thus, $p_x = \sin\theta\cos\varphi$, $p_y = \sin\theta\sin\varphi$, and $p_z = \cos\theta$. The solution of the Jeffery equation is $\tan\varphi = a_r \tan(2\pi t/T_J + \varphi_0)$ and $\tan\theta = Ca_r \Big/ \sqrt{a_r^2 \sin^2\varphi + \cos^2\varphi}$, where t is time and the phase shift φ_0 is determined by the initial conditions. The values of an orbit constant C range from 0 to ∞, corresponding to the orientations $\theta = 0$ and $\theta = \pi/2$, respectively.

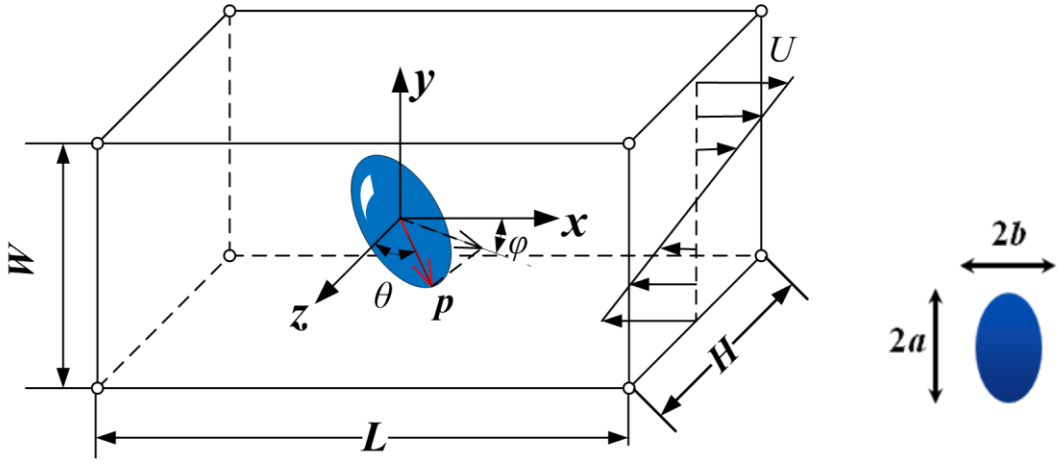

Figure 19 Schematic diagram of a spheroid particle rotating in a simple shear flow.

Jeffery's theory has been experimentally verified [115, 116], but some experiments also found that particles did not move in a closed orbit, but showed a slow drift to a preferred orbit [117]. Bretherton [118] found that the orbit would be closed for almost any body of revolution within the context of the Stokes equations suggesting that the drift to a preferential orbit may be explained by inertia or non-Newtonian effects. In these early works, both the particle inertia and the fluid inertia were neglected. Leal [119] examined the dynamics of inertialess particles in a fluid flow with inertia. Still open questions were, however, how a combination of fluid inertia and particle rotary inertia affects the motion of spheroids and what parameters characterize this behavior.

More recently, it has been shown that at a finite Reynolds number, neutrally buoyant elongated particles (prolate spheroids) tend to drift to an orbit where they rotate in the shear plane [120]. Subramanian & Koch [121] examined the dynamics of a slender fiber in a simple shear flow. They concluded that at a critical *Re* the fiber stops rotating and obtains a final stationary orientation in the shear plane. This result was confirmed by

Ding & Aidun [122] who also found that the period of rotation increases to infinity at a critical *Re* for elliptical cylinders and oblate spheroids in a simple shear flow.

Feng & Joseph [123] numerically investigated the rotation of an ellipsoid in a simple shear flow. Solid inertia and unsteady inertia of the fluid (the Basset force) were taken into account even in the limit of a creeping flow. They found that the unsteady inertia of fluid can change the characteristics of the particle motion in creeping flows. Broday et al. [124] examined the motion of spheroids in a vertical shear flow, with emphasis on the combined effect of particle inertia, flow velocity gradient, and the gravity on particle migration across streamlines. They found that inertial particles migrate across streamlines and the rate of drift depends on particle shape.

Yu et al. [125] studied the rotation of a neutrally buoyant spheroid in a simple shear flow. They found that fluid inertia can significantly affect the orbits of spheroids. For a prolate spheroid, particle undergoes Jeffery orbit, tumbling, quasi-Jeffery orbit, log rolling, and inclined rolling with increasing Reynolds number, whereas an oblate spheroid undergoes Jeffery orbit, log rolling, inclined rolling, and a motionless state. It was shown that the orbit behavior is sensitive to the initial orientation in the case of strong inertia.

Altenbach et al. [126] investigated the effect of particle inertia on the rotary motion of a fiber in a uniform creeping flow. They found that the principal effect associated with the particle inertia is a slow drift of the rotating fiber towards the flow plane. Lundell & Carlsson [127] found a similar behavior for heavy ellipsoids. They defined the Stokes number $St = 4\rho_s \dot{\gamma} a^2 / \mu$, where ρ_s is the density of the particle and a is the length of the semi major axis of the ellipsoid. For small St, particle motion is

similar to Jeffery obits with the addition of an orbit drift to the flow plane. At larger St, for particles oriented in the flow plane, the rotation rate increases abruptly to half of the shear rate, while for particles with other orientations, the motion goes from a kayaking motion to the rotation around an oblique axis.

Rotation of spheroids has been studied with a wide variety of experimental and numerical methods. Most of these studies either examined inertialess particles or the conditions in which fluid inertia has a negligible effect. Only a few studies probed the simultaneous effect of both particle and fluid inertia on spheroid dynamics. However, even these are limited to particular cases of neutrally buoyant particles [125], constrained to rotation in the shear plane [122], and elliptical cylinders in a two-dimensional shear flow [122, 128]. A comprehensive understanding of the effect of fluid and particle inertia on the orientation and rotation of particles with different aspect ratios is yet to be established.

Several studies have also examined the effect of confinement on non-spherical particle trajectories. Ku & Lin [129] examined the effect of channel confinement ratio on the rotational motion of a two-dimensional fiber in a simple shear flow. They found when the confinement ratio is larger than 3, it has no effect on the motion. They also found that when Re increases beyond a critical value, periodic rotation stops. This critical Reynolds number increases with decreasing confinement ratio.

Our review indicates that the dynamics of spheroid particles in a microfluidic environment is a complex process that still remains poorly explored. To get a better insight into the dynamics, there is a critical need for comprehensive computational models capable of simultaneously capturing the effects of fluid and particle inertia, as

well as the effect of bounding walls. These models can not only help us better understand the dynamics of spheroid particles, but also can be applied to design new microfluidic methods for the separation and focusing of non-spherical particles [130].

6.2 Computational Setup

In our study, the computational domain is a box of sizes $L \times W \times H$. Two boundaries located at $y = 0$ and $y = W$ move in opposite directions with a constant speed U as shown in Figure 19. The particle Reynolds number is defined as $\mathrm{Re} = 4\rho_l a^2 \gamma / \mu$ for a prolate spheroid and $\mathrm{Re} = 4\rho_l b^2 \gamma / \mu$ for an oblate spheroid, where ρ_l is the fluid density, μ is the fluid viscosity, and $\gamma = 2U/W$ is the shear rate. To characterize the effect of particle inertia, we define the Stokes number as $St = \mathrm{Re}\, \rho_s / \rho_l$, where ρ_s is the density of the solid particle.

In order to model an unbounded shear flow, we employ the Edwards-Lee boundary condition [131] at the upper and lower boundaries of the computational domain. This boundary condition allows us to reduce the wall effect in the shear gradient direction due to a finite size of the computational domain. Periodic boundary conditions are applied in other two directions. We set $L = 20d$ and $H = 12d$ which ensures that the periodic domain boundaries do not affect the simulations. Here, d is the length of the semi-major axis (i.e. $d = a$ for a prolate spheroid and $d = b$ for an oblate spheroid). We validated that our results are not sensitive to the domain size by performing simulations with an increased domain size. Combining a large domain size with the Edwards-Lee boundary conditions used at the shear walls makes our method applicable for studying particle motion in an unbounded shear flow.

To separate the effects of particle inertia and fluid inertia in our simulations, we conduct simulations with and without fluid inertia. To exclude the effect of fluid inertia, we modify the standard LBM by removing the quadratic term from the particle equilibrium distribution [24]. With this modification, LBM reproduces the hydrodynamics governed by the Stokes equation.

In all our simulations, a simple shear flow is used as the initial velocity distribution. The particle is released at the center of the computational domain with zero velocity. Although the translational motion of the particle is not constrained, the center of the spheroid is found to remain at the initial position.

To validate our model, we compared our simulation results for a neutrally buoyant oblate spheroid rotating in a shear flow with the results of a previously reported numerical model [18]. In our validation study, the domain size is set to $200\times80\times40$, and the semi-axes of the particle are 8, 16, 16 (LBM unit), which are identical to the parameters used in [18]. The initial orientation of the particle is $(\theta_0, \varphi_0) = (\pi/2, 0)$, i.e., the symmetry axis is parallel to the flow direction.

The results of the validation study are depicted in Figure 20. Figure 20a shows that the periods of tumbling at $\mathrm{Re} = 50$ and $\mathrm{Re} = 70$ are much longer than the Jeffery's solution ($a_r = 0.5$, $T_J\gamma = 15.708$) and the rotation stops when $\mathrm{Re} = 90$. The tumbling period as a function of Re is shown in Figure 20b. The simulation results are compared to the predictions of a scaling law $\gamma T = c(\mathrm{Re}_c - \mathrm{Re})^{-1/2}$ with $\mathrm{Re}_c = 81$ and $c = 200$ shown by the solid line in this figure. We find that our simulation results agree well with the results obtained by Aidun [18]. We also find that at higher Reynolds numbers the tumbling period of a fluid-filled rigid capsule is much shorter than that of a solid particle,

indicating that the internal fluid contributes additional torque on the shell. We note that in [132], the tumbling period and angular velocity were found slightly different from our results. This discrepancy can be attributed to a different domain sizes used in [132].

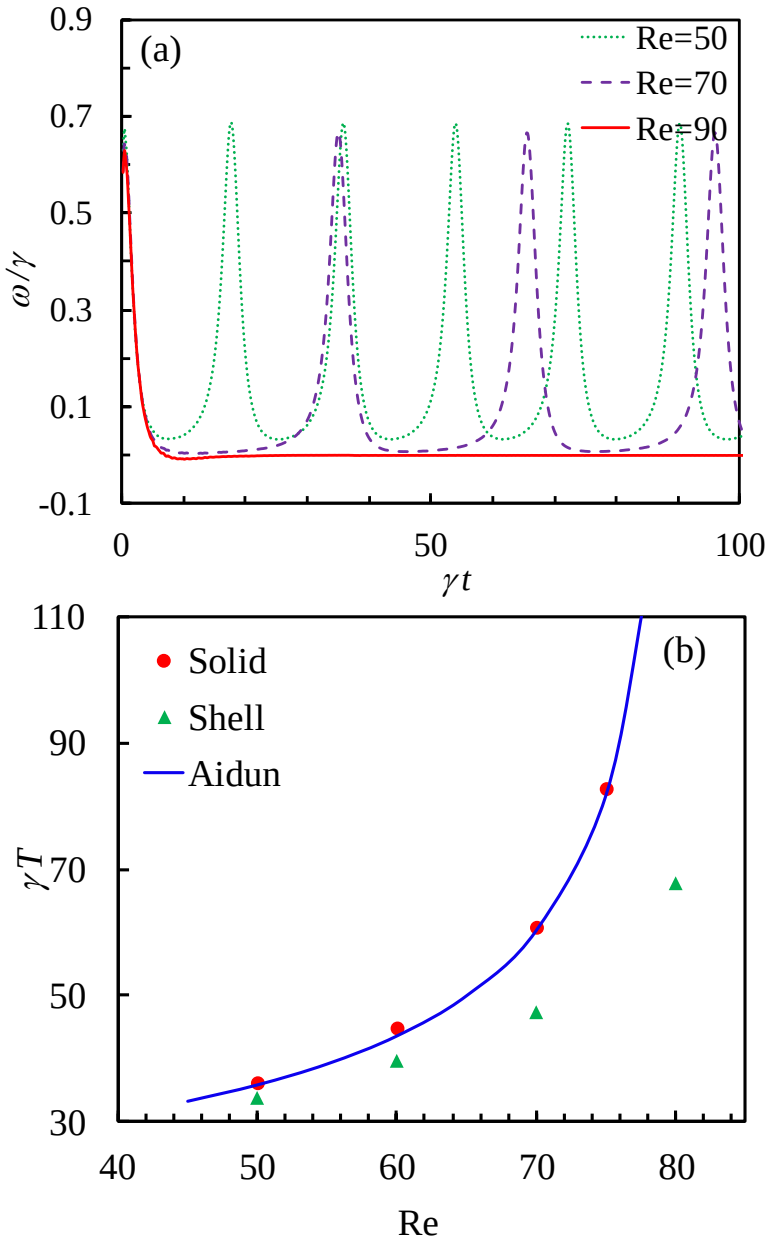

Figure 20 (a) The angular velocity of an oblate spheroid as a function of the non-dimensional time for different Reynolds numbers. (b) The tumbling period of an oblate spheroid as a function of Reynolds number. The prediction of a scaling law is shown by the solid line. The circles are the simulation results of solid particles and the triangles are the results of rigid fluid-filled capsules.

In what follows, we will first examine the rotation behavior when the symmetry axis of a particle rotates around the vorticity axis ($\theta = \pi/2$). The separate effects of particle inertia and fluid inertia are discussed. Next, the three-dimensional rotation of spheroids with different initial orientations is studied. We show that particle and fluid inertia have distinct effects on the equilibrium particle orientation. Moreover, we demonstrate that the initial orientation also affects the steady state of spheroids.

6.3 Rotation around the Vorticity Axis

When the spheroid symmetry axis is initially located in the shear plane, the spheroid remains in this plane at all times. This greatly simplifies the system dynamics. For a massive spheroid with a negligible fluid inertia ($\mathrm{Re} = 0$), the hydrodynamic torque on the spheroid given by Jeffery can be coupled with the equations of motion of the spheroid. In this situation, a second-order ordinary differential equation (ODE) can be derived, $\frac{St}{80}\frac{1-\varepsilon}{1+\varepsilon}\left(\alpha_0 + \frac{1-\varepsilon}{1+\varepsilon}\beta_0\right)\ddot{\varphi} = \varepsilon\left(0.5 - \sin^2\varphi\right) - 0.5 - \dot{\varphi}$, where the parameter $\varepsilon = \frac{a_r^2 - 1}{a_r^2 + 1}$ is a function of the aspect ratio of the spheroid [127, 133]. The non-dimensional coefficients are $\alpha_0 = K\left(1, a_r^{-2}\right)$, $\beta_0 = K(a_r^{-2}, a_r^{-2})$, and $K(C_1, C_2) = \int_0^\infty \frac{d\lambda}{(C_1+\lambda)(C_2+\lambda)\sqrt{1+\lambda}}$.

The above equation can be numerically integrated to obtain φ as a function of time. For negligible small St, the left-hand side of equation is close to zero, reproducing the well-known Jeffery's solution. For non-zero St, both the rotation period and the angular velocity deviate from the Jeffery's solution. For very large St, after an initial

transient, the spheroid rotates with a constant angular velocity $\dot{\varphi}/\gamma = 0.5$ and the rotation period is $T_H = 4\pi/\gamma$.

In order to examine the effect of particle inertia for differently shaped spheroids in a flow without fluid inertia, we conducted simulations for a range of St and a_r, and with the Reynolds number equal to zero. Figure 21 shows how the rotation period and angular velocity normalized by the respective Jeffery's solutions depend on the Stokes number for four different values of a_r. The symbols represent the results of numerical simulations, and the dashed lines represent the theoretical solution [14, 29].

Good agreement between the simulations and the theory in Figure 21 further demonstrates the accuracy of our numerical model. We also find that the deviation from the Jeffery's solution, indicated by non-zero values of the normalized period and angular velocity, increases with the Stokes number. For nearly-spherical particles with aspect ratios close to 1 (see Figures 21a and 21c), the deviation is smaller compared to the particles with large aspect ratios (see Figures 21b and 21d). The period of rotation is only 1% smaller than Jeffery's solution even when $St = 100$ for nearly-spherical particles. On the other hand, the effect of particle inertia on angular velocity cannot be neglected even for nearly-spherical spheroids. As Stokes number increases, the maximum angular velocity decreases and the minimum angular velocity increases, leading to smaller fluctuations of the angular velocity. This trend is consistent with the observation that spheroids rotate with a constant angular velocity for sufficiently large Stokes numbers. Figure 21 also indicates that the effect of Stokes number is significant leading to a difference with Jeffery's solution exceeding about 5% only when $St > 40$.

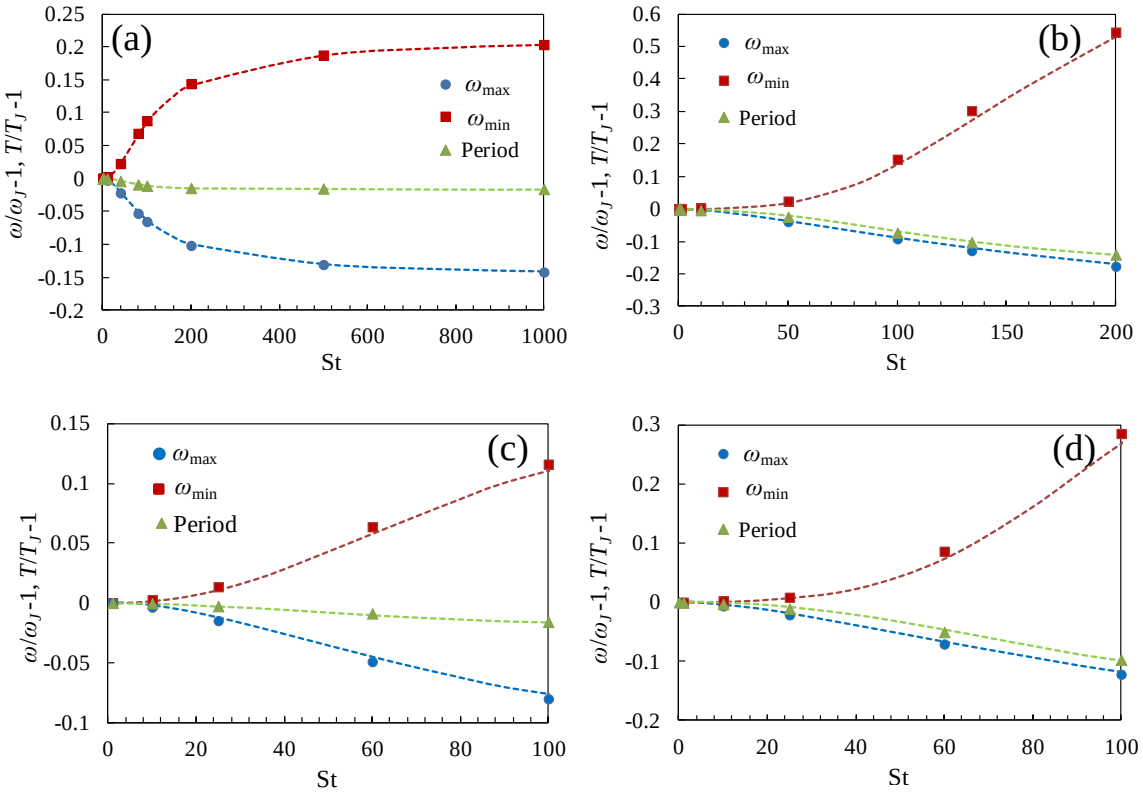

Figure 21 Effect of particle inertia on rotation period and angular velocity for different particle aspect ratios at zero Reynolds number. (a) $a_r = 1.2$, (b) $a_r = 2$, (c) $a_r = 0.8$, (d) $a_r = 0.5$. The symbols are results from simulation and the dash lines are results calculated using analytical theory [14, 29]. Subscript J denotes the Jeffery's analytical solution.

In Figure 22a, we examine the effects of fluid inertia and particle inertia on the angular velocity of a spheroid with $a_r = 2$. For $\mathrm{Re} = 0$ and $St = 0.02$, the numerical result (the solid black line) overlaps with the Jeffery's solution (the dashed blue line). For $\mathrm{Re} = 0$ and $St = 100$, our numerical result (the solid red line) is close to the calculation from the ODE (the dashed red line). During the initial transient of a massive spheroid with $St = 100$, the maximum angular velocity decreases and the minimum angular velocity increases. This observation is consistent with the fact that heavy spheroids tend to rotate with a constant velocity [133]. On the other hand, when $\mathrm{Re} = 20$, $St = 2$ (the

solid green line), the fluid inertia causes both the maximum and the minimum angular velocities to decrease, increasing the overall rotation period.

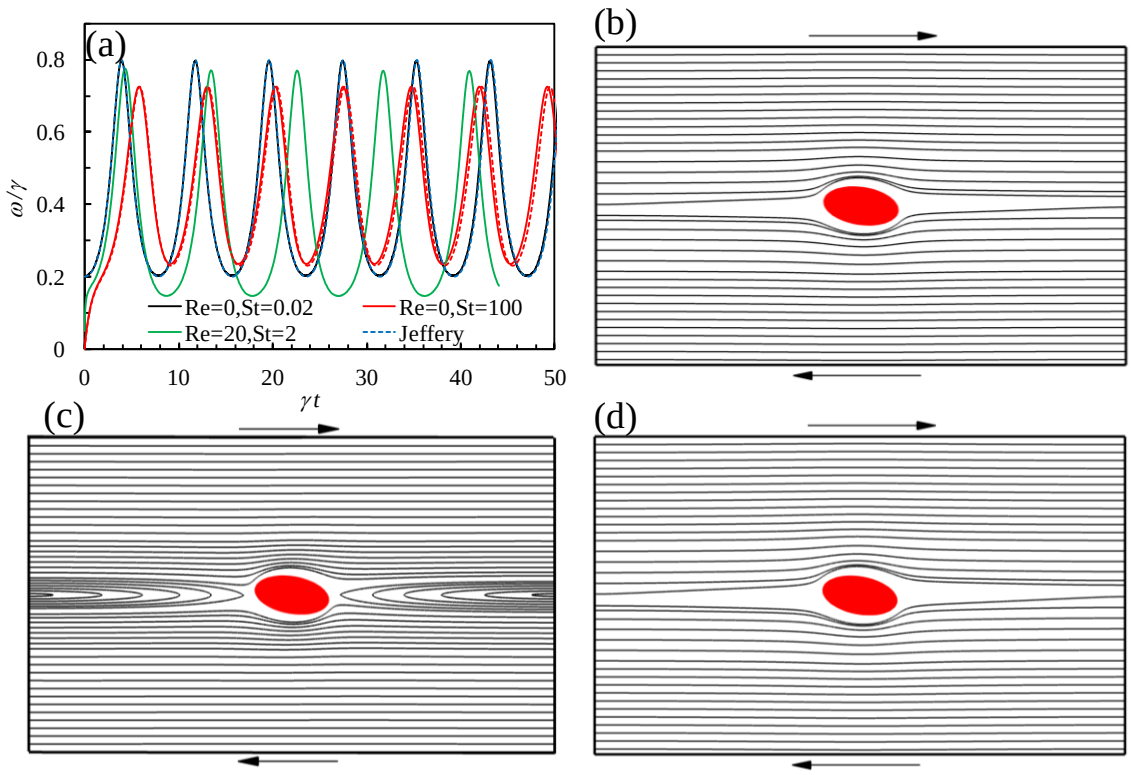

Figure 22 (a) The angular velocity of a spheroid with aspect ratio $a_r = 2$ at different flow conditions. The streamlines in the $x-y$ plane for a prolate spheroid rotating in the shear plane with the instant orientation angle $\varphi \approx -10^{\circ}$. (b) $\mathrm{Re} = 0$, $St = 0.02$, (c) $\mathrm{Re} = 10$, $St = 1$, (d) $\mathrm{Re} = 0$, $St = 100$.

The difference between the effects of particle inertia and fluid inertia can be explained by examining the corresponding flow fields. Figure 22b shows the streamlines for a freely rotating spheroid with negligible small fluid and particle inertia. It can be seen that the flow near the moving top and bottom boundaries creates a positive torque accelerating the rotation [64].

For the rotation with a large fluid inertia (Figure 22c), there is a recirculation region at the center of the channel. Oppositely to the effect of the far-field shear flow, the recirculation region in the fluid has a contribution that acts against the particle rotation direction. This adverse contribution increases with the Reynolds number, increasing the period and reducing the angular velocity of rotation.

Flow around a massive spheroid in a fluid without inertia (Figure 22d) exhibits streamlines that have the same pattern as in the flow around an inertialess spheroid (Figure 22b). It indicates that the particle inertia does not affect the hydrodynamic torque on the particle. Thus, the torque formula obtained by Jeffery can be employed to estimate the effect of particle inertia on spheroid rotation at Re=0 [127].

To further examine the effect of fluid inertia on spheroid rotation, we conduct simulations in which we vary the Reynolds number in the range from 0 to 40 while keeping the value of corresponding Stokes numbers one order of magnitude smaller than that of Re. Figure 23 shows how the normalized rotation period and angular velocity depend on the Reynolds number for different particle aspect ratios. We see that the deviation from the Jeffery's solution increases with Reynolds number. For nearly-spherical particles (Figure 23a, 23c), the deviation is smaller compared to the particles with larger aspect ratios (Figure 23b, 23d). As Reynolds number increases, both the maximum and the minimum angular velocities decrease.

We find that slender particles are more affected by fluid inertia at lower Reynolds numbers. This is similar to the effect of particle inertia on the spheroid dynamics. However, the effect of fluid inertia is more prominent than particle inertia and it should not be neglected even when $\mathrm{Re} = 1$. As we showed above, fluid inertia creates a

recirculation region at the center of the channel and imposes a negative torque on the particle. The magnitude of the negative torque depends on the particle orientation and is maximized when the particle is aligned along the flow. Therefore, the minimum angular velocity occurs when φ is close to 0 and it decreases faster than the maximum angular velocity as Reynolds number increases.

If the Reynolds number exceeds a critical value, the minimum angular velocity decreases to zero. Thus, above the critical Reynolds number, the particle stops rotating and reaches a stable stationary orientation with the symmetry axis tilted by a small angle with respect to the flow direction [122, 129]. Based on this result, we can expect that the critical Reynolds number decreases for slender particles.

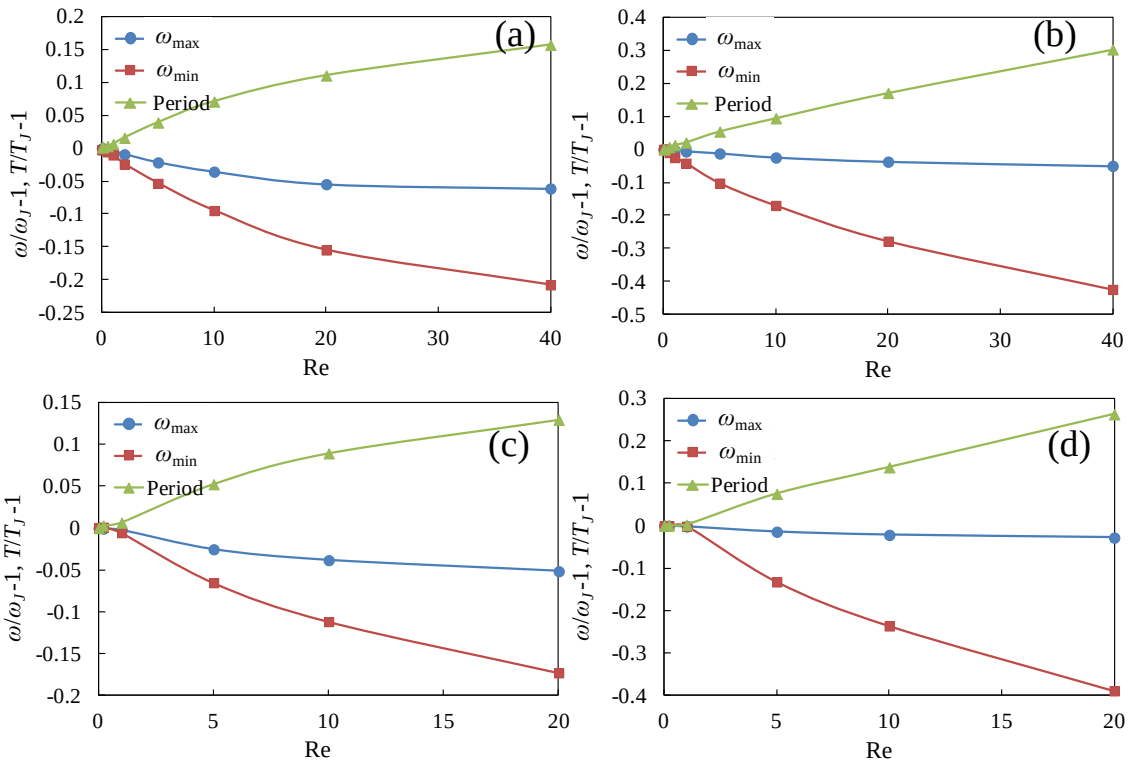

Figure 23 Effect of fluid inertia on rotation period and angular velocity for different particle aspect ratios. (a) $a_r = 1.2$, (b) $a_r = 2$, (c) $a_r = 0.8$, (d) $a_r = 0.5$. Subscript J denotes the Jeffery's analytical solution.

The results presented in this section indicate that particle and fluid inertia have distinct effects on the dynamics of spheroidal particles. Particle inertia does not change the net torque exerted on the particle, but make the particle rotation more uniform. Since the particle inertia does not change the flow pattern, the effects of particle and fluid inertia can be superposed to estimate the rotational dynamics of a particle with an arbitrary density ratio. Furthermore, we can speculate that as the density ratio increases, the critical Reynolds number corresponding to the stationary particle motion increases due to the effect of particle inertia. This hypothesis agrees with the results obtained by Ding [122].

6.4 Rotation in Three Dimensions

It has been previously shown that neutrally buoyant spheroids exhibit different steady or rotation modes as the Reynolds number increases [120, 125, 132]. However, some results from literature contradict each other. Moreover, to the best of our knowledge there are no prior studies that separately examine and compare the effects of fluid inertia and particle inertia. Herein, we focus on the dynamics of spheroid particles at low to moderate Reynolds numbers, and investigate the effects of particle inertia, fluid inertia, and initial orientation.

When the initial orientation angle $\theta \neq \pi/2$, Jeffery's theory predicts that the particle should follow one of a family of closed orbits around the vorticity axis. However, when particle inertia and/or fluid inertia are not negligible, the orbit may be not closed and a drift towards the shear plane (tumbling) or the vorticity axis (rolling) may emerge. During this drift, the orbit parameter, C, is not a constant, but rather changes with time. The evolution of the orbit parameter C can be, therefore, used to characterize the

spheroid drift. For convenience, we introduce a normalized orbit parameter $C_b = C/(C+1)$ that changes in a range [0, 1]. In this case, $C_b = 1$ represents the tumbling motion in the shear plane, while $C_b = 0$ corresponds to the rolling motion.

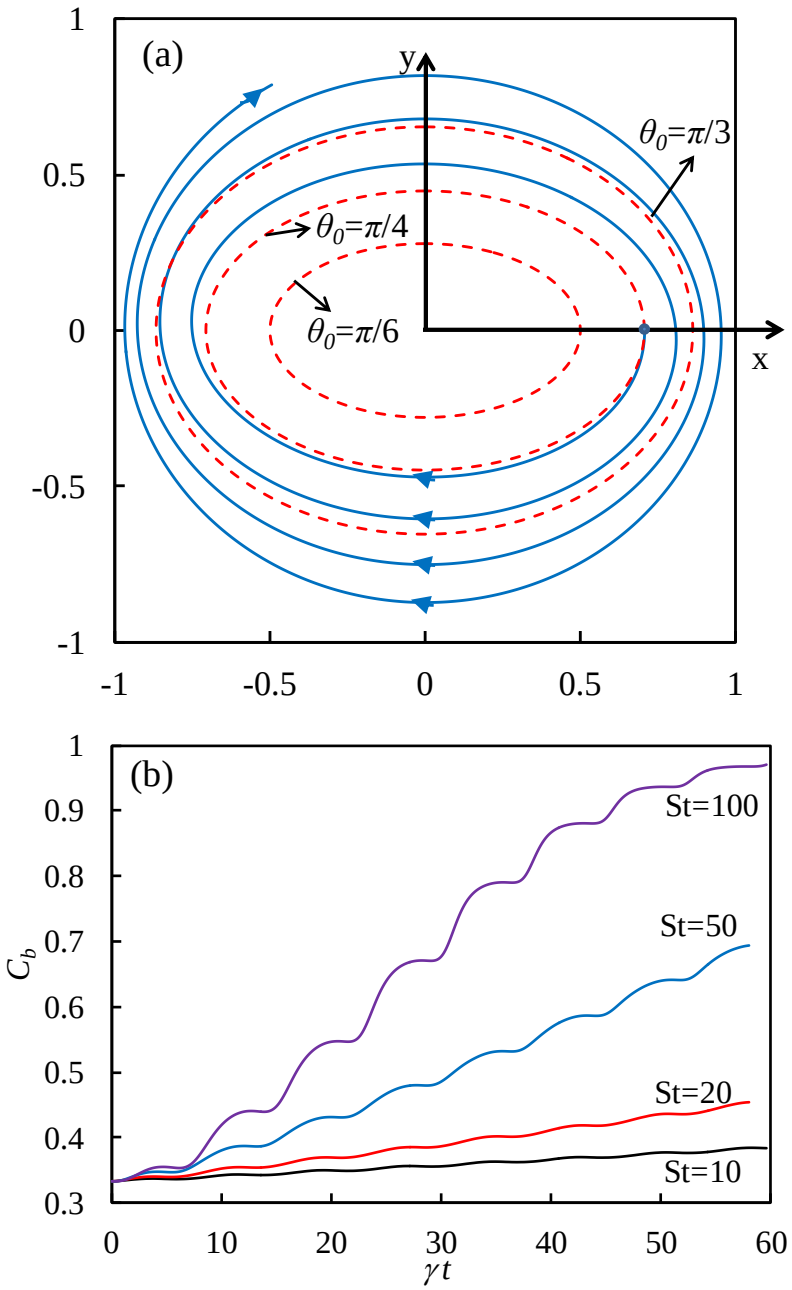

Figure 24 (a) The orbit, projected onto the shear plane, of a prolate spheroid in a shear flow with $a_r = 2$, $St = 50$, $\mathrm{Re} = 0$, and the initial orientation $\theta_0 = \pi/4$, $\varphi_0 = 0$. The dash lines show the closed Jeffery orbits at different orientations. (b) The orbit parameter as a

function of time for different Stokes numbers with $\mathrm{Re}=0$, $a_r=2$, and initial orientation $\theta_0=\pi/4$, $\varphi_0=0$.

In Figure 24a, the orbit of a rotating prolate spheroid with $a_r=2$, $St=50$, and $\mathrm{Re}=0$ is projected onto the shear plane. The spheroid is released with an initial orientation $\theta_0=\pi/4$ and $\varphi_0=0$ indicated by the blue dot in Fig. 24a. We find that the projected orbit spirals out towards the shear plane (the tumbling motion). In the same figure, the dash lines show the corresponding Jeffery orbits in the form of closed ovals. Since in the simulations presented in this figure we excluded the effect of fluid inertia, the drift originates from the particle inertia only.

It has been previously found that the drift precession of a spheroid is a competing effect between centrifugal and gyroscopic forces [134]. The evolution of the orbit parameter is shown in Figure 24b for different Stokes numbers. We find the drift of orbit accelerates as particle inertia increases. Indeed, the figure shows that when the Stokes number is small, particle drifts slowly towards the shear plane. As the Stokes number increases, the drift rate increases. The variation of the orbit parameter is not a linear function of time.

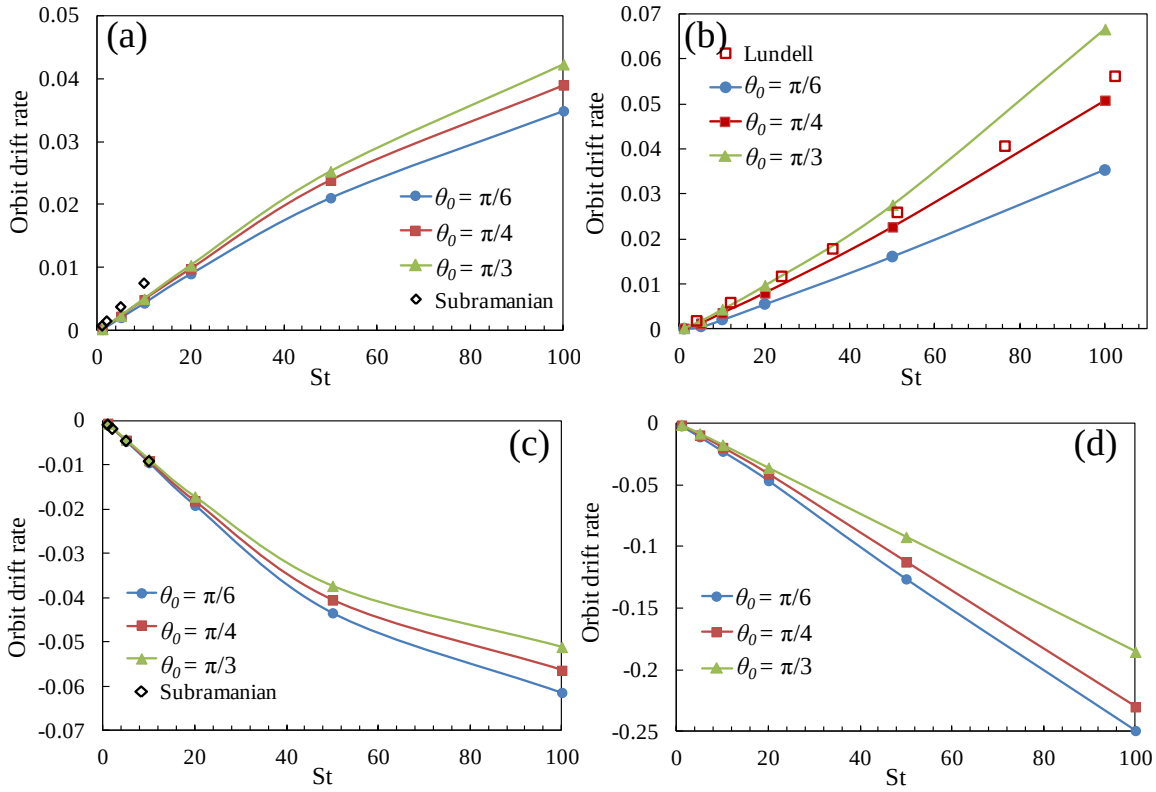

Figure 25 The effect of particle inertia on the orbit drift rate c' for particles with different aspect ratios and initial orientations at $\mathrm{Re} = 0$. (a) $a_r = 1.2$, (b) $a_r = 2$, (c) $a_r = 0.8$, (d) $a_r = 0.5$. In all simulations, $\varphi_0 = 0$. The empty symbols represent the results from the literature [127, 134].

Next, we examine the effect of the initial orientation on the trajectory drift. The orbit drift can be quantified by an orbit drift rate c' [125, 127], defined as $c' = \dfrac{2\ln\left(C(\varphi = -2\pi)/C(\varphi = -\pi)\right)}{\gamma T_J}$. It can be regarded as an increment of the orbit parameter C during one rotating period. Therefore, a positive value of c' means that the orbit drifts towards the tumbling motion, whereas a negative value of c' means that the orbit drifts towards the rolling motion.

In Figure 25, the orbit drift rate c' is shown as a function of the Stokes number for spheroids with different aspect ratios and initial orientations. We find that for prolate

spheroids, particle inertia induces a drift towards the shear plane, while for oblate spheroids, a drift to the rolling motion takes place independent of the initial orientation. This conclusion is consistent with the results of other researchers that particle inertia induces drift towards the rotation about the shortest axis [127, 134].

However, the orbit drift rates are different for different orientations. When the initial orientation θ_0 is closer to the stable orbit ($\theta = \pi/2$ for prolate spheroids, and $\theta = 0$ for oblate spheroids), the orbit drift rate is greater. For nearly spherical particles with a small Stokes number, our numerical results are close to the theoretical analysis [134] shown by the black empty symbols in Figures 25a and 25c. However, the theory does not predict that the drift rate depends on the initial orientation. In Figure 25c, the red empty squares are values obtained following Lundell and Carlsson [127] for prolate spheroids with the aspect ratio of 2 at a zero Reynolds number (note the Stokes number defined in [127] is based on the radius of the particle, thus it is four times smaller than that used here). Our numerical results agree well with the results obtained by Lundell and Carlsson. We also examined several cases with different values of the initial orientation angle φ_0, and found that φ_0 does not significantly affect the drift behavior. It is because φ rotates 2π each period.

We find that particle aspect ratio affects the magnitude of the drift rate. For slender particles shown in Figures 25b and 25d, the drift rates are faster than those of the nearly spherical particles. Furthermore, the drift rate increases with increasing Stokes number. The variation of the drift rate shows a nearly linear behavior with the Stokes number when particle inertia is small. For higher Stokes numbers, the change of the drift rate slows down for particles with nearly spherical shapes (Figs. 25a and 25c).

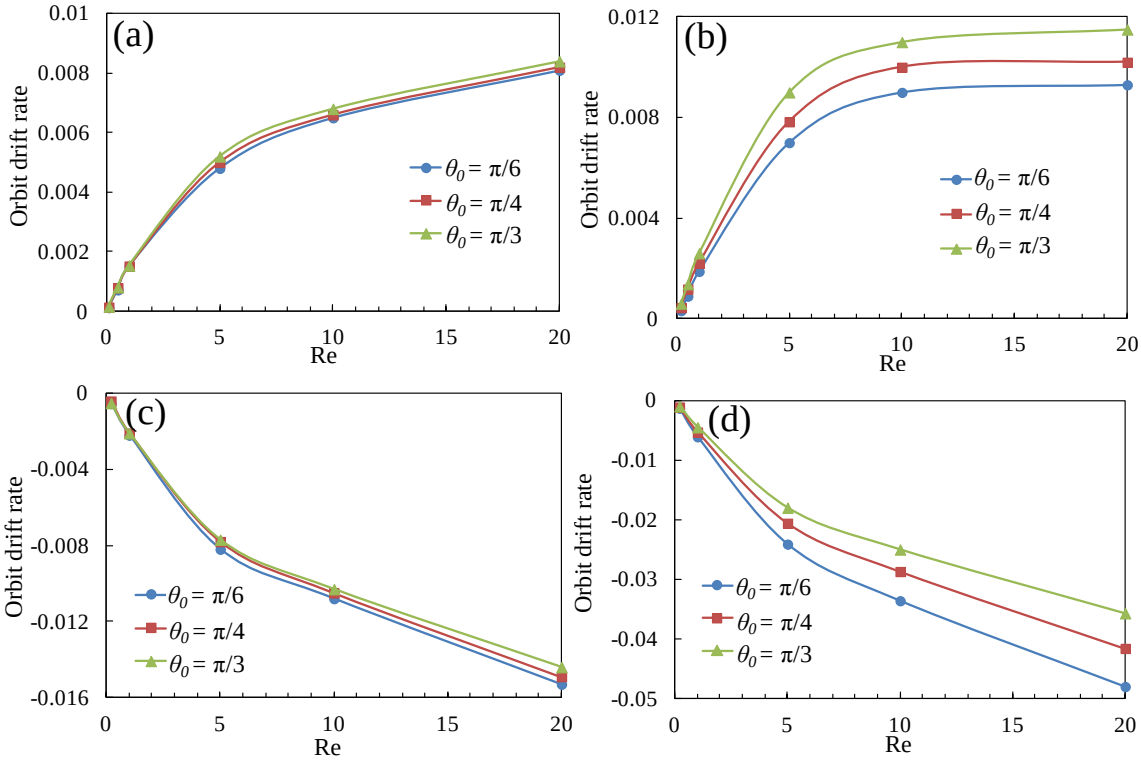

Figure 26 Effect of fluid inertia on orbit drift rate c' for different particle aspect ratios and different initial orientations. (a) $a_r = 1.2$, (b) $a_r = 2$, (c) $a_r = 0.8$, (d) $a_r = 0.5$. In all simulations, $\varphi_0 = 0$.

We probe the effect of fluid inertia on the drift of spheroid particles with relatively small particle inertia. In particular, we examine particles that have inertia which is ten times smaller than the fluid inertia. For prolate spheroids, fluid inertia always induces a drift towards the rotation in the shear plane regardless of the particle aspect ratio and the initial orientation. By contrast, fluid inertia causes oblate spheroids to drift towards the vorticity axis. For Reynolds number less than 20, the orbit drift rate shows a monotonic increase with increasing Re (see Figure 26). This increase depends on the particle aspect ratio. For $a_r = 2$, the growth of orbit drift rate slows down with Re and reaches a plateau when $\mathrm{Re} > 10$.

We find that oblate spheroids exhibit a faster drift towards the vorticity axis when the initial orientation θ_0 approaches zero. For prolate spheroids, on the other hand, a faster drift occurs when θ_0 is close to $\pi/2$. The dependency on the initial orientation is more significant for slender particles (Figures 26b and 26d) that have drift rates larger than that of nearly-spherical particles (Figures 26a and 26c). For nearly-spherical particles, the drift rates are nearly insensitive to the initial orientation. We find that for the parameters used in our study, the effect of particle inertia on the drift rate is comparable to the effect of fluid inertia, which indicates both particle inertia and fluid inertia cannot be neglected.

In order to probe the combined effect of fluid inertia and particle inertia, we conduct simulations of neutrally buoyant particles for which both these effects come into play. We find that the behavior of drift rate is similar to that of inertialess particles in a fluid with inertia. This is because both fluid and particle inertias have the similar effect on the drift rate. Our results contradict to the results for nearly-spherical spheroids obtained by Subramanian & Koch [134]. They found that fluid inertia causes prolate spheroids to drift towards the vorticity axis, while oblate spheroids drift towards the shear plane. We did not see this behavior in our simulations.

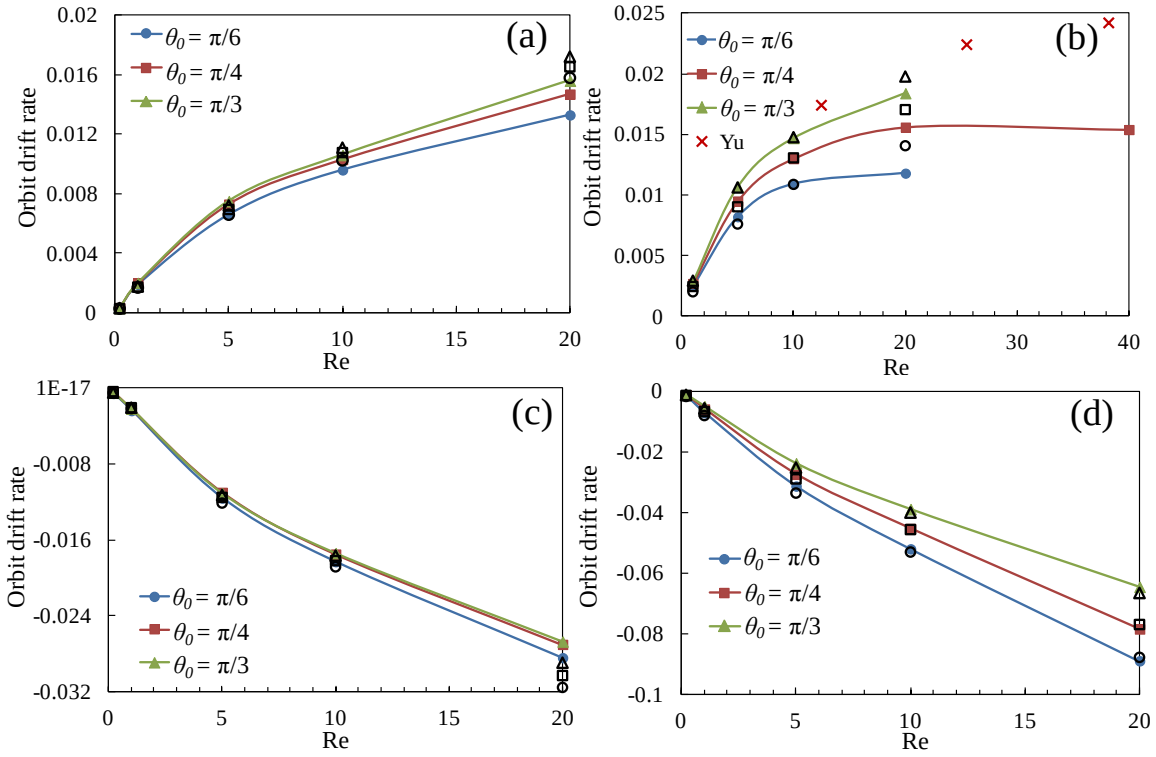

Figure 27 Combined effect of fluid inertia and particle inertia on the orbit drift rate of neutrally buoyant spheroids with different particle aspect ratios and different initial orientations. (a) $a_r = 1.2$, (b) $a_r = 2$, (c) $a_r = 0.8$, (d) $a_r = 0.5$. In all simulations, $\varphi_0 = 0$. The empty symbols are the results of the superposition of fluid inertia effect (Figure 26) and particle inertia effect (Figure 25) calculated separately. The red product symbol represents the results of neutrally buoyant spheroids by Yu [125].

In Figure 27, we also plot the drift rate obtained by superposition of the rates due to fluid inertia and particle inertia that are calculated separately. The superimposed results are rather close to the simulations of neutrally buoyant spheroids, indicating that these effects can be considered to be linearly independent. This result also suggests that the trajectories of particles with different density ratios can be estimated using the superposition of separate results obtained with fluid and particle inertia. When $\mathrm{Re} = 20$, the superimposed results slightly overestimate the orbit drift, indicating nonlinear effects associated with particle and fluid inertia become more significant with increasing Re.

In Figure 27b, we compare our simulations with the results reported by Yu [125] for neutrally buoyant spheroids with $a_r = 2$, $\theta_0 = \pi/4$. While our results show the same trend, there is a discrepancy that increases with increasing Re. The discrepancy can be related to a limited domain size used in [125]. It has been also demonstrated that for a less confined domain, the critical Reynolds number for which the drift changes its direction shifts to a smaller value [132]. This result is consistent with our simulations that show that the maximum drift rate occurs at $\mathrm{Re} \approx 30$, which is smaller than that for a bounded domain where the drift rate reaches its maximum at $\mathrm{Re} \approx 40$ [125].

6.5 Summary

In conclusion, we study the effects of particle inertia and fluid inertia on the motion of spheroid particles in a shear flow. Our results are important for the understanding of motion and orientation of neutrally and non-neutrally buoyant spheroids at low and moderate Reynolds numbers. We draw the following conclusions on the dynamics of spheroid particles:

(i) For prolate spheroids rotating around the vorticity axis, the rotation period and the variations of angular velocity decrease as Stokes number increases. With increasing Reynolds number, both the maximum and minimum angular velocities decrease, and thus the rotation period increases.

(ii) At zero Reynolds number, particle inertia induces particle drift towards the vorticity axis for oblate spheroids, whereas for prolate spheroids, the drift is towards tumbling orbit in the shear plane.

(iii) Inertialess prolate spheroids drift towards the shear plane, whereas for inertialess oblate spheroids, fluid inertia induces a drift towards the vorticity

axis. However, when Reynolds number is sufficiently large, the trend prolate spheroids changes.

(iv) For the low and moderate Reynolds numbers and the densities of particle and fluid are comparable, both fluid inertia and particle inertia are important for orbital drift. When the Reynolds number is relatively small, superposition can be used to estimate the combined effect of fluid inertia and particle inertia on spheroid dynamics.

CHAPTER 7

DYNAMICS OF SPHEROID PARTICLES IN CHANNEL FLOW

7.1 Introduction

Shape represents one of the most important characteristics of biological particles [135]. For example, eukaryotic cells such as yeast show cell-cycle dependent changes in their shape as a budding daughter cell forms attached to the mother cell [136]. Shape is also a useful indicator of cell state in clinical diagnostics. For example, cell shape changes accompany many diseases, such as modified red blood cell morphology resulting from sickle cell disease, anaemia, or malaria [137]. Thus, shape can be a specific marker in bioparticle separation and may serve as a basis for passive particle fractionation. More generally, many biological and synthetic particles of interest such as parasites, bacteria, viruses, but also marine organisms [138], man-made microparticles and microcapsules [139, 140] possess a variety of shapes and the ability to separate particles with particular shapes enables subsequent medical and industrial applications.

The motion of spheroid particles in a pressure-driven channel flow is encountered in a broad range of biological and engineered systems. Therefore, understanding the dynamics of spheroid particles in channel flow would not only help us explain the phenomena encountered in particle suspensions, but also provides the practical guideline for developing new approaches for separation and focusing of non-spherical particles [130].

The dynamics of a single spherical particle at a finite Reynolds number has been investigated extensively for a pressure-driven Poiseuille flow. In 1962, Segre and Silberberg [11] observed that rigid neutrally buoyant spheres in a pipe flow migrated to

an equilibrium position located at a radius of $r \approx 0.6R$, with R being the pipe radius. Schonberg and Hinch [13] studied the inertial migration of a sphere in a plane Poiseuille flow at small Reynolds numbers ($\mathrm{Re}_c = 1-75, \mathrm{Re}_p << 1$), and found that the equilibrium position moves towards the wall as Reynolds number increases. Asmolov [14] extended the matched asymptotic approach of Schonberg to higher Reynolds numbers (up to 1500).

The migration away from the channel centerline is attributed to the competing effects of the curvature of the velocity profile and the wall influence [77, 141]. Recently, experiment conducted by Matas [142] confirmed that the equilibrium position moves towards the wall of a pipe as Reynolds number increases. It was found that an additional equilibrium position exists at the inner radius of the pipe for $\mathrm{Re} > 700$. Matas [143] extended the asymptotic expansion to cylindrical channels. All the theories were developed under an assumption that the presence of a particle does not affect the velocity field, i.e. a point-particle assumption was used.

Only a few studies considered the effect of the particle size. Di Carlo [144] and Chun [145] studied the migration of confined particles through rectangular cross-section microchannels. More recently, Bhattacharya [146] analytically investigated the inertia-induced radial migration of finite sized particles inside a narrow cylindrical channel. These works revealed the importance of the effects associated with particle size on the overall behavior of a particle suspension at a finite Re.

There is a limited number of studies that examine the orientation dynamics of spheroid particles in a Poiseuille flow. Chwang and Wu [147] solved the Stokes equations to determine the motion of a spheroid in unbounded quadratic flows. They

showed that the spheroid moves in a straight line parallel to the flow direction without any lateral drift. Sugihara-Seki [148] numerically studied a rigid ellipsoid in a Poiseuille flow through a narrow tube in the zero-Reynolds-number limit. He found that a prolate spheroid either tumbles or oscillates depending on the particle-tube size ratio, the aspect ratio of particle, and the initial conditions.

A large oblate spheroid may approach a steady trajectory located closer to the tube centerline. Pan et al. [149] simulated the motion of a neutrally buoyant ellipsoid in Poiseuille flows and found that its rotation exhibits distinctive states depending on the Reynolds number and the shape of the ellipsoid. Chen et al. [150] investigated the motion of single and multiple neutrally buoyant elliptical cylinders in a plane Poiseuille flow. They found for a single elliptical cylinder with small channel size ratio ($K < 0.2$), the cylinder with a higher aspect ratio moves closer to the centerline and has a higher translational velocity. For a larger channel size ratio, as Reynolds number increases, the cylinder consequently exhibits full rotation, oscillatory rotation, and finally a pure translational motion.

In spite of the progress made in these previous studies, the relationship between the orientation dynamics and the center of mass trajectory of spheroids in a Poiseuille flow remains unclear. In this chapter, we will conduct a systematic investigation of the motion of spherical and spheroid particles in planar Poiseuille flow.

In what follows, we first study the inertia migration of spherical particles in a plane Poiseuille flow. The effect of particle size will be examined. Then, we focus on the inertia migration of spheroid particles when the symmetry axis of the particle rotates around the vorticity axis. Finally, the three-dimensional rotation and migration of a

spheroid in a channel flow is investigated with the emphasis on the steady state motion of neutrally buoyant spheroids.

7.2 Computational Setup

We consider a channel of height H filled with a viscous fluid with viscosity μ and density ρ (Figure 28). A neutrally buoyant spherical or spheroid particle is introduced into the flow. Spherical particles are characterized by the diameter d, whereas spheroid particles are characterized by the semi-axes a and b, and the particle aspect ratio $a_r = a/b$.

To characterize the flow within the channel, we defined a channel Reynolds number $\mathrm{Re}_c = \rho U_m H/\mu$, where U_m is the maximum velocity of the undisturbed fluid flow. The channel Reynolds number represents the ratio between fluid inertia and viscous forces. The effect of inertia on particle motion is characterized in terms of a particle Reynolds number $\mathrm{Re}_p = \mathrm{Re}_c \alpha^2$. Here, $\alpha = d/2H$ is the channel confinement ratio of spherical particles, whereas for spheroidal particles, the confinement ratio is $\alpha = a/H$ for prolate spheroids, and $\alpha = b/H$ for oblate spheroids.

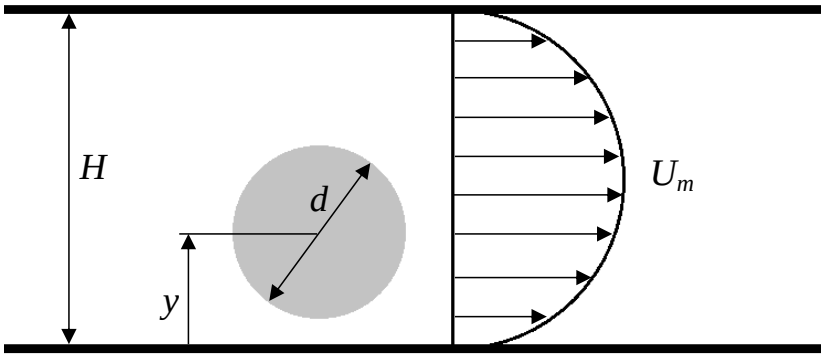

Figure 28 Schematic of a neutrally-buoyant solid particle propelled by a pressure-driven channel flow.

We impose a non-penetration, no-slip boundary condition at the top and bottom walls of our computational box which has height H. In the x and z directions, we apply periodic boundary conditions. For spherical particles, we set the lateral size of the computational box equal to $10d$. For prolate spheroid particles, we set $L = 20a$, $W = 13a$. For oblate spheroid particles, we set $L = 20b$, $W = 13b$. We have verified that the dimensions of our periodical computational box are large enough and so they do not affect the results of our simulations.

In all of our simulations, the initial velocity distribution inside the channel was set to match a plane Poiseuille flow. Particles are released with zero translational and angular velocities. Hereafter, we only present our results for the lower half of the channel flow, since they are symmetric with respect to the channel centerline.

7.3 Inertial Migration of Spherical Particles

We first examine the cross-stream inertial migration of spherical particles in a channel with a small confinement ratio $\alpha = 0.025$. In this case, the effect of particle size is weak allowing direct comparison with theoretical solutions for $\alpha \to 0$ [13, 14]. In Figure 29, we show the dimensionless migration velocity as a function of the distance from a channel wall. We find that particle lateral velocity is positive when it is closer to the wall and negative closer to the channel centerline. The positive velocity means that particle migrates away from channel wall, whereas the negative velocity indicates the migration away from the centerline. Thus, there is a stable off-center equilibrium position where particle velocity is zero.

To validate our computational model, we compare the simulations for rigid spherical particles with theoretical results for different Reynolds numbers [13, 14]. We

find good agreement between our simulations and the theory in terms of the particle drift velocity and the equilibrium positions where the drift velocity is zero. We find a discrepancy between our model and the theory in the near-wall region. This discrepancy can be explained by the fact that the Stokes expression for the drag force $F_L = 3\pi\mu d V_p$ used to calculate the theoretical value of drift velocity is not valid near the wall. Thus, overall agreement between the simulations and theory indicates that our computational method can properly capture the non-linear effects associated with inertia drift of solid particles in a channel flow.

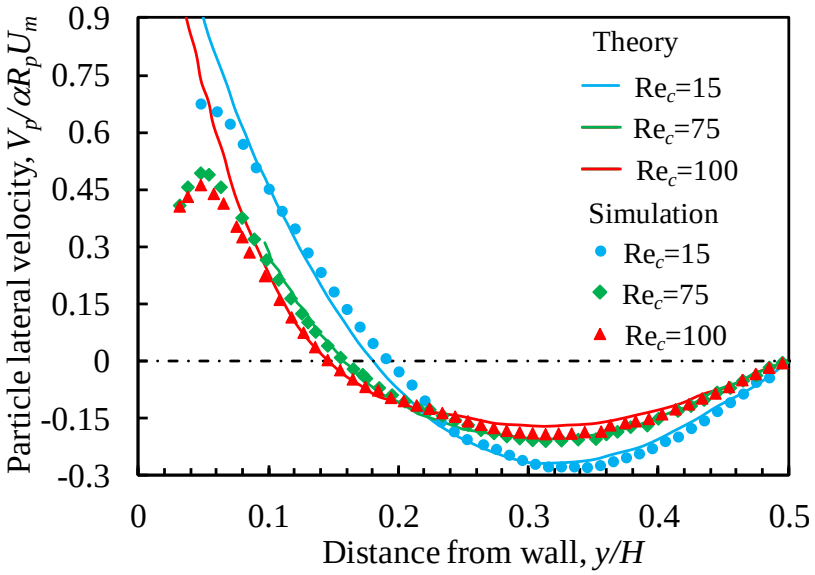

Figure 29 Cross-stream migration velocities of rigid spherical particles in channels with different Reynolds numbers. The symbols show the results of our numerical simulations with confinement ratio $\alpha = 0.025$, whereas the solid line presents the theoretical data [13, 14].

After validating the computational model in the limit of small particles, we apply our model to explore the behavior of particles in confined channels. In Figure 30, we plot the dimensionless particle migration velocity as a function of the normalized distance from the channel centerline. The dimensionless distance $(H-2y)/(H-d)$ is in the

range between 0 and 1. The value of 1 corresponds to the limiting case where the particle is in contact with the wall. The data in Figure 30 is presented for a range of Reynolds numbers. We find that as the confinement ratio and/or the Reynolds number increase, the magnitude of dimensionless cross-stream velocity decreases.

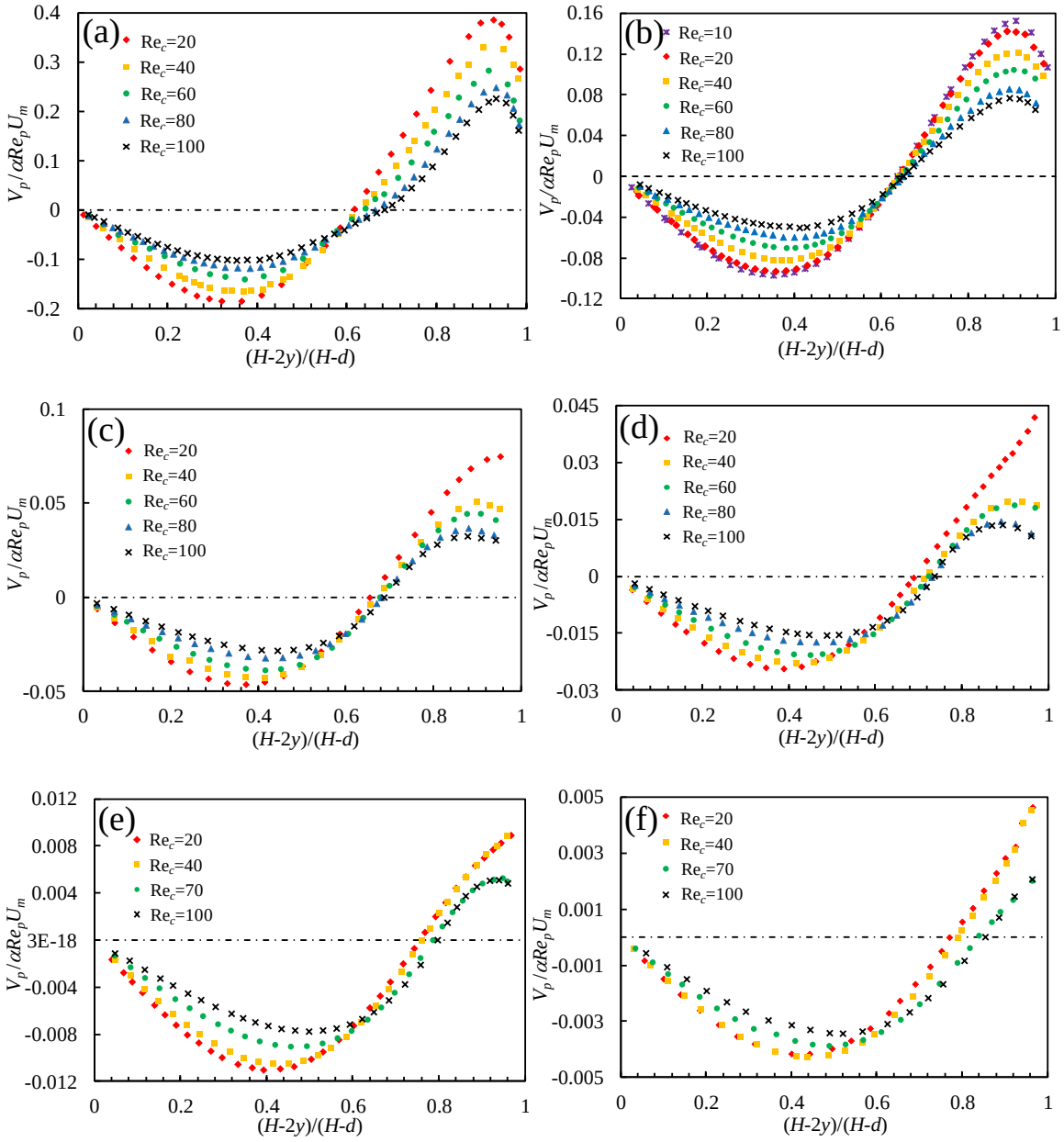

Figure 30 Dimensionless cross-stream migration velocities of rigid spherical particles in confined channels with different Reynolds numbers and confinement ratios. (a) $\alpha = 0.05$, (b) $\alpha = 0.1$, (c) $\alpha = 0.15$, (d) $\alpha = 0.2$, (e) $\alpha = 0.25$, (f) $\alpha = 0.3$.

Figure 30 shows that the migration velocities exhibit similar trends for different Reynolds numbers and confinement ratios. Therefore, it can be potentially expected that there is a universal scaling that can be used to represent all data in terms of a single function. Indeed, a scaling law of the drift velocity $V_p \sim \alpha \,\mathrm{Re}_c\, U_m$ has been previously reported for square channels [144] and for cylindrical channels [146]. This scaling law gives good results when the confinement ratio is in the range of $0.1 \le \alpha \le 0.2$ and when the particle is located near the channel centerline.

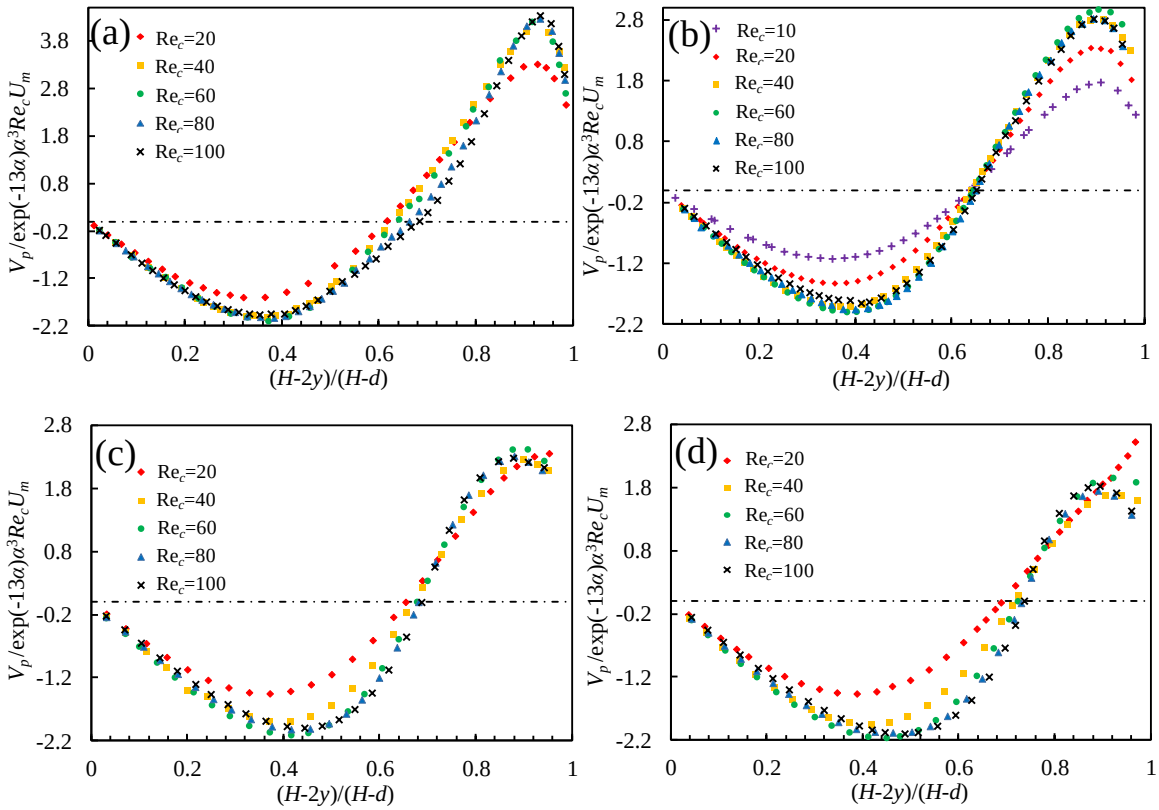

Figure 31 Scaled cross-stream velocities for different Reynolds numbers and confinement ratios. (a) $\alpha = 0.05$, (b) $\alpha = 0.1$, (c) $\alpha = 0.15$, (d) $\alpha = 0.2$.

Our data suggest that the results can be fitted more accurately using the following scaling $V_p \sim \alpha^3 \exp(-13\alpha)\,\mathrm{Re}_c^{0.5}\, U_m$. This scaling is shown in Figure 31 for a wide range

of channel Reynolds numbers and confinement ratios. The figure shows that the scaled velocity collapses to a single curve for $0.05 \le \alpha \le 0.25$ and $\mathrm{Re}_c \ge 40$.

In Figure 32, we plot particle equilibrium position as a function of Reynolds number for different confinement ratios. We find that the equilibrium position shifts towards the wall with increasing Reynolds number. We also find that particle equilibrium position is dependent on the confinement ratio. When α large, particle is equilibrated near the channel centerline, whereas for smaller confinement ratio the equilibrium position is closer to the wall. This result points to a potential application of dynamically measuring particle size based on their trajectories in a channel flow.

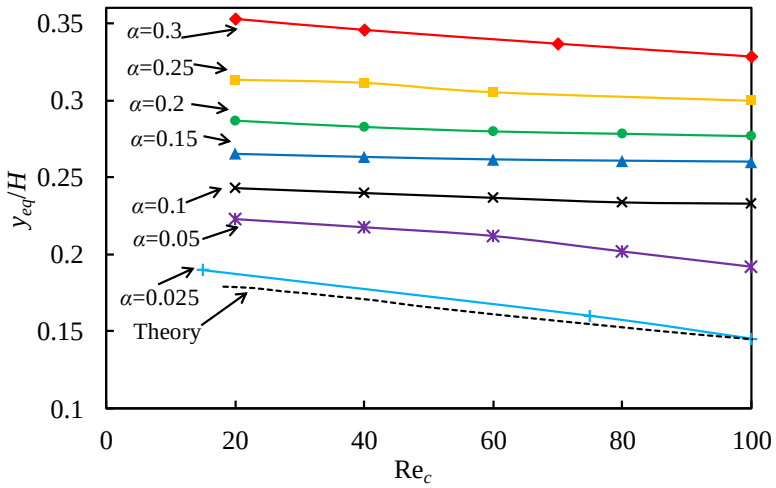

Figure 32 Particle equilibrium position as a function of Reynolds number at different confinement ratios. The dotted line shows theoretical data from [14].

7.4 Dynamics of Spheroid Particles

With the knowledge of the dynamics of spherical particles in a Poiseuille flow, we now turn to the motion of neutrally buoyant spheroid particles. Unlike spherical particles, the orientation dynamics of spheroids need to be investigated.

If a spheroid is initially located in the shear plane ($\theta = \pi/2$), the particle remains in this plane at all times. This greatly simplifies the dynamics of the system and we first consider this scenario. We simulate spheroid particles with different aspect ratios and different initial positions propelled by a channel flow. Figure 33 shows trajectories of spheroids with different aspect ratios in a channel with $\mathrm{Re}_c = 40$ and $\alpha = 0.15$. Two particles are released from a position that is close to the channel centerline, whereas two other particles are released closer to the wall. All the particles migrate to equilibrium trajectories located midway relative to the initial release positions of the particles. The particles periodically oscillate as they follow the equilibrium trajectories. We denote the average height of the equilibrium trajectory $y_{eq} = \langle y_p \rangle$ as the particle lateral equilibrium position in the channel.

We find that the equilibrium position of the spheroids with the same a_r coincides independent of the particle initial position. For particles with larger a_r, y_{eq} is slightly closer to the wall and the migration time required to reach the equilibrium position is longer compare to particles with smaller a_r.

The oscillations of trajectories, which are induced by the rotation of the spheroid, are more pronounced when particles are closer to the wall. The amplitude of the oscillations also depends on the aspect ratio. Figure 33b shows the cross-stream velocity of the particle center of mass as the particle moves along the equilibrium trajectory for several rotation periods. The instantaneous cross-stream velocity of a spheroid is zero when its major axis is aligned with the flow direction, and is the maximum when its major axis is nearly perpendicular to the flow direction. The figure shows that the particle

with higher aspect ratio has slightly larger velocity oscillations and rotation period. Although the velocity oscillates, the period-averaged cross-stream velocity is zero.

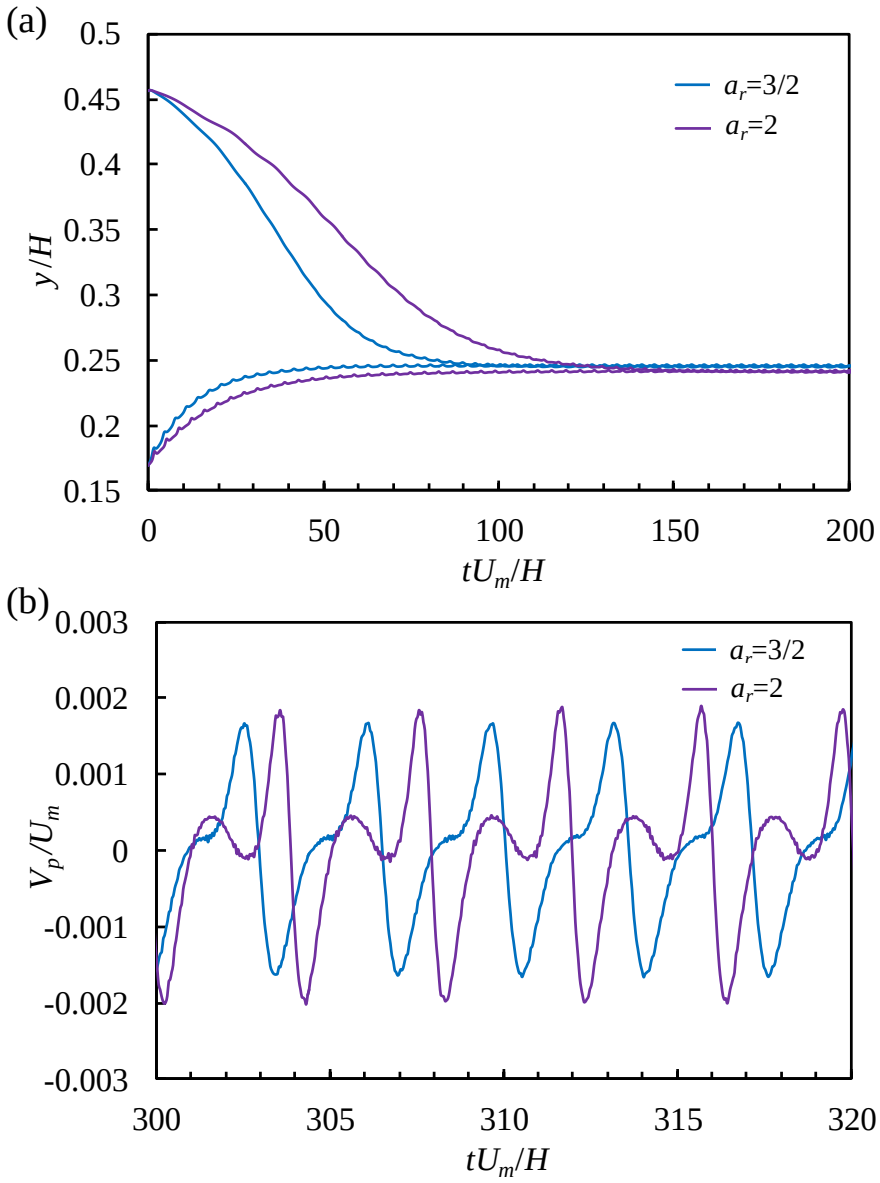

Figure 33 (a) Lateral migration of a spheroid with different aspect ratios in a channel with $\mathrm{Re}_c = 40$ and $\alpha = 0.15$. (b) Cross-stream migration velocity at the equilibrium trajectory versus time for spheroids with different aspect ratios at $\mathrm{Re}_c = 40$, $\alpha = 0.15$.

In Figure 34, we plot the period-averaged lateral migration velocity of spheroids with different aspect ratios and Reynolds numbers as a function of normalized distance

from the channel centerline. To normalize the distance, we use $d = 2a$ for prolate spheroids and $d = 2b$ for oblate spheroids. We find that compared to spherical particles for which $a_r = 1$, spheroids have smaller migration velocities and the equilibrium positions of spheroidal particles are closer to the wall.

For the same Reynolds number, the magnitude of migration velocity increases as the channel confinement ratio α increases. This increase is related to a steeper velocity gradient in more confined channels which accelerates the migration of particles to the equilibrium position. Furthermore, when particles are close to the wall, the wall induced lift is stronger due to a smaller distance between particle surface and the wall. For a fixed confinement ratio, we find that the migration velocity is faster for larger Re due to stronger nonlinear effects.

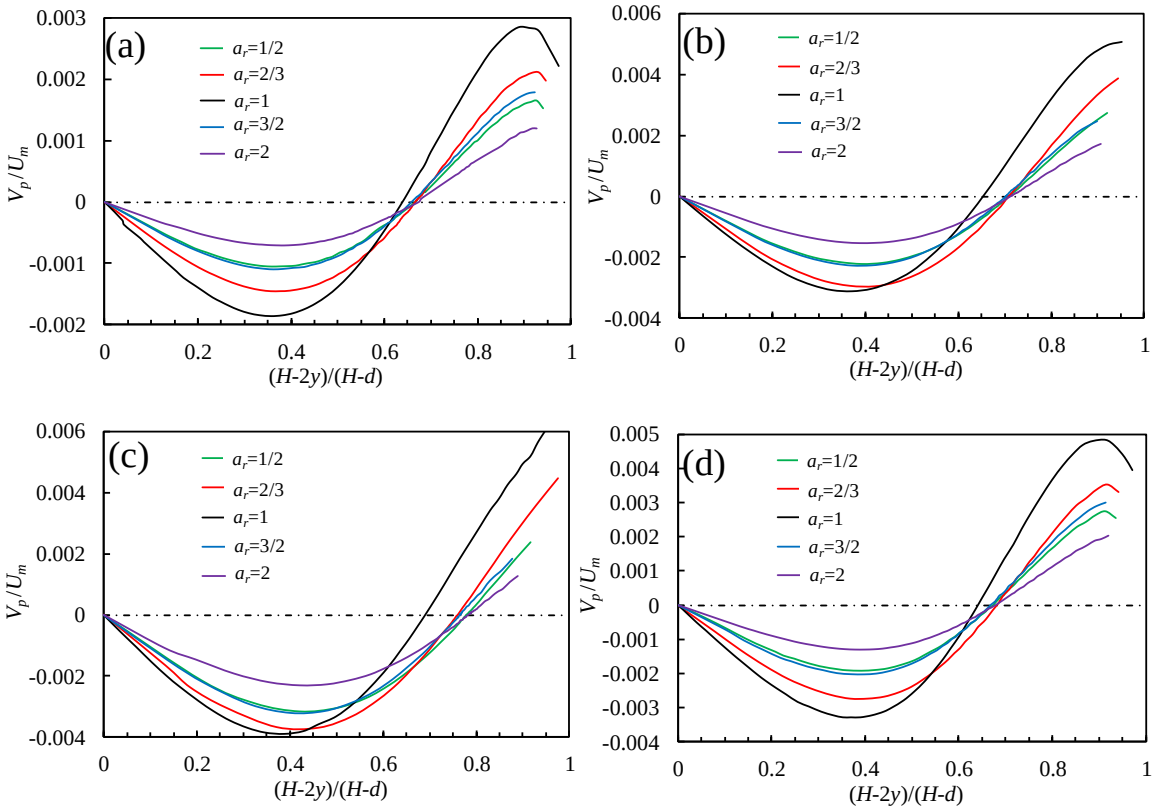

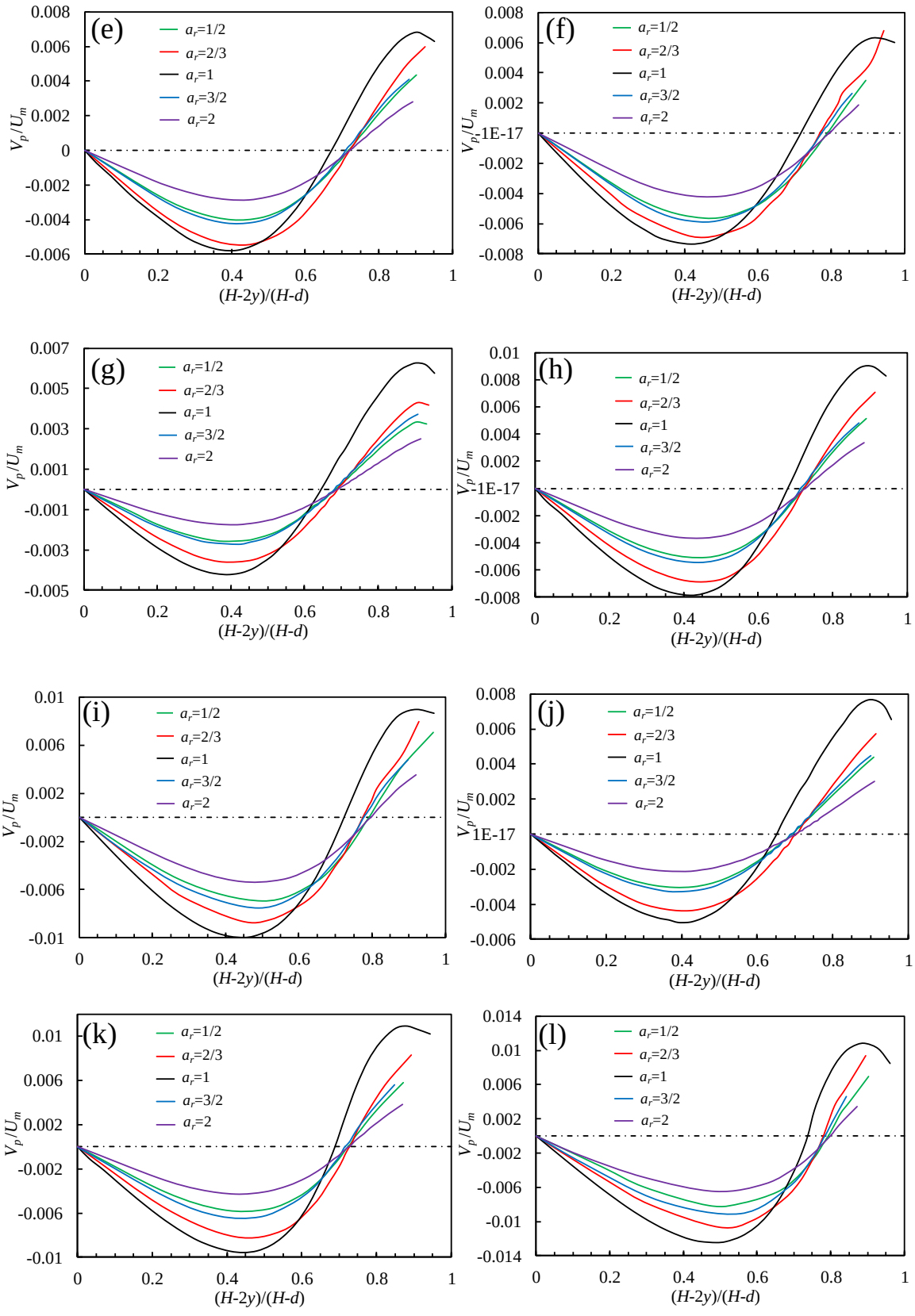
(e)
(f)
(g)
(h)
(i)
(j)
(k)
(l)
a_r=1/2
a_r=2/3
a_r=1
a_r=3/2
a_r=2
V_p/U_m
(H-2y)/(H-d)

Figure 34 Dimensionless cross-stream migration velocities of rigid spheroidal particles in confined channels with different Reynolds numbers and confinement ratios. (a) $\alpha = 0.1$, $\mathrm{Re}_c = 20$, (b) $\alpha = 0.15$, $\mathrm{Re}_c = 20$, (c) $\alpha = 0.2$, $\mathrm{Re}_c = 20$, (d) $\alpha = 0.1$, $\mathrm{Re}_c = 40$, (e) $\alpha = 0.15$, $\mathrm{Re}_c = 40$, (f) $\alpha = 0.2$, $\mathrm{Re}_c = 40$, (g) $\alpha = 0.1$, $\mathrm{Re}_c = 60$, (h) $\alpha = 0.15$, $\mathrm{Re}_c = 60$, (i) $\alpha = 0.2$, $\mathrm{Re}_c = 60$, (j) $\alpha = 0.1$, $\mathrm{Re}_c = 100$, (k) $\alpha = 0.15$, $\mathrm{Re}_c = 100$, (l) $\alpha = 0.2$, $\mathrm{Re}_c = 100$.

Figure 34 shows that the lateral migration velocity depends on the channel Reynolds number, confinement ratio, and particle aspect ratio. Based on the scaling for spherical particles, we construct a similar scaling for spheroidal particles that also incorporates the parameters relevant to spheroids. We find that the migration velocity scales as $e^{-13\alpha_V}\alpha_V{}^3\,\mathrm{Re}_c^{0.5}U_m$ for $0.05 \le \alpha_V \le 0.2$ and $\mathrm{Re}_c \ge 40$. The scaled data is plotted in Figure 35 which shows that data for different particles collapse into a single curve with acceptable accuracy.

Note that the volumetric confinement ratio $\alpha_V = r_V / H$ used in the above scaling is calculated using an equivalent radius $r_V = \sqrt[3]{abc}$ that corresponds to a sphere with a volume equal to that of the spheroid. For example, when the confinement ratio equals to 0.1, the corresponding volumetric confinement ratios are 0.063, 0.0763, 0.0794, and 0.0874 for spheroids with a_r equal to 2, 1.5, 0.5, and 2/3, respectively. Thus, lateral migration velocity of spheroidal particles can be estimated using the migration velocity of a sphere with the same volume.

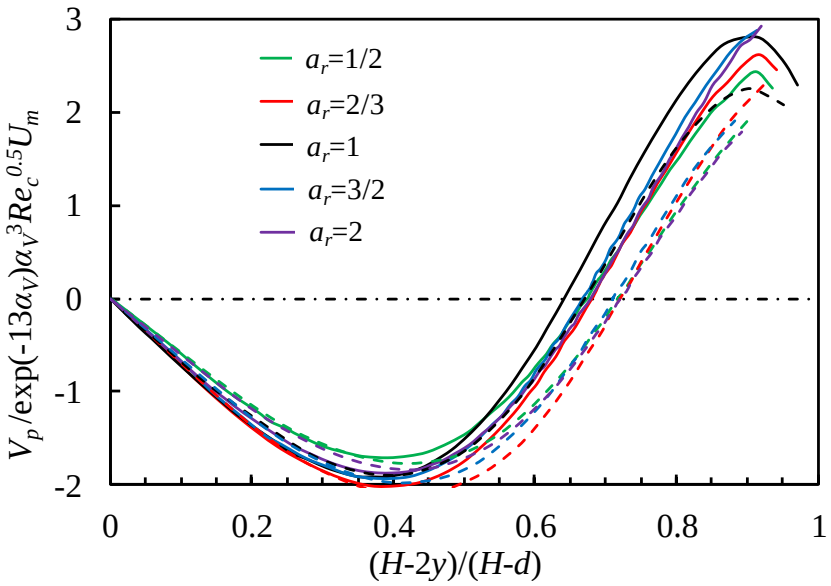

Figure 35 Normalized cross-stream velocity as a function of the fractional distance from the channel centerline for different aspect ratios when $\mathrm{Re}_c = 40$. Solid lines denote cases with $\alpha = 0.1$ and dashed lines denote cases with $\alpha = 0.15$.

In Figure 36, we plot particle equilibrium positions as a function of Reynolds number for different confinement ratios. The solid symbols represent results for spherical particles. We find that the equilibrium position shifts towards the wall with increasing Reynolds number. We also find that the particle equilibrium positions depend on the confinement ratio. When α is large, particles equilibrate near the channel centerline, whereas for smaller confinement ratios the equilibrium positions are closer to the wall.

For prolate spheroids, the stable motion is tumbling, thus the length of both major and minor axes affects the spheroid trajectory and equilibration. It has been suggested that the equilibrium position of spheroids can be estimated based on the equilibrium position of a sphere with the radius equal to the major axis of the spheroid [130]. Figure 36a indicates that this approximation is inaccurate. The figure shows that the equilibrium position of a spheroid with $a_r = 2$ and a confinement ratio $\alpha = 0.2$ is about the same as

the equilibrium position of a sphere with a confinement ratio $\alpha = 0.15$. Similar behavior is found for a spheroid with $a_r = 1.5$ shown in Figure 36b.

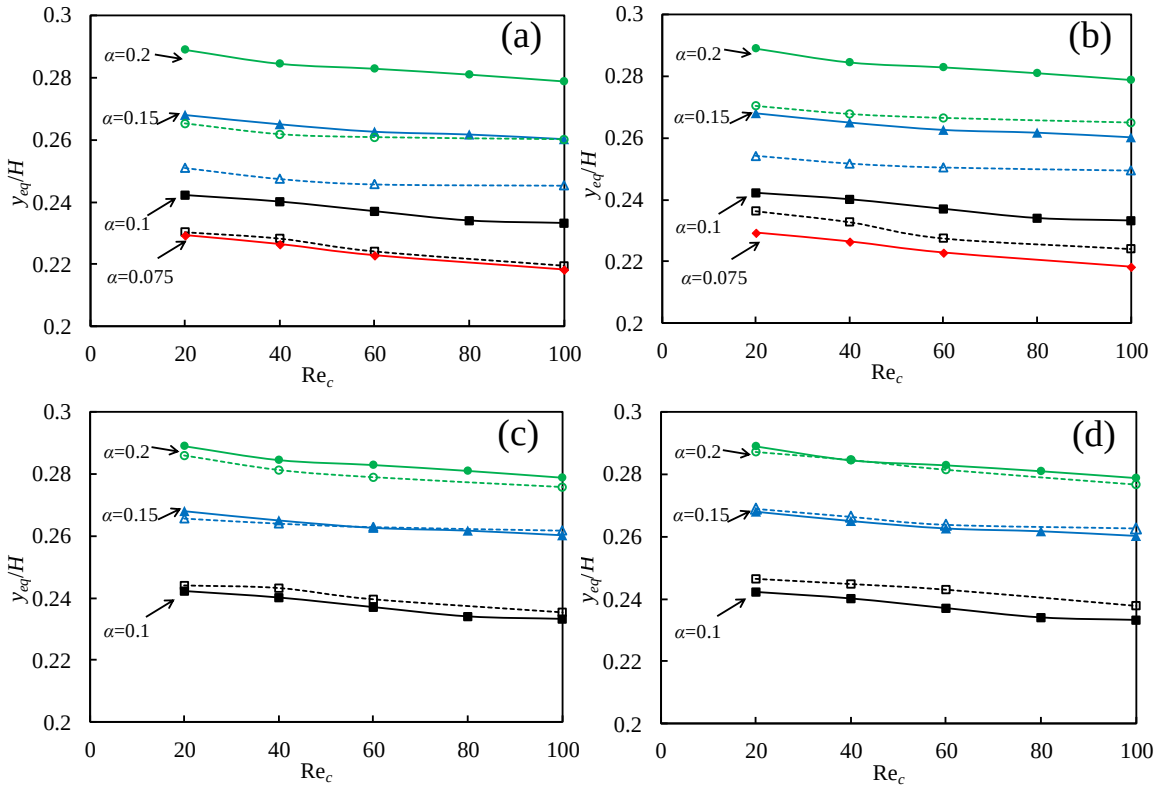

Figure 36 Equilibrium positions of particles as a function of Reynolds number at different confinement ratios. The solid lines denote the results for spherical particles, and the dashed lines denote the results for spheroids. (a) $a_r = 2$, (b) $a_r = 1.5$, (c) $a_r = 2/3$, (d) $a_r = 0.5$. Note that for oblate spheroids shown in (c) and (d), particles equilibrate when they rolls with the symmetry axes parallel to the vorticity axis.

The equilibrium positions of spheroids can be estimated more accurately using the equilibrium position of spheres with the same cross-sectional area, rather than the diameter equal to the major axis. Figure 37 shows the equilibrium positions as a function of area confinement ratio $\alpha_A = \alpha/\sqrt{a_r}$. We find that the data for spheroids with $0.5 \le a_r \le 2$ fits well the curve obtained for spheres. For example, when the confinement ratio equals to 0.1, the corresponding area confinement ratios α_A are 0.0707 and 0.0817

for prolate spheroids with aspect ratio equals to 2 and 1.5, respectively. For this reason, the equilibrium position of a spheroid with $a_r = 2$ at a confinement ratio 0.1 is close to a sphere at confinement ratio $\alpha = 0.075$ shown by the red line in Figure 36a. For oblate spheroids at rolling motion (Figures 36c and 36d), we find that their equilibrium positions are close to that of spheres with the same confinement ratios. The latter can be explained by the fact that the area confinement ratio α_A for rolling oblate spheroids and spheres are identical.

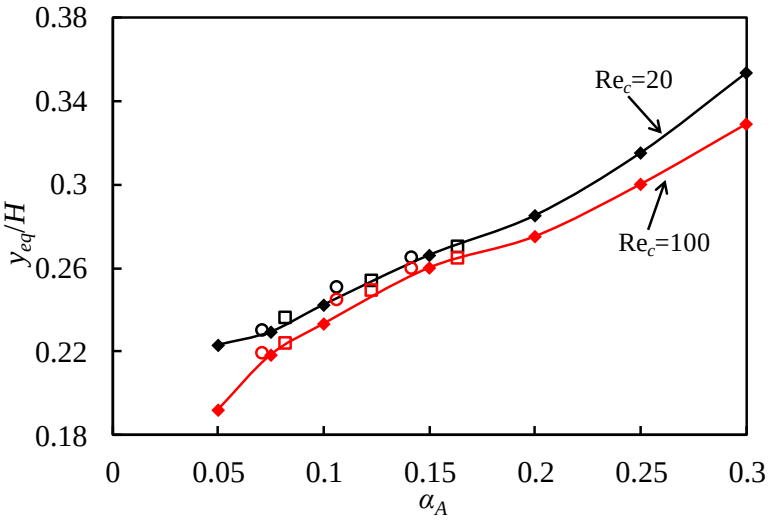

Figure 37 Equilibrium positions as a function of area confinement ratio. The solid lines and the symbols denote the data for spheres, the empty circle symbols denote the data for spheroids with $a_r = 2$, and the empty square symbols represent the data from spheroids with $a_r = 1.5$.

Figure 38 shows the rotational period and the angular velocity of particles that undergo tumbling when moving along the equilibrium trajectory. In this figure, the values are normalized by the local shear rate in the channel flow, $\gamma = (4 - 8y_p/H)U_m/H$. For comparison, we also include the Jeffery's solutions that are shown by the solid and dotted lines [114]. Specifically, the rotation period of a spheroid is given by

$T_J = 2\pi(a_r + a_r^{-1})/\gamma$, and the maximum and minimum angular velocities are $\omega_{J,\max} = \gamma a^2/(a^2+b^2)$ and $\omega_{J,\min} = \gamma b^2/(a^2+b^2)$, respectively.

We find that both the maximum and the minimum angular velocities in a channel flow are slightly smaller than the Jeffery's solutions, pointing to a longer rotation period. As Reynolds number increases, the deviation from Jeffery's solutions increases. This trend is similar to the results we obtained for spheroids in a simple shear flow (see chapter 6). We also find that the deviation is greater for slender spheroids. Channel confinement ratio also affects the rotation. In more confined channels, spheroids rotate slower with a smaller angular velocity. This reduction in the angular velocity can be, therefore, attributed to the influence of channel walls on particle motion.

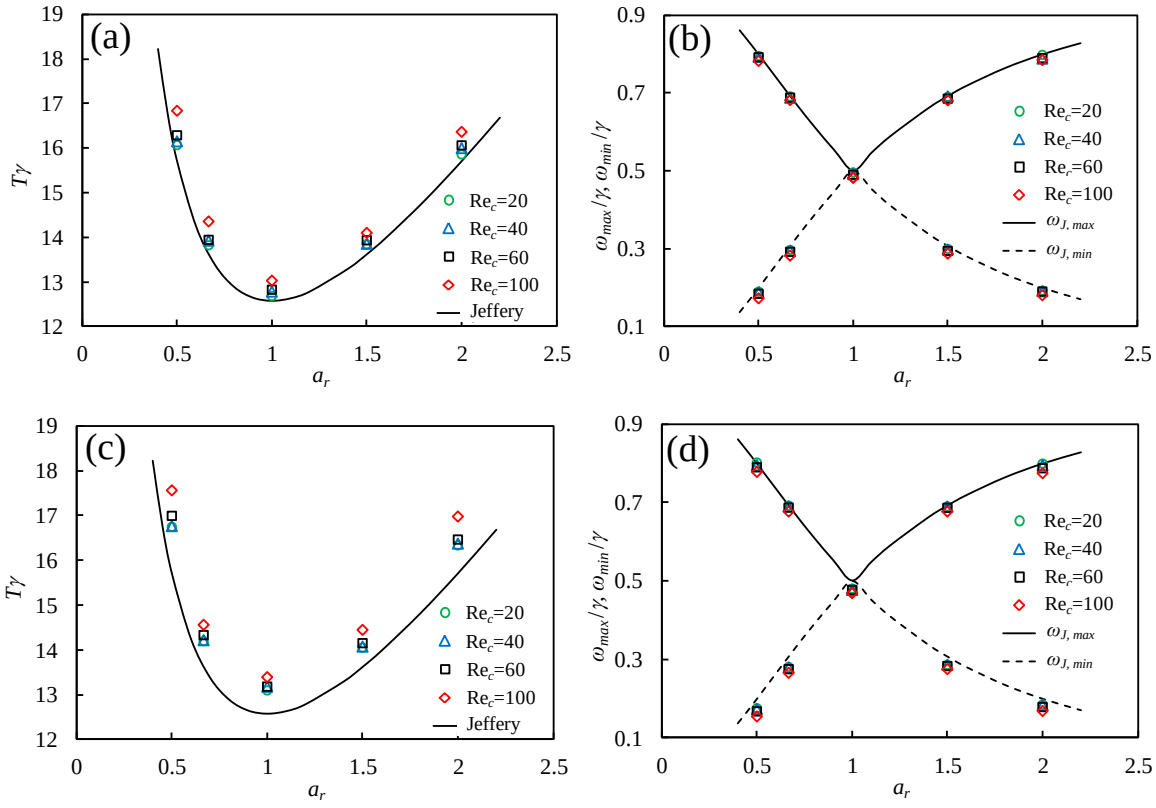

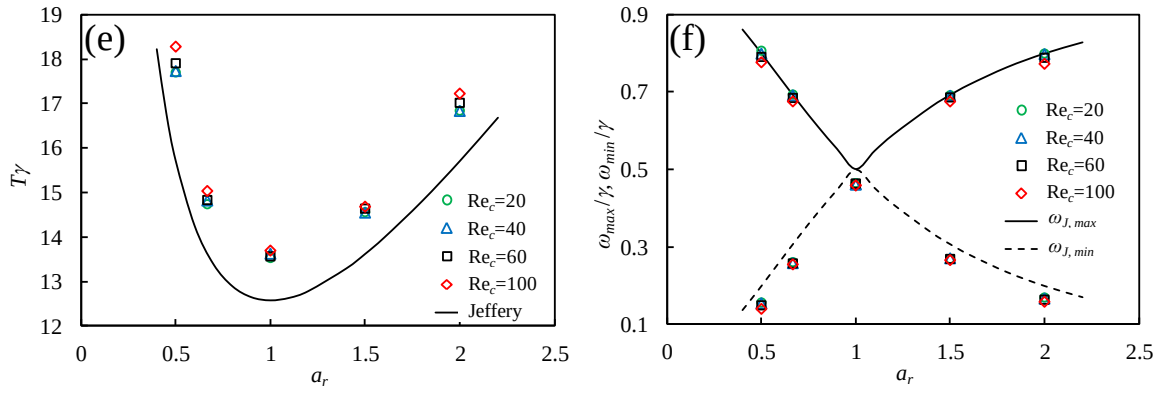

Figure 38 The rotational period and the angular velocity at the equilibrium position when particles undergo the tumbling motion at various Reynolds numbers. Jeffery's solutions are also plotted for comparison. (a), (b) $\alpha = 0.1$; (c), (d) $\alpha = 0.15$; (e), (f) $\alpha = 0.2$.

When the initial orientation angle $\theta \neq \pi/2$, spheroid particles exhibit different rotation modes. Staben et al. [151] numerically studied the three-dimensional motion of neutrally buoyant spheroids in a Stokes flow. They found that spheroids can exhibit a two-dimensional oscillating motion, a two-dimensional tumbling motion, three-dimensional oscillations, or three-dimensional tumbling depending on the initial center location and initial orientation.

Using experiments in a rectangular channel, Masaeli et al. [130] classified the rotational modes of prolate spheroids as "in plane rotation" (tumbling), "out of plane rotation", and "no rotation". They found that as Reynolds number increases, the frequency of rotational modes decreases and most of the particles follow a tumbling motion. This implies that the latter two modes may not be the stable rotational modes. Our previous study shows that prolate spheroids in an unbounded shear flow drift to the tumbling motion, while oblate spheroids possess a stable rolling motion after a transient precession. In what follows, we focus on the rotational behavior of spheroids in a planar channel flow.

To investigate the orbit change, we define orbit drift rate as $c' = \frac{2\ln\left(C(\varphi=-2\pi)/C(\varphi=-\pi)\right)}{\gamma T_J}$ [125, 127], where C is the orbit parameter. Thus, a positive c' means the orbit drifts towards the tumbling motion, while a negative c' means the orbit drifts towards the rolling motion. In Figure 39, the orbit drift rate is shown as a function of the Reynolds number for spheroids with different aspect ratios and initial orientations. The Reynolds number is based on the local flow shear rate and is defined as $\mathrm{Re}_S = 4\rho_l a^2\gamma/\mu$ for prolate spheroids and $\mathrm{Re}_S = 4\rho_l b^2\gamma/\mu$ for oblate spheroids. Here, the local shear rate γ is calculated based on the averaged center position of the particle. Even though we simulate particles with the same channel Reynolds number, the particles may have different Re_S depending on their location within the flow.

We find that for prolate spheroids, the inertia induces a drift towards the shear plane (tumbling motion), while oblate spheroids drift towards the rolling motion. This drift takes place regardless of the initial orientation and the initial position. This result is consistent with the stable rotational modes of spheroids in an unbounded shear flow. In other words, the stable equilibrium rotational mode of prolate spheroids is tumbling, while for oblate spheroids, the stable equilibrium mode is rolling.

The orbit drift rates are different for different initial orientations (see Figure 39). When the initial orientation θ_0 is closer to the stable orbit ($\theta = \pi/2$ for prolate spheroids, and $\theta = 0$ for oblate spheroids), the orbit drifts faster. Particles with different aspect ratios show similar dependencies of the orbit drift rate on Re.

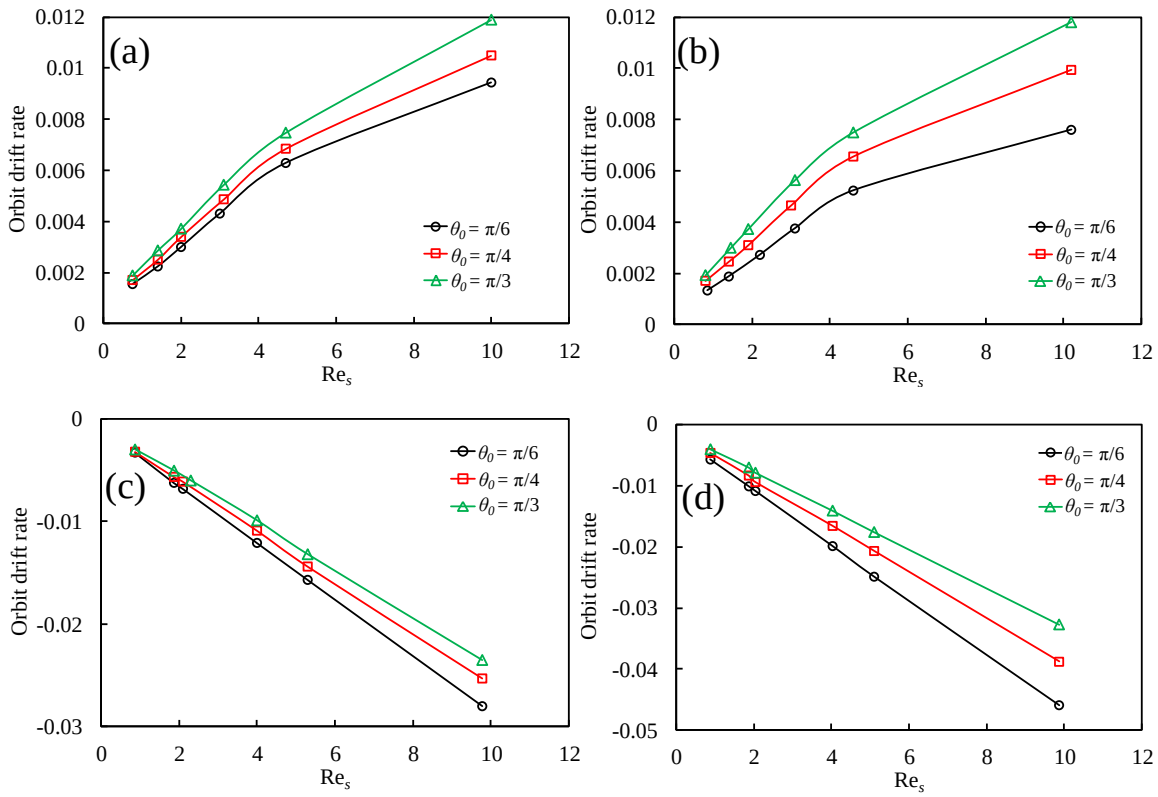

Figure 39 Effect of fluid inertia on the orbit drift rate c' for different particle aspect ratios and initial orientations in a channel flow with $\alpha = 0.1$. (a) $a_r = 1.5$, (b) $a_r = 2$, (c) $a_r = 2/3$, (d) $a_r = 0.5$. In all simulations, $\varphi_0 = 0$.

The results in Figure 39 are for the channel confinement ratio equal to $\alpha = 0.1$. We have also examined the behavior of orbit drift in channels with $\alpha = 0.2$. We find the trends for prolate spheroids to drift to the tumbling mode and for oblate spheroids to drift to the rolling mode are similar to those found in the wider channel. Furthermore, we find that the drift rate at the same Re_S is smaller for $\alpha = 0.2$ compared to channel with $\alpha = 0.1$.

In the previous section, we have demonstrated that spheroids initially orientated in the $x-y$ plane migrate monotonically in the cross-stream direction to an equilibrium trajectory. We find, however, that particles with other initial orientations can also exhibit

a non-monotonic migration. For example, when a prolate spheroid is released with an initial orientation close to the rolling motion, it may first migrate closer to the wall where rolling particles equilibrate, and then as the orbit drifts to the tumbling motion, the particle can migrate to a new equilibrium trajectory located closer to the channel centerline. This overshooting phenomenon is observed in our simulations (Figure 40).

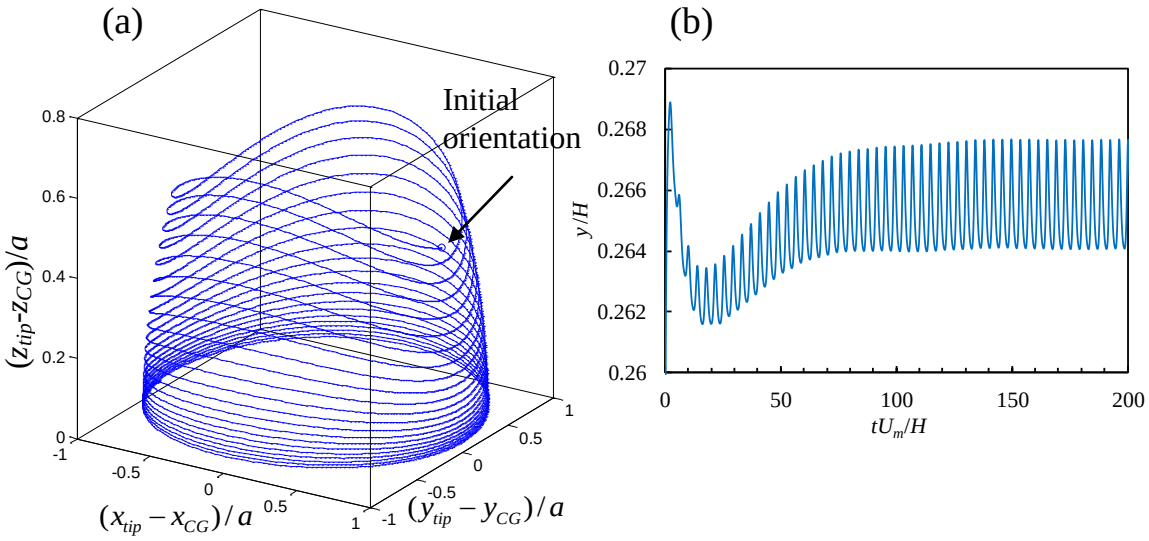

Figure 40 (a) Trajectory of the particle tip ($x_{tip}, y_{tip}, z_{tip}$) with respect to the particle center of mass (x_{CG}, y_{CG}, z_{CG}) and (b) temporal evolution of the lateral migration for a particle with aspect ratio $a_r = 1.5$ at $\mathrm{Re}_c = 60$, $\alpha = 0.2$.

7.5 Summary

In conclusion, the motion of neutrally buoyant spherical and spheroid particles in a planar Poiseuille flow has been studied. We have shown that the equilibrium position of spherical particles depends on channel confinement ratio. We also provide a detailed investigation of the motion of spheroids in a planar channel flow. It is found that the stable motion of prolate spheroids is tumbling, whereas the stable motion of oblate spheroids is rolling. These stable rotation modes are independent of the particle initial

orientation and the channel confinement ratio. The lateral migration velocity of spheroids in tumbling can be estimated using the migration velocity of spheres with the same volume. The equilibrium positions of spheroids are close to those of spheres with the same cross-sectional area. We propose a scaling for the lateral migration velocity that includes the effects of the channel confinement ratio, particle aspect ratio, and Reynolds number. Finally, the rotational period of particle at equilibrium is compared with the Jeffery's solution. It is found that the period is longer than that predicted by the Jeffery's theory. The period increases with increasing Reynolds number. The deviation from Jeffery's solution is greater for slender particles.

CHAPTER 8

CONCLUDING REMARKS AND OUTLOOK

In this study, a fluid-structure interaction model was used to examine the dynamics of solid particles in a viscous flow. The computational model is based on the lattice Boltzmann model combined with the lattice spring model. We showed that this fully-coupled three-dimensional model can accurately simulate complex dynamics of compliant and non-spherical particles in a fluid flow at finite Reynolds numbers.

We used computer simulations to design a ridged microchannel that hydrodynamically separate solid particles by size. Specifically, particles with different sizes follow distinct trajectories as a result of the nonlinear inertial effects and secondary flows created by diagonal ridges in the channel. This new continuous separation method offers high throughput, enhanced resolution, and simple channel layout, enabling simple integration in lab-on-a-chip devices for autonomous particle processing.

We developed a computational model to investigate the motion of biological cells in microfluidic channels. We examined the utility of ridged microchannels for high-throughput separation of biological cells by their differential stiffness. Cells with different stiffness squeezed through narrow gaps between solid diagonal ridges and the channel wall and migrate across the microchannel with different rate depending on their stiffness. This deformability-based microfluidic separation method can be used for detecting diseased cells, as a variety of cell pathologies manifest through the change in cell mechanics.

We employed our computational model to explore the dynamics of spheroid particles in a simple shear flow and in a Poiseuille flow. The effect of particle inertia and fluid inertia on the motion of spheroid particles has been studied. We showed that increasing fluid inertia suppresses the oscillations of particle rotational velocity and results an increased rotational period. Particle inertia and fluid inertia both affect the orbital drift of spheroid particles. Prolate spheroids drift towards the shear plane, while oblate spheroids drift towards the vorticity axis. We also demonstrated that superposition can be used to estimate the combined effect of fluid inertia and particle inertia.

Inertial migration of spherical and spheroid particles in a planar Poiseuille flow was examined. We identified a scaling for particle migration velocity that integrates the effects of channel confinement ratio, particle aspect ratio, and Reynolds number. It is also found that the stable motion of prolate spheroids is tumbling, whereas the stable motion of oblate spheroids is rolling. The dependence of equilibrium trajectory on particle shape points to a potential application of a microchannel flow for shape based particle separation.

The results of our studies advance the basic understanding of complex hydrodynamic interactions governing the motion of solid particles in a channel fluid. Our results help to develop engineering guidelines for designing new high-throughput microfluidic devices for sorting, focusing, and separation of synthetic solid particles and biological cells.

Flow of particle suspensions is a complex process that poses multiple challenging problems to the researches. Our work is focused on just several specific examples

involving the dynamics of deformable and non-spherical solid particles in a viscous flow in the dilute limit. Based on our results we can suggest the following future studies.

A study of densely concentrated suspensions is a direct extension of our current work. In concentrated suspensions, particle-particle interactions are important. Small distances between particles require the model to take into account lubrication forces. We can expect that particle concentration and finite fluid inertia can significantly alter the rheology of dense suspensions and affect the macroscopic response of the material to forces.

Investigation of a blood flow is a further extension of our work. LSM can be extended to simulate the mechanics of red blood cells (RBC) and platelets. It is suggested that deformability of RBCs leads to non-Newtonian behavior of blood. This model could be used to better understand the dynamics of blood flow in the microcirculation with curved geometry and bifurcations. Therefore, it is important to examine the interactions between cells and blood vessel walls. Cell adhesion in the microcirculation can play a critical role in the development of different physiological conditions.

The cell model used in our work is rather simple and does not incorporate any effects associated with internal structure of a cell. The mechanical properties of cytoskeletal networks are intimately involved in determining the behavior and mechanics of living cells. Therefore, the development of a mesoscopic cell model integrating cell membrane, cytoplasm, and cytoskeleton will enable new investigations that can reveal interesting and important insights into the physics of cell mechanics.

REFERENCES

1. Aidun CK & Clausen JR (2010) Lattice-Boltzmann Method for Complex Flows. *Annu Rev Fluid Mech*, Annual Review of Fluid Mechanics, (Annual Reviews, Palo Alto), Vol 42, pp 439-472.

2. Einstein A & Fürth R (1956) *Investigations on the Theory of the Brownian Movement* (Dover Publications).

3. Happel J & Brenner H (1965) *Low Reynolds number hydrodynamics, with special applications to particulate media* (Prentice-Hall, Englewood Cliffs, N.J.).

4. Leal LG (1992) *Laminar flow and convective transport processes : scaling principles and asymptotic analysis* (Butterworth-Heinemann, Boston [etc.]).

5. Batchelor GK (1970) The stress system in a suspension of force-free particles. *J Fluid Mech* 41(03):545-570.

6. Jeffrey DJ & Onishi Y (1984) Calculation of the resistance and mobility functions for two unequal rigid spheres in low-Reynolds-number flow. *J Fluid Mech* 139:261-290.

7. Kim S & Mifflin RT (1985) The resistance and mobility functions of two equal spheres in low-Reynolds-number flow. *Phys Fluids* 28(7):2033-2045.

8. Batchelor GK (1977) The effect of Brownian motion on the bulk stress in a suspension of spherical particles. *J Fluid Mech* 83(01):97-117.

9. Brady JF & Morris JF (1997) Microstructure of strongly sheared suspensions and its impact on rheology and diffusion. *J Fluid Mech* 348:103-139.

10. Heemels MW, Hagen MHJ, & Lowe CP (2000) Simulating Solid Colloidal Particles Using the Lattice-Boltzmann Method. *J Comput Phys* 164(1):48-61.

11. Segré G & Silberberg A (1962) Behaviour of macroscopic rigid spheres in Poiseuille flow Part 2. Experimental results and interpretation. *J Fluid Mech* 14(01):136-157.

12. MATAS J-P, MORRIS JF, & GUAZZELLI (2004) Inertial migration of rigid spherical particles in Poiseuille flow. *J Fluid Mech* 515:171-195.

13. Schonberg JA & Hinch EJ (1989) Inertial migration of a sphere in Poiseuille flow. *J Fluid Mech* 203:517-524.

14. Asmolov ES (1999) The inertial lift on a spherical particle in a plane Poiseuille flow at large channel Reynolds number. *J Fluid Mech* 381:63-87.

15. Subramanian G & Koch DL (2006) Inertial effects on the transfer of heat or mass from neutrally buoyant spheres in a steady linear velocity field. *Phys Fluids* 18(7):073302-073318.

16. Ladd AJC (1994) Numerical simulations of particulate suspensions via a discretized Boltzmann equation. Part 2. Numerical results. *J Fluid Mech* 271:311-339.

17. Chen S & Doolen GD (1998) LATTICE BOLTZMANN METHOD FOR FLUID FLOWS. *Annu Rev Fluid Mech* 30(1):329-364.

18. Aidun CK, Lu Y, & Ding EJ (1998) Direct analysis of particulate suspensions with inertia using the discrete Boltzmann equation. *J Fluid Mech* 373:287-311.

19. Brady JF & Bossis G (1988) Stokesian Dynamics. *Annu Rev Fluid Mech* 20(1):111-157.

20. Succi S (2001) *The Lattice Boltzmann Equation for Fluid Dynamics and Beyond* (Clarendon Press).

21. Sukop MC & Thorne DT (2006) *Lattice Boltzmann Modeling: An Introduction for Geoscientists And Engineers* (Springer).

22. Frisch U, *et al.* (1986) *Lattice gas hydrodynamics in two and three dimensions* p Medium: ED; Size: Pages: 56.

23. Ladd AJC & Verberg R (2001) Lattice-Boltzmann simulations of particle-fluid suspensions. *Journal of Statistical Physics* 104(5-6):1191-1251.

24. Chun B & Ladd AJC (2007) Interpolated boundary condition for lattice Boltzmann simulations of flows in narrow gaps. *Phys Rev E* 75(6):066705.

25. Reider MB & Sterling JD (1995) Accuracy of discrete-velocity BGK models for the simulation of the incompressible Navier-Stokes equations. *Computers & Fluids* 24(4):459-467.

26. Guo Z, Zheng C, & Shi B (2002) Discrete lattice effects on the forcing term in the lattice Boltzmann method. *Phys Rev E* 65(4):046308.

27. Dünweg B & Ladd AJC (2008) Lattice Boltzmann Simulations of Soft Matter Systems. Advances in Polymer Science, (Springer Berlin Heidelberg), pp 1-78.

28. d'Humieres D (1994) Generalized Lattice-Boltzmann Equations. *Progr Astronaut Aero* 159:450-458.

29. d'Humières D (2002) Multiple–relaxation–time lattice Boltzmann models in three dimensions. *Philosophical Transactions of the Royal Society of London. Series A: Mathematical, Physical and Engineering Sciences* 360(1792):437-451.

30. Premnath KN & Abraham J (2007) Three-dimensional multi-relaxation time (MRT) lattice-Boltzmann models for multiphase flow. *J Comput Phys* 224(2):539-559.

31. Ginzburg I (2002) A free-surface lattice Boltzmann method for modelling the filling of expanding cavities by Bingham fluids. *Philosophical Transactions of the Royal Society of London. Series A: Mathematical, Physical and Engineering Sciences* 360(1792):453-466.

32. McNamara G, Garcia A, & Alder B (1995) Stabilization of thermal lattice Boltzmann models. *J Stat Phys* 81(1):395-408.

33. Giraud L, D'Humieres D, & Lallemand P (1998) A lattice Boltzmann model for Jeffreys viscoelastic fluid. *Europhys Lett* 42(6):625-630.

34. Adhikari R, Stratford K, Cates ME, & Wagner AJ (2005) Fluctuating lattice Boltzmann. *EPL (Europhysics Letters)* 71(3):473.

35. Lallemand P & Luo L-S (2000) Theory of the lattice Boltzmann method: Dispersion, dissipation, isotropy, Galilean invariance, and stability. *Phys Rev E* 61(6):6546-6562.

36. Pan C, Luo L-S, & Miller CT (2006) An evaluation of lattice Boltzmann schemes for porous medium flow simulation. *Computers & Fluids* 35(8–9):898-909.

37. Lloyd BA, Szekely G, & Harders M (2007) Identification of spring parameters for deformable object simulation. *Ieee T Vis Comput Gr* 13(5):1081-1094.

38. Wang T, Pan TW, Xing ZW, & Glowinski R (2009) Numerical simulation of rheology of red blood cell rouleaux in microchannels. *Phys Rev E* 79(4):041916.

39. Tsubota K-i & Wada S (2010) Elastic force of red blood cell membrane during tank-treading motion: Consideration of the membrane's natural state. *International Journal of Mechanical Sciences* 52(2):356-364.

40. Gavin AB, Christopher MC, & Douglas JC (2001) A lattice spring model of heterogeneous materials with plasticity. *Model Simul Mater Sc* 9(6):485.

41. Gusev AA (2004) Finite Element Mapping for Spring Network Representations of the Mechanics of Solids. *Phys Rev Lett* 93(3):034302.

42. Omori T, *et al.* (2011) Comparison between spring network models and continuum constitutive laws: Application to the large deformation of a capsule in shear flow. *Physical Review E* 83(4):041918.

43. Monette L & Anderson MP (1994) Elastic and fracture properties of the two-dimensional triangular and square lattices. *Model Simul Mater Sc* 2(1):53.

44. Landau LD, Lifshitz EM, Kosevich AM, & Pitaevskiĭ LP (1986) *Theory of Elasticity* (Butterworth-Heinemann).

45. O'Brien GS & Bean CJ (2004) A 3D discrete numerical elastic lattice method for seismic wave propagation in heterogeneous media with topography. *Geophys. Res. Lett.* 31(14):L14608.

46. Jagla EA (2007) Modeling the buckling and delamination of thin films. *Physical Review B* 75(8):085405.

47. Sahimi M & Arbabi S (1993) Mechanics of disordered solids. II. Percolation on elastic networks with bond-bending forces. *Phys Rev B* 47(2):703-712.

48. Ventsel E & Krauthammer T (2001) *Thin Plates and Shells: Theory, Analysis, and Applications* (Marcel Dekker).

49. Bridson R, Marino S, & Fedkiw R (2003) Simulation of clothing with folds and wrinkles. in *Proceedings of the 2003 ACM SIGGRAPH/Eurographics symposium on Computer animation* (Eurographics Association, San Diego, California), pp 28-36.

50. Fedosov DA, Caswell B, & Karniadakis GE (2010) A Multiscale Red Blood Cell Model with Accurate Mechanics, Rheology, and Dynamics. *Biophys J* 98(10):2215-2225.

51. Tuckerman M, Berne BJ, & Martyna GJ (1992) Reversible multiple time scale molecular-dynamics. *Journal of Chemical Physics* 97(3):1990-2001.

52. Zhao G-F, Fang J, & Zhao J (2011) A 3D distinct lattice spring model for elasticity and dynamic failure. *Int J Numer Anal Met* 35(8):859-885.

53. Alexeev A, Verberg R, & Balazs AC (2005) Modeling the Motion of Microcapsules on Compliant Polymeric Surfaces. *Macromolecules* 38(24):10244-10260.

54. Bouzidi Mh, Firdaouss M, & Lallemand P (2001) Momentum transfer of a Boltzmann-lattice fluid with boundaries. *Phys Fluids* 13(11):3452-3459.

55. Clausen JR & Aidun CK (2009) Galilean invariance in the lattice-Boltzmann method and its effect on the calculation of rheological properties in suspensions. *Int J Multiphas Flow* 35(4):307-311.

56. Sangani AS & Acrivos A (1982) Slow flow through a periodic array of spheres. *Int J Multiphas Flow* 8(4):343-360.

57. White FM (1991) *Viscous fluid flow* (McGraw-Hill, New York).

58. Landau LD & Lifshits EM (1959) *Fluid mechanics* (Pergamon Press; Addison-Wesley Pub. Co., London; Reading, Mass.).

59. Yahiaoui S & Feuillebois F (2010) Lift on a sphere moving near a wall in a parabolic flow. *J Fluid Mech* 662:447-474.

60. Krishnan GP & Leighton JDT (1995) Inertial lift on a moving sphere in contact with a plane wall in a shear flow. *Phys Fluids* 7(11):2538-2545.

61. Zeng L, Najjar F, Balachandar S, & Fischer P (2009) Forces on a finite-sized particle located close to a wall in a linear shear flow. *Phys Fluids* 21(3):033302-033318.

62. Derksen JJ & Larsen RA (2011) Drag and lift forces on random assemblies of wall-attached spheres in low-Reynolds-number shear flow. *J Fluid Mech* 673:548-573.

63. Nguyen NQ & Ladd AJC (2002) Lubrication corrections for lattice-Boltzmann simulations of particle suspensions. *Physical Review E* 66(4):046708.

64. Ding EJ & Aidun CK (2003) Extension of the Lattice-Boltzmann Method for Direct Simulation of Suspended Particles Near Contact. *J Stat Phys* 112(3):685-708.

65. Skalak R, Tozeren A, Zarda RP, & Chien S (1973) Strain Energy Function of Red Blood Cell Membranes. *Biophys J* 13(3):245-264.

66. Krüger T, Varnik F, & Raabe D (2011) Efficient and accurate simulations of deformable particles immersed in a fluid using a combined immersed boundary lattice Boltzmann finite element method. *Computers & Mathematics with Applications* 61(12):3485-3505.

67. Barthès-Biesel D (2011) Modeling the motion of capsules in flow. *Current Opinion in Colloid & Interface Science* 16(1):3-12.

68. Pozrikidis C (2001) Effect of membrane bending stiffness on the deformation of capsules in simple shear flow. *J Fluid Mech* 440:269-291.

69. Lac E, Barthes-Biesel D, Pelekasis NA, & Tsamopoulos J (2004) Spherical capsules in three-dimensional unbounded Stokes flows: effect of the membrane constitutive law and onset of buckling. *Journal of Fluid Mechanics* 516:303-334.

70. Lenshof A & Laurell T (2010) Continuous separation of cells and particles in microfluidic systems. *Chemical Society Reviews* 39(3):1203-1217.

71. Petersson F, Aberg L, Sward-Nilsson AM, & Laurell T (2007) Free flow acoustophoresis: Microfluidic-based mode of particle and cell separation. *Analytical Chemistry* 79(14):5117-5123.

72. Pamme N & Wilhelm C (2006) Continuous sorting of magnetic cells via on-chip free-flow magnetophoresis. *Lab on a Chip* 6(8):974-980.

73. Pamme N & Manz A (2004) On-chip free-flow magnetophoresis: Continuous flow separation of magnetic particles and agglomerates. *Analytical Chemistry* 76(24):7250-7256.

74. Cui HH, Voldman J, He XF, & Lim KM (2009) Separation of particles by pulsed dielectrophoresis. *Lab on a Chip* 9(16):2306-2312.

75. Chmela E, Tijssen R, Blom MT, Gardeniers HJGE, & van den Berg A (2002) A Chip System for Size Separation of Macromolecules and Particles by Hydrodynamic Chromatography. *Analytical Chemistry* 74(14):3470-3475.

76. Pamme N (2007) Continuous flow separations in microfluidic devices. *Lab on a Chip* 7(12):1644-1659.

77. Di Carlo D (2009) Inertial microfluidics. *Lab on a Chip* 9(21):3038-3046.

78. Choi S & Park JK (2007) Continuous hydrophoretic separation and sizing of microparticles using slanted obstacles in a microchannel. *Lab on a Chip* 7(7):890-897.

79. Yamada M & Seki M (2005) Hydrodynamic filtration for on-chip particle concentration and classification utilizing microfluidics. *Lab on a Chip* 5(11):1233-1239.

80. Bhagat AAS, Kuntaegowdanahalli SS, & Papautsky I (2009) Inertial microfluidics for continuous particle filtration and extraction. *Microfluidics and Nanofluidics* 7(2):217-226.

81. Di Carlo D, Edd JF, Humphry KJ, Stone HA, & Toner M (2009) Particle Segregation and Dynamics in Confined Flows. *Physical Review Letters* 102(9).

82. Chun B & Ladd AJC (2006) Inertial migration of neutrally buoyant particles in a square duct: An investigation of multiple equilibrium positions. *Physics of Fluids* 18(3).

83. Bhagat AAS, Kuntaegowdanahalli SS, & Papautsky I (2008) Enhanced particle filtration in straight microchannels using shear-modulated inertial migration. *Physics of Fluids* 20(10).

84. Segre G & Silberberg A (1962) Behaviour of Macroscopic Rigid Spheres in Poiseuille Flow .2. Experimental Results and Interpretation. *Journal of Fluid Mechanics* 14(1):136-157.

85. Racila E, *et al.* (1998) Detection and characterization of carcinoma cells in the blood. *Proceedings of the National Academy of Sciences of the United States of America* 95(8):4589-4594.

86. Kononen J, *et al.* (1998) Tissue microarrays for high-throughput molecular profiling of tumor specimens. *Nat. Med.* 4(7):844-847.

87. Xia N, *et al.* (2006) Combined microfluidic-micromagnetic separation of living cells in continuous flow. *Biomed. Microdevices* 8(4):299-308.

88. Han KH & Frazier AB (2006) Paramagnetic capture mode magnetophoretic microseparator for high efficiency blood cell separations. *Lab Chip* 6(2):265-273.

89. Kim U, Qian JR, Kenrick SA, Daugherty PS, & Soh HT (2008) Multitarget Dielectrophoresis Activated Cell Sorter. *Anal. Chem.* 80(22):8656-8661.

90. Pommer MS, *et al.* (2008) Dielectrophoretic separation of platelets from diluted whole blood in microfluidic channels. *Electrophoresis* 29(6):1213-1218.

91. Vahey MD & Voldman J (2008) An equilibrium method for continuous-flow cell sorting using dielectrophoresis. *Anal. Chem.* 80(9):3135-3143.

92. Doh I & Cho YH (2005) A continuous cell separation chip using hydrodynamic dielectrophoresis (DEP) process. *Sens. Actuator A-Phys.* 121(1):59-65.

93. Wang MM, *et al.* (2005) Microfluidic sorting of mammalian cells by optical force switching. *Nat. Biotechnol.* 23(1):83-87.

94. Perroud TD, *et al.* (2008) Microfluidic-based cell sorting of Francisella tularensis infected macrophages using optical forces. *Anal. Chem.* 80(16):6365-6372.

95. Lenshof A, *et al.* (2009) Acoustic Whole Blood Plasmapheresis Chip for Prostate Specific Antigen Microarray Diagnostics. *Anal. Chem.* 81(15):6030-6037.

96. Shi JJ, Huang H, Stratton Z, Huang YP, & Huang TJ (2009) Continuous particle separation in a microfluidic channel via standing surface acoustic waves (SSAW). *Lab Chip* 9(23):3354-3359.

97. Fu AY, Spence C, Scherer A, Arnold FH, & Quake SR (1999) A microfabricated fluorescence-activated cell sorter. *Nat. Biotechnol.* 17(11):1109-1111.

98. Suresh S, *et al.* (2005) Connections between single-cell biomechanics and human disease states: gastrointestinal cancer and malaria. *Acta Biomater.* 1(1):15-30.

99. Guck J, *et al.* (2005) Optical deformability as an inherent cell marker for testing malignant transformation and metastatic competence. *Biophys. J.* 88(5):3689-3698.

100. Cross SE, Jin YS, Rao J, & Gimzewski JK (2007) Nanomechanical analysis of cells from cancer patients. *Nat. Nanotechnol.* 2(12):780-783.

101. Cross SE, *et al.* (2008) AFM-based analysis of human metastatic cancer cells. *Nanotechnology* 19(38).

102. Rosenbluth MJ, Lam WA, & Fletcher DA (2008) Analyzing cell mechanics in hematologic diseases with microfluidic biophysical flow cytometry. *Lab Chip* 8(7):1062-1070.

103. Lee WG, *et al.* (2007) On-chip erythrocyte deformability test under optical pressure. *Lab Chip* 7(4):516-519.

104. Lincoln B, *et al.* (2004) Deformability-based flow cytometry. *Cytom. Part A* 59A(2):203-209.

105. Hou HW, *et al.* (2010) Deformability based cell margination-A simple microfluidic design for malaria-infected erythrocyte separation. *Lab on a Chip* 10(19):2605-2613.

106. Hur SC, Henderson-MacLennan NK, McCabe ERB, & Di Carlo D (2011) Deformability-based cell classification and enrichment using inertial microfluidics. *Lab on a Chip* 11(5):912-920.

107. Mohamed H, Murray M, Turner JN, & Caggana M (2009) Isolation of tumor cells using size and deformation. *J. Chromatogr. A* 1216(47):8289-8295.

108. Zhu C, Bao G, & Wang N (2000) Cell mechanics: Mechanical response, cell adhesion, and molecular deformation. *Annu. Rev. Biomed. Eng.* 2:189-226.

109. Kuo-Kang L (2006) Deformation behaviour of soft particles: a review. *Journal of Physics D: Applied Physics* 39(11):R189.

110. Arata JP & Alexeev A (2009) Designing microfluidic channel that separates elastic particles upon stiffness. *Soft Matter* 5(14):2721-2724.

111. Mao W & Alexeev A (2011) Hydrodynamic sorting of microparticles by size in ridged microchannels. *Physics of Fluids* 23(5):051704.

112. Schmidschonbein GW, Sung KLP, Tozeren H, Skalak R, & Chien S (1981) PASSIVE MECHANICAL-PROPERTIES OF HUMAN-LEUKOCYTES. *Biophys. J.* 36(1):243-256.

113. Yao WJ, *et al.* (2002) Changes of biophysical behavior of K562 cells for p16 gene transfer. *Clin. Hemorheol. Microcirc.* 27(3-4):177-183.

114. Jeffery GB (1922) The Motion of Ellipsoidal Particles Immersed in a Viscous Fluid. *Proceedings of the Royal Society of London. Series A* 102(715):161-179.

115. Trevelyan BJ & Mason SG (1951) Particle motions in sheared suspensions. I. Rotations. *Journal of Colloid Science* 6(4):354-367.

116. Mason SG & Manley RSJ (1956) Particle Motions in Sheared Suspensions: Orientations and Interactions of Rigid Rods. *Proceedings of the Royal Society of London. Series A. Mathematical and Physical Sciences* 238(1212):117-131.

117. Taylor GI (1923) The Motion of Ellipsoidal Particles in a Viscous Fluid. *Proceedings of the Royal Society of London. Series A* 103(720):58-61.

118. Bretherton FP (1962) The motion of rigid particles in a shear flow at low Reynolds number. *J Fluid Mech* 14(02):284-304.

119. Leal LG (1980) Particle Motions in a Viscous Fluid. *Annu Rev Fluid Mech* 12(1):435-476.

120. Qi D & Luo L-S (2003) Rotational and orientational behaviour of three-dimensional spheroidal particles in Couette flows. *J Fluid Mech* 477:201-213.

121. Subramanian G & Koch DL (2005) Inertial effects on fibre motion in simple shear flow. *J Fluid Mech* 535:383-414.

122. Ding EJ & Aidun CK (2000) The dynamics and scaling law for particles suspended in shear flow with inertia. *J Fluid Mech* 423:317-344.

123. Feng J & Joseph DD (1995) The unsteady motion of solid bodies in creeping flows. *J Fluid Mech* 303:83-102.

124. Broday D, Fichman M, Shapiro M, & Gutfinger C (1998) Motion of spheroidal particles in vertical shear flows. *Phys Fluids* 10(1):86-100.

125. Yu Z, Phan-Thien N, & Tanner RI (2007) Rotation of a spheroid in a Couette flow at moderate Reynolds numbers. *Phys Rev E* 76(2):026310.

126. Altenbach H, Naumenko K, Pylypenko S, & Renner B (2007) Influence of rotary inertia on the fiber dynamics in homogeneous creeping flows. *ZAMM - Journal of Applied Mathematics and Mechanics / Zeitschrift für Angewandte Mathematik und Mechanik* 87(2):81-93.

127. Lundell F & Carlsson A (2010) Heavy ellipsoids in creeping shear flow: Transitions of the particle rotation rate and orbit shape. *Phys Rev E* 81(1):016323.

128. Zettner CM & Yoda M (2001) The circular cylinder in simple shear at moderate Reynolds numbers: An experimental study. *Experiments in Fluids* 30(3):346-353.

129. Ku XK & Lin JZ (2009) Inertial effects on the rotational motion of a fibre in simple shear flow between two bounding walls. *Physica Scripta* 80(2):025801.

130. Masaeli M, *et al.* (2012) Continuous Inertial Focusing and Separation of Particles by Shape. *Physical Review X* 2(3):031017.

131. Wagner AJ & Pagonabarraga I (2002) Lees–Edwards boundary conditions for lattice Boltzmann. *J Stat Phys* 107(1-2):521-537.

132. Huang H, Yang X, Krafczyk M, & Lu X-Y (2012) Rotation of spheroidal particles in Couette flows. *J Fluid Mech* 692:369-394.

133. Nilsen C & Andersson HI (2013) Chaotic rotation of inertial spheroids in oscillating shear flow. *Phys Fluids* 25:013303.

134. Subramanian G & Koch DL (2006) Inertial effects on the orientation of nearly spherical particles in simple shear flow. *J Fluid Mech* 557:257-296.

135. Mitragotri S & Lahann J (2009) Physical approaches to biomaterial design. *Nat Mater* 8(1):15-23.

136. Martin SG (2009) Geometric control of the cell cycle. *Cell Cycle* 8:3643-3647.

137. Wongsrichanalai C, Barcus MJ, Muth S, Sutamihardja A, & Wernsdorfer WH (2007) A Review of Malaria Diagnostic Tools: Microscopy and Rapid Diagnostic Test (RDT). *The American Journal of Tropical Medicine and Hygiene* 77(6 Suppl):119-127.

138. Hashemi N, Erickson JS, Golden JP, & Ligler FS (2011) Optofluidic characterization of marine algae using a microflow cytometer. *Biomicrofluidics* 5(3):032009-032009.

139. Pregibon DC, Toner M, & Doyle PS (2007) Multifunctional Encoded Particles for High-Throughput Biomolecule Analysis. *Science* 315(5817):1393-1396.

140. Shchepelina O, *et al.* (2010) Anisotropic Micro- and Nano-Capsules. *Macromolecular Rapid Communications* 31(23):2041-2046.

141. Ho B & Leal L (1974) Inertial migration of rigid spheres in two-dimensional unidirectional flows. *J Fluid Mech* 65(02):365-400.

142. Matas J-P, Morris JF, Guazzelli, Eacute, & Lisabeth (2004) Inertial migration of rigid spherical particles in Poiseuille flow. *J Fluid Mech* 515:171-195.

143. Matas J-P, Morris JF, & Guazzelli E (2009) Lateral force on a rigid sphere in large-inertia laminar pipe flow. *J Fluid Mech* 621:59.

144. Di Carlo D, Edd JF, Humphry KJ, Stone HA, & Toner M (2009) Particle segregation and dynamics in confined flows. *Phys Rev Lett* 102(9):094503.

145. Chun B & Ladd A (2006) Inertial migration of neutrally buoyant particles in a square duct: An investigation of multiple equilibrium positions. *Phys Fluids* 18:031704.

146. Bhattacharya S, Gurung DK, & Navardi S (2013) Radial lift on a suspended finite-sized sphere due to fluid inertia for low-Reynolds-number flow through a cylinder. *J Fluid Mech* 722:159-186.

147. Chwang AT & Wu TY (1976) Hydromechanics of low-Reynolds-number flow. Part 4. Translation of spheroids. *J. Fluid Mech* 75(4):677-689.

148. Sugihara-Seki M (1996) The motion of an ellipsoid in tube flow at low Reynolds numbers. *J Fluid Mech* 324(1):287-308.

149. Pan T-W, Chang C-C, & Glowinski R (2008) On the motion of a neutrally buoyant ellipsoid in a three-dimensional Poiseuille flow. *Comput Method Appl M* 197(25):2198-2209.

150. Chen S-D, Pan T-W, & Chang C-C (2012) The motion of a single and multiple neutrally buoyant elliptical cylinders in plane Poiseuille flow. *Phys Fluids* 24:103302.

151. Staben ME, Zinchenko AZ, & Davis RH (2006) Dynamic simulation of spheroid motion between two parallel plane walls in low-Reynolds-number Poiseuille flow. *J Fluid Mech* 553:187-226.

VITA

WENBIN MAO

Wenbin Mao was born in the historic city of Xiangyang, Hubei, China. He received his B.Eng. degree in Thermal Energy and Power Engineering from the University of Science and Technology of China in 2006. Subsequently, he joined the Guangzhou Institute of Energy Conversion in the Chinese Academy of Sciences and earned his M.S. in Engineering of Thermophysics in 2009. He then moved to Georgia Tech to pursue a Ph.D. degree in Mechanical Engineering. Wenbin employs numerical simulations to solve challenging problems in the interdisciplinary research of engineering, physics, and biology. His research interests include computational fluid dynamics, fluid-structure interactions, complex fluids, and biomimetic modeling and design.